Motion Correction and Volumetric Acquisition Techniques for Coronary Magnetic Resonance Angiography

Zur Erlangung des akademischen Grades eines

DOKTOR-INGENIEURS

von der Fakultät für
Elektrotechnik und Informationstechnik
der Universität Fridericiana Karlsruhe
genehmigte

DISSERTATION

von

Dipl.-Ing. Christian Stehning
aus Dorsten

Contents

Abbreviations

- MRI   magnetic resonance imaging
- MRA   magnetic resonance angiography
- CMRA   coronary magnetic resonance angiography
- CVD   cardiovascular disease
- CAD   coronary artery disease
- CHD   coronary heart disease
- RCA   right coronary artery
- LCA   left coronary artery
- LM   left main artery
- LAD   left anterior descending artery
- LCX   left circumflex artery
- superior   towards head
- inferior   towards feet
- anterior   towards front
- posterior   towards back
- SI   superior-inferior
- FH   from feet to head
- RL   from right to left
- AP   from anterior to posterior
- PC   personal computer
- PSF   point spread function
- CC   cross correlation
- NMI   normalized mutual information
- EFT   epicardiac fat tracking
- COM   center of mass
- ROAR   readout orientation arrangement
- RR   from R-wave to R-wave
- FFT   fast Fourier transformation
- DFT   discrete Fourier transformation
- SENSE   sensitivity encoding
- GRAPPA   generalized autocalibrating partially parallel acquisitions

Preface

According to WHO estimates, 16.7 million people die of cardiovascular diseases (CVD) each year. Since 1900 CVD has been the No. 1 killer in the United States every year, claiming about as many lives each year as the next five leading causes of death combined, which are cancer, chronic lower respiratory diseases, accidents, diabetes mellitus, and influenza and pneumonia [amh05]. Among the different causes of CVD, coronary heart disease (CHD) is the single largest killer. While these statistics were raised for the United States, they can be considered representative for the population in the western world.

The onset of knowledge of coronary disease cannot be precisely dated. Among the first to describe and work on coronary arteries was Leonardo da Vinci (1452-1519). He incorrectly drew the liver as the center of circulation (Fig. I.1). But he stated that „vessels in the elderly through the thickening of the tunics, restrict the transit of blood [who]". This is one of the earliest descriptions of atherosclerosis.

Almost five centuries later, in 1895, a notable innovation crucial to the future development in cardiology was the discovery of X-rays by Willhelm Conrad Röntgen (Fig. I.2). This historic discovery was the key to numerous research activities, revealing new diagnostic and therapeutic methods in cardiology until today [roe].
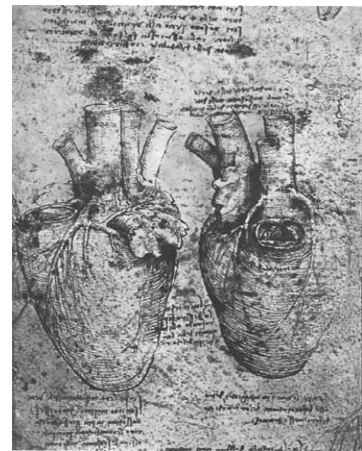
Fig I.1 Leonardo da Vincis sketches showing the distribution of the coronary vessels, from different views. His observations were based on dissections of the ox heart

One year after the discovery of X-Rays, Francis Williams (1852-1936) produced the first fluoroscopic images of the beating heart (Fig. I.2 [c]). His fluoroscopic experience led to the 1901 publication of one of the most widely-read textbooks in the new field: „The Roentgen Rays in Medicine and Surgery". In the following nineteen years he examined or treated more than 150,000 patients [soy] .
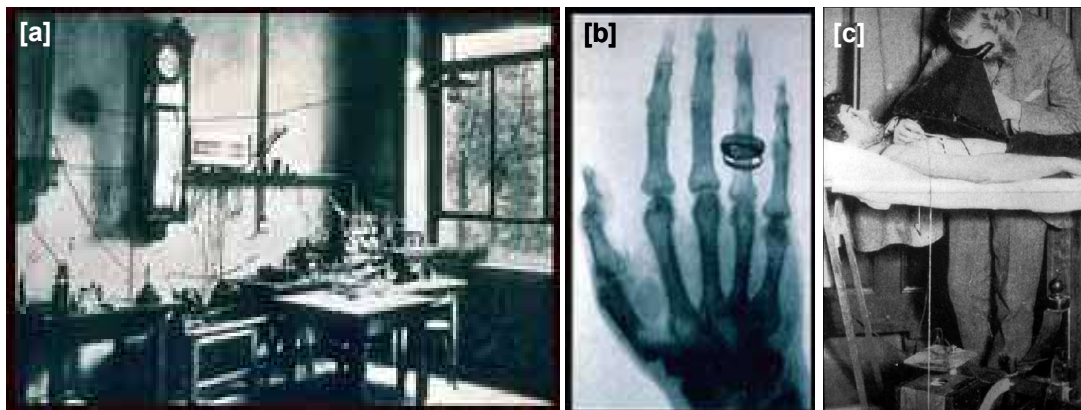
Fig I.2 Physical Institute laboratory room at the University of Würzburg, in which Röntgen first noted and investigated X-rays [a]. Fig. I.2 [b] shows a Radiograph of the hand of Albert von Kolliker, made at the conclusion of Roentgen's lecture and demonstration at the Würzburg Physical-Medical Society on 23 January 1896. In Fig. I.2 [c], Francis Williams during his early fluoroscopic experiments in 1901 is shown

To date, invasive X-Ray angiography performed in the catheter lab is actually the gold standard for the identification of coronary artery disease. While spatial resolution and specificity of X-Ray angiography are yet unsurpassed, mayor drawbacks that are associated with this invasive technique, such as the exposure to ionizing radiation or potential risk of infection or death due to the insertion of a catheter, have not been solved to date. Furthermore, in about one third of all catheterizations, no significant coronary disease is diagnosed during the invasive intervention. Hence, a non-invasive modality capable to rule out CAD from the first is highly desirable.

Fig I.3 Paul C. Lauterbur (left) and Sir Peter Mansfield (right) were presented with the nobel prize in 2003 for discoveries concerning MRI

Besides other alternative imaging modalities like Echocardiography or nuclear imaging (PET, SPECT), magnetic resonance imaging (MRI) has gained increased clinical interest for cardiac diagnostics over the recent years. The phenomenon of nuclear magnetic resonance was first demonstrated in 1946 [bloch46] and has resulted in Nobel Prizes in both Physics (Felix Bloch and Edward Mills Purcell) and Chemistry (Richard Ernst). Recently in 2003, the Nobel Prize in Physiology or Medicine was awarded to Paul Lauterbur and Sir Peter Mansfield (Fig. I.3) for their discoveries in 1973 concerning magnetic resonance imaging ([laut73], [mans73]). As ever, the Nobel Prize is not without controversy. Physician Raymond Damadian pioneered the

application of NMR in medicine during the early 1970s and built the first MRI scanner (Fig. I.4). However, Lauterbur and Mansfield used magnetic field gradients, which led to the form of imaging hospitals now use routinely (Fig. I.5).
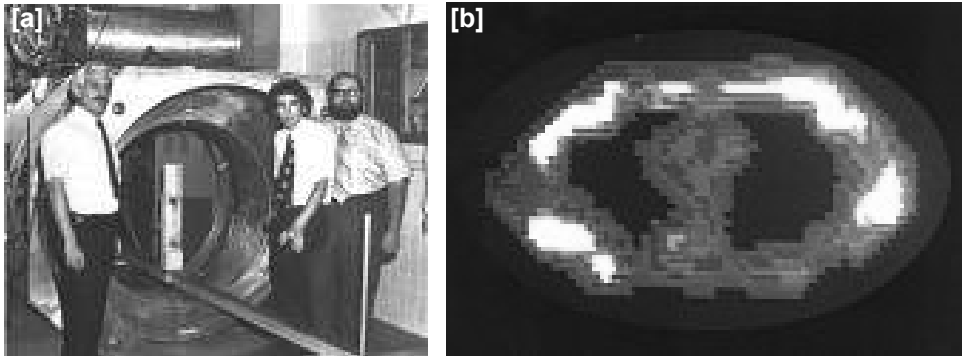
Fig I.4 *Raymond Damadian with his post-doctoral research fellows, L.Minkoff and M. Goldsmith, and first MR scanner [a]. Fig I.4 [b] shows the first MR image of the human body, a cross-section of Minkoff's chest (1977)*

Although MRI is a relatively new technique, it has undergone impressive enhancements in the recent years, and it brings along a great potential for the development of entirely new diagnostic applications. Moreover, MRI provides an excellent soft-tissue contrast and allows the assessment of many physiological properties such as flow, perfusion, strain, and viability. Currently, MRI is the only modality that has the potential to provide all required morphological and functional information as well as the required information of the cardiac vasculature in a single, comprehensive, non-invasive examination as a „One-Stop-Shop" [kram98]. Finally, in contrast to X-ray angiography, MRI is a non-invasive technique.
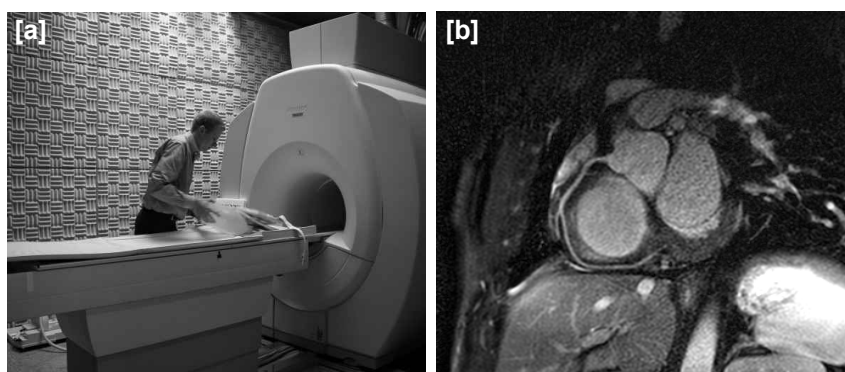
Fig I.5 *Clinical MR scanner [a] operating at 3 Tesla. In [b], a coronary angiogram of the right coronary artery (RCA) is shown*

Hence, it is a primary goal of researchers, engineers and clinicians around the world to extend the field of MR imaging applications to the diagnosis of coronary heart diseases, such as the

detection of coronary stenoses. In the recent past, magnetic resonance angiography (MRA) has been successfully applied for the visualization of the coronary arteries and potential coronary artery disease [kim01]. However, image quality is still hampered by certain limitations such as motion during the prolonged acquisition and has not reached sufficient quality for widespread diagnostic application yet. Furthermore, coronary MRA is a very complex examination and thus remains a difficult and challenging task.

Hence, it is the intention of this work to present new methods with improved ease-of use and novel motion correction strategies for simplified MR imaging with high resolution and shortened scan times. A more detailed overview is given in the following section.

Introduction and outline

Clinical interest in magnetic resonance imaging (MRI) for cardiac diagnostics has grown over the recent years, as it is a non-invasive technique providing an excellent soft-tissue contrast and allowing the assessment of many morphological and functional information of the cardiac vasculature. However, despite the continuous development of improved imaging techniques, coronary imaging still remains a challenging task for mainly two reasons.

To date, the amount of MR data required to cover the coronary artery tree with sufficient resolution cannot be measured instantaneously within a fraction of one heart beat. Therefore, the data acquisition is split into multiple heart beats, which makes imaging very sensitive to cardiac and respiratory motion. Only small, well-defined fractions of the cardiac and respiratory cycle, where motion is expected to be minimal, are used for imaging. As a consequence thereof, scan time is prolonged considerably to the order of several minutes, which may not be tolerated by patients in clinical practice. Hence, improved scanning methods that provide an increased scan efficiency and abbreviated scan time are desirable.

An additional obstacle in coronary MRA is the complex examination, requiring extensive scout scanning prior to the actual image acquisition. These preparations are necessary to locate individual anatomical details such as the coronary arteries, and to plan the actual imaging experiment. As an improvement, it is desirable to acquire an extended volume, e.g. the entire heart, with high and isotropic resolution instead, making initial planning rather simple.

The aim of the present work was to address these two current limitations of coronary MRA. In chapter 2, motion compensation strategies to correct for intrinsic cardiac motion are presented, which allow for improved scan efficiency and shortened scan times while maintaining a high image quality. For this purpose, non-Cartesian (radial "stack-of-stars") acquisition techniques were employed, which were shown to be inherently less sensitive to motion. Furthermore, it is a particular asset of the radial acquisition that images can be reconstructed from an undersampled subset of k-space data with very little aliasing artifacts. Also, no additional a-priory information such as the coil sensitivity map is necessary to reconstruct images from undersampled k-space data. This allows for a novel, image-based detection of relative vessel motion between undersamped k-space segments, and facilitates appropriate motion correction prior to the reconstruction of a final, high resolution image. First

in vivo results obtained in healthy adult volunteers using the novel approach for cardiac motion correction conclude the second chapter.

To take a further step forward, the well-established thin-slab acquisition using stack-of-stars sampling, which is radial in in-plane direction, but Cartesian in the remaining phase encoding direction, has been extended to a true 3D radial sampling fashion, which further accentuates the beneficial assets of radial scanning, such as the low sensitivity to motion and reduced aliasing artifacts in an undersampled acquisition. The present work includes the implementation and evaluation of the 3D radial sampling scheme on a clinical MR scanner, as well as the development of an appropriate image reconstruction by means of three-dimensional regridding to reconstruct data acquired with these trajectories. Furthermore, considerations concerning the available SNR and the effect of undersampling in a 3D radial acquisition are given in the theory section.

First *in vivo* results obtained with a whole-heart coronary MRA protocol using 3D radial sampling are presented in chapter 3. A volumetric coverage with isotropic resolution in all three spatial dimensions was obtained, which allows for a retrospective visualization of the coronary vessels.

Furthermore, additional beneficial assets of 3D radial scanning are investigated in more detail in the third chapter. In radial sampling, the acquisition is insensitive to motion perpendicular to the readout direction. This asset has been utilized to reduce respiratory motion artifacts by means of „smart" reordering of readouts in realtime during the respiratory cycle.

Furthermore, in radial scanning, every readout provides information about the entire imaged volume. In turn, it is possible to extract motion information from each sampled echo. Consequently, a self-navigated acquisition was developed that eliminates the need for additional respiratory bellows or navigator echoes by means of extracting the motion information directly from the MR data acquired for imaging. Finally, first *in vivo* whole-heart images acquired in a very short scan time, using parallel imaging approaches on a 32 channel system, conclude the third chapter.

The presented work was created at the Philips Research Laboratories in Hamburg, under the supervision of Dr. Peter Börnert and Prof. Dr. Olaf Dössel of the Institute of Biomedical Engineering, University of Karlsruhe. Parts of this work where accomplished at the Johns Hopkins University School of Medicine in Baltimore, Maryland, USA, in cooperation with Prof. Dr. Matthias Stuber. All examinations were performed on clinical Philips 1.5T and 3.0T whole-body MR scanners.

1. Theory

1.1 Cardiac motion – an overview

The heart beats continuously in a periodic fashion to provide blood supply of the entire body. The left and right ventricle synchronously press the blood batch-wise into the aorta and the pulmonary trunk, respectively. The periodic cardiac motion can be subdivided into a phase of contraction (systole) and a phase of relaxation (diastole). The systole starts with the falling edge of the R-wave of the electrocardiogram, which is sketched in Fig. 1.1.
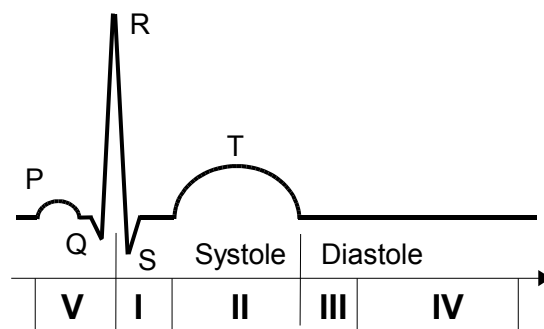
Fig 1.1 The Electrocardiogram (EKG) over the R-R interval: isovolumetric contraction of the ventricles (I), ejection phase (II) isovolumetric relaxation (III), passive filling of the ventricles (IV), contraction of the atria = active filling of the ventricles (V)

The ventricular muscles start to contract, while the volumes of the ventricles stay constant (I). When the pressure in the ventricles is greater than the pressure in the aorta and the pulmonary trunk, the blood is ejected out of the ventricles (II). The diastole begins at the end of the T-wave with the isovolumetric relaxation of the ventricles (III). During mid-diastole, the ventricles are passively refilled (IV). In end-diastole, the ventricles are actively filled due to the contraction of the atria (V).

The volume reduction of the LV in systole, which is also referred to as the ejection fraction, is caused by the reduction of the ventricle diameter due to thickening of the myocardium and a slight systolic torsion of the apex by 5 to 10 degree as shown in Fig. 1.2. In addition, the axial ventricle length is slightly shortened during systole. The ejection fraction of the RV is due to shortening of the axial ventricle length and a shortening of the anterior free wall.

In coronary magnetic resonance angiography with a targeted submillimeter resolution, cardiac motion induced vessel motion has to be taken into account. The motion pattern of the coronary
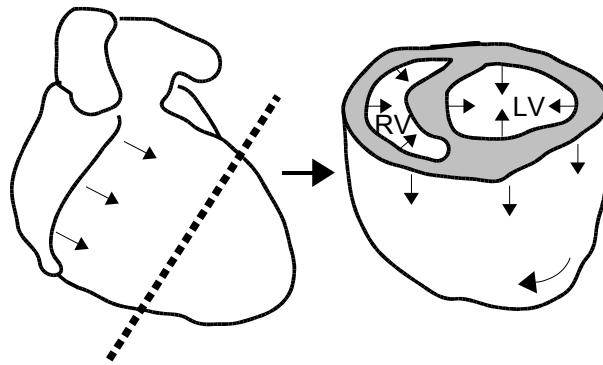
Fig 1.2 Ejection kinetics of the ventricles during systole

arteries (RCA, LAD, LCx, cf. Fig. 1.3) is determined by the motion of the left and right ventricle, for which they provide blood supply. An estimate of vessel motion during the cardiac cycle can be obtained by a time-resolved cine scan in transverse orientation as shown in Figs. 1.3 [a] and [b], respectively.
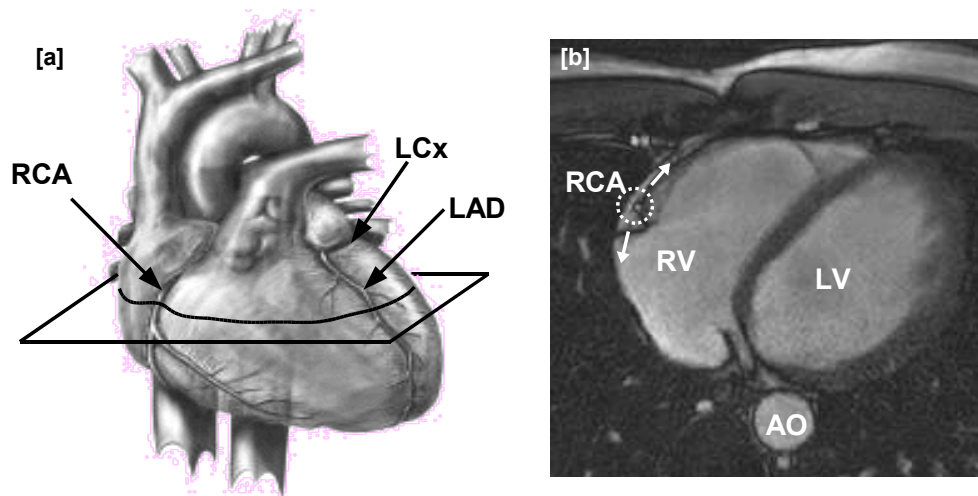
Fig 1.3 Human heart and coronary arteries. Right coronary artery (RCA), left anterior descending artery (LAD), left cirumflex (LCx). A transversal imaging plane though the heart is shown in black in [a]. In [b], a MR image acquired in transversal orientation shows the right ventricle (RV), left ventricle (LV), descending aorta (AO) and a section through the RCA (white circle). During the cardiac cycle, the RCA section performs a rotational motion (white arrows) in the imaging plane along with the RV
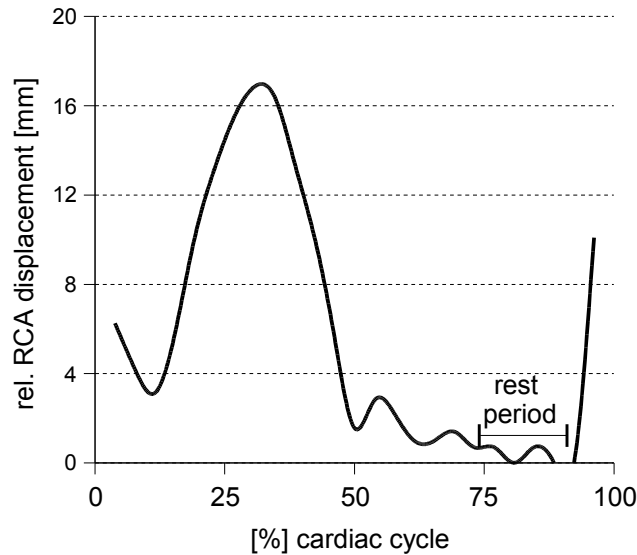
Fig 1.4 *Measured displacement [mm] of the RCA section relative to a reference position in late diastole. A rest period with little coronary motion is observed between 75% and 90% of the cardiac cycle for the examined volunteer*

Figure 1.4 shows a quantitative example of coronary vessel motion during the cardiac cycle for a healthy volunteer, which was measured by means of a time-resolved (cine) scan using a transverse slice through the heart. As evident in Fig. 1.4, the displacement of the RCA during the cardiac cycle has an amplitude in the order of centimeters, resulting in serious blurring and ghosting or streaking artifacts as described in the theory section. Hence, coronary MRA in the presence of motion is a challenging task.

For further analysis, cardiac motion during magnetic resonance imaging can further be decomposed into four different types, which are illustrated in Fig. 1.5. First, the cardiac data acquisition window usually has a finite duration, T_{AQ}, and motion that occurs within the sampling window in the cardiac cycle will be referred to as intra-RR motion. The cardiac acquisition window can be further subdivided into segments $S_1..S_n$. Hence, intra-RR motion is decomposed into intra-segment and and inter-segment motion. If the segment duration is sufficiently short, intra-segment motion is negligible, but inter-segment motion remains to be taken into account.
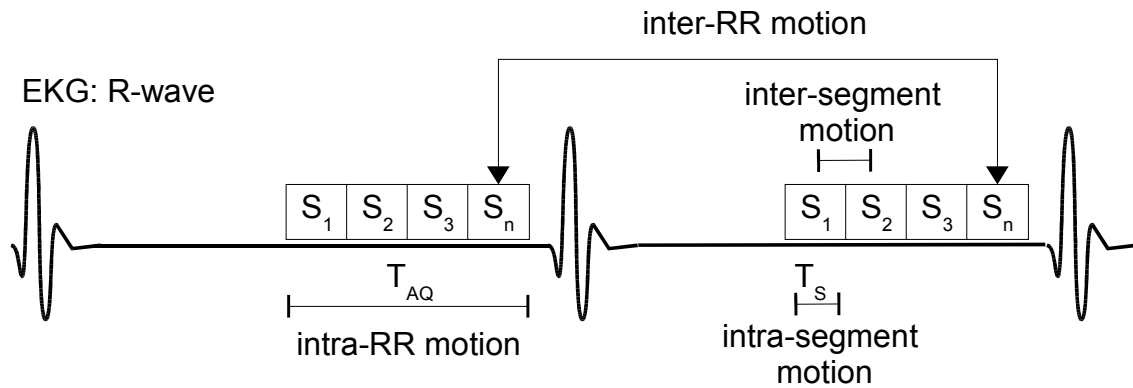
Fig. 1.5 *Classification of motion in cardiac imaging. Intra-RR motion occurs during sampling in the cardiac cycle due to cardiac motion. The cardiac acquisition window can be further subdivided into segments $S_1..S_n$. Thus, intra-RR motion is decomposed into intra-segment motion, and inter-segment motion. If the segment duration T_s is sufficiently short, intra-segment motion is negligible*

Furthermore, the cardiac cycle may vary during scanning, which will be referred to as inter-RR motion. Variations of the cardiac cycle may be induced, for instance, by emotional stress or relaxation of the patient, which has a significant impact on the subject's heart rate. Another source of inter-RR motion is the respiration-induced bulk shift of the heart in feet-head direction. However, this topic has been covered in much detail in [manke03], and therefor it is not the main focus of the present work.

1.2 Motion in MR imaging

The purpose of this chapter is to provide the mathematical supplement to describe motion effects in MR imaging in a quantitative manner. The basics of MR physics shall not be discussed here, as they are described in much detail in the literature ([haa99], [vla02], [liang99]). Moreover, to gain insight into the MR imaging sequence, the reader is referred to the literature as well, which provides a comprehensive overview of the large diversity of MR sequences that are available, including a comparison of their characteristic properties. However, the basics that are necessary to understand the effect of motion on the MR image, and a closed-form description of motion correction approaches, are provided in the following sections.

1.2.1 MR imaging in the absence of motion

The Bloch equation

In principle, the underlying process that generates the MR signal needs to be treated in terms of quantum mechanics. However, a classical treatment on the basics of the Bloch equation [bloch46] is possible, which will be derived briefly in the following section. The differential equation for the precession of an ensemble of spinning tops with a magnetic dipole moment in an external magnetic field is

$$\frac{\delta \vec{m}}{\delta t} = \gamma \left(\vec{m} \times \vec{B} \right) \qquad \qquad [1.1]$$

where $\vec{m}$ represents the magnetization density measured in [A/m], which will be referred to as the „magnetization", and $\vec{B}$ denotes the magnetic flux density measured in Tesla [T], which will be referred to as the „magnetic field". The constant $\gamma = 2\pi \cdot 42.6\, MHz/T$ is the gyromagnetic constant for protons (spin ½). Equation 1.1 implies that the temporal derivative of the magnetization is oriented perpendicular to the plane defined by $\vec{m}$ and $\vec{B}$. For magnetization that is not aligned with the magnetic field $\vec{B}$, this results in a precession around $\vec{B}$ with the angular velocity, ω_L.

$$\omega_L = \gamma |\vec{B}|$$ [1.2]

The angular precession frequency ω_L is known as the Larmor frequency. In practice, three different magnetic fields add up to $\vec{B}$. The first component is the main magnetic field $\vec{B}_0$ oriented in z direction, the second is the position-dependent gradient field $\vec{G}(\vec{r})$, and the third is the magnetic component $\vec{B}_1$ of the RF excitation pulse that rotates with the Larmor frequency. Hence, Eq. 1.1 can be rewritten as:

$$\frac{\delta \vec{m}}{\delta t} = \gamma \, \vec{m} \times \left(\vec{B}_0 + \vec{G}(\vec{r}) + \vec{B}_1 \right)$$ [1.3]

When a new coordinate system (x', y', z) that rotates with the Larmor frequency about the z-axis („rotating frame of reference") is introduced, the main magnetic field component $\vec{B}_0$ vanishes in Eq. 1.3.

Furthermore, if the spin system is not in equilibrium, which means that the magnetization vector $\vec{m}$ is not aligned with the main magnetic field $\vec{B}_0$, two relaxation processes exist that bring the system back to equilibrium. The first one is called spin-lattice relaxation and drives the longitudinal component m_z of the magnetization vector back to the maximum, i.e., the spins are re-aligned with the main magnetic field, and the second one is called spin-spin relaxation that dephases the transversal component m_T, i.e., the magnetization in the x'y'-plane. The longitudinal relaxation with the characteristic decay T_1 is described by the differential equation 1.4.

$$\frac{\delta m_z(t)}{\delta t} = -\frac{m_z(t) - m_0}{T_1}$$ [1.4]

Where m_0 is the magnetization in thermal equilibrium. The transverse relaxation with the characteristic decay time T_2 is given by Eq. 1.5.

$$\frac{\delta\, m_T(t)}{\delta\, t} = -\frac{m_T(t)}{T_2}$$ [1.5]

Combining equations 1.3, 1.4, and 1.5 yields the *Bloch equation* in matrix notation:

$$\frac{\delta\,\vec{m}}{\delta\,t} = \begin{bmatrix} -1/T_2 & \gamma\,\vec{G}\cdot\vec{r} & -\gamma\,B_{1y'} \\ -\gamma\,\vec{G}\cdot\vec{r} & -1/T_2 & \gamma\,B_{1x'} \\ \gamma\,B_{1y'} & -\gamma\,B_{1x'} & -1/T_1 \end{bmatrix}\vec{m} + \begin{bmatrix} 0 \\ 0 \\ m_0/T_1 \end{bmatrix}$$ [1.6]

   With the Bloch equation, a macroscopic description ([slich96], [abr83]) of the quantum-mechanical NMR process is possible, and most problems in MRI can be described in a comprehensive way. Thus, the Bloch equation is the basis for the following considerations.

Spatial encoding and image reconstruction

For simplicity, the excitation process, i.e., flipping magnetization from equilibrium into the transverse plane, is not discussed here, as it is described in much detail in the literature ([haacke99], [vla02], [liang99]). Furthermore, relaxation effects shall be neglected for the time being. Thus, with $B_1 = 0$ and $(T_1, T_2 \rightarrow \infty)$ the Bloch equation for the transverse magnetization of a single infinitesimal volume element (delta probe) after excitation reads

$$\frac{\delta\, m}{\delta\, t} = \gamma\left(\vec{G}\cdot\vec{r}\right)\begin{pmatrix} m_{y'} \\ m_{x'} \\ 0 \end{pmatrix}$$ [1.7]

If we introduce the transversal magnetization in complex notation $m_T = m_{x'} + j\, m_{y'}$, Eq. 1.7 reads

$$\frac{\delta\, m_T}{\delta\, t} = -j\,\gamma\left(\vec{G}\cdot\vec{r}\right)m_T$$ [1.8]

The general solution of Eq. 1.8 is

$$m_T(t) = m_{T,0} e^{-j\gamma \int\limits_0^t \vec{G}(\tau)\cdot\vec{r}\, d\tau} \qquad [1.9]$$

Hence, the resulting MR signal that is induced in the RF receive coil by the transversal magnetization at a certain point in time t is determined by the integral over the excited spins in the imaged matter.

$$S(t) = \int\limits_{\vec{r}} m_{T,0}(\vec{r}) e^{-j\gamma \int\limits_0^t \vec{G}(\tau)\cdot\vec{r}\, d\tau}\, d\vec{r} \qquad [1.10]$$

As evident from Eq. 1.10, an applied gradient $\vec{G}$ yields an accumulation of phase φ in the received MR signal:

$$\varphi(t,\vec{r}) = \gamma \int\limits_0^t \vec{G}(\tau)\cdot\vec{r}\, d\tau \qquad [1.11]$$

Since the gradient G(τ) is a known function, we can make the substitution

$$\vec{k}(t) \overset{!}{=} \gamma \int\limits_0^t \vec{G}(\tau)\, d\tau \qquad \text{with} \quad \vec{k} = \left[k_x, k_y, k_z\right]^T \qquad [1.12]$$

The space that is spanned by the wave number, $\vec{k}$, is referred to as inverse spatial domain, or k-space [twieg83]. Now Eq. 1.10 can be rewritten as

$$S(\vec{k}) = \int\limits_{\vec{r}} m_{T,0}(\vec{r}) e^{-j\vec{k}\cdot\vec{r}}\, d\vec{r} \qquad [1.13]$$

It can be recognized from this equation that the received MR signal $S(\vec{k})$ is equivalent to the Fourier transform of the transverse magnetization density $m_{T,0}(\vec{r})$. Provided that k-space is sufficiently covered by means of an appropriate order of encoding gradients and data

acquisition ("MR sequence"), the reconstructed image can be obtained by means of the inverse Fourier transform of $S(\vec{k})$.

$$m_{T,0}(\vec{r}) = \frac{1}{(2\pi)^3} \int\limits_{\vec{k}} S(\vec{k}) e^{j\vec{k}\cdot\vec{r}} d\vec{k} \qquad [1.14]$$

Equation 1.13 and its counterpart 1.14 are the fundamental MR imaging equations describing the spatial signal encoding and the image reconstruction process, respectively [kum75]. Essential for MRI is that the spatial information of the received signal is stored in the signal phase $\varphi = \vec{k}\cdot\vec{r}$, where $\vec{k}$ is a function of time t and has the dimension [m^{-1}]. However, the equations are only valid if no motion is present. Otherwise, the magnetization location $\vec{r}$ is a function of time, and $\vec{r}$ could not be separated from the inner integral in Eq. 1.10. This situation is addressed in the next section.

1.2.2 Effect of motion in during data acquisition

If motion is present during signal reception, the localization of magnetization is not constant ([wood85], [haa86], [lau93], [xia93]). Moreover, the position vector transforms into a a time-variant function $\vec{r} \Rightarrow \vec{R}(\vec{r},\tau)$. Hence, the distorted receive signal S' can be described as in Eq. 1.15 [haa86]:

$$S'(t) = \int\limits_{\vec{r}} m_{T,0}(\vec{r}_0) e^{-j\gamma \int\limits_0^t \vec{G}(\tau)\cdot\vec{R}(\vec{r},\tau) d\tau} d\vec{r}_0 \qquad [1.15]$$

where the $m_{T,0}$ and $\vec{r}_0$ denote the transverse magnetization and the position at the point in time t=0, respectively. In the presence of motion, the k-space formalism of Eq. 1.14, which allows to reconstruct an image by means of the discrete Fourier transform, is not applicable, as the spin-localization is time-variant and cannot be extracted from the inner integral. However, for a closed-form description of the effect of motion on the reconstructed image, we assume

that the time-variant object deformation can be decomposed into a linear transformation A(τ) and a translation $\vec{r}_{tr}(\tau)$ as illustrated in Fig. 1.6.

$$[a]\ \text{shearing} \qquad A=\begin{bmatrix} 1 & a_{xy} \\ 1 & 1 \end{bmatrix}$$

$$[b]\ \text{contraction / expansion} \qquad A=\begin{bmatrix} a_{xx} & 1 \\ 1 & a_{yy} \end{bmatrix}$$

$$[c]\ \text{rotation} \qquad A=\begin{bmatrix} \cos(\alpha) & \sin(\alpha) \\ -\sin(\alpha) & \cos(\alpha) \end{bmatrix}$$

$$[d]\ \text{translation} \qquad \vec{r}=\begin{bmatrix} \Delta x \\ \Delta y \end{bmatrix}$$
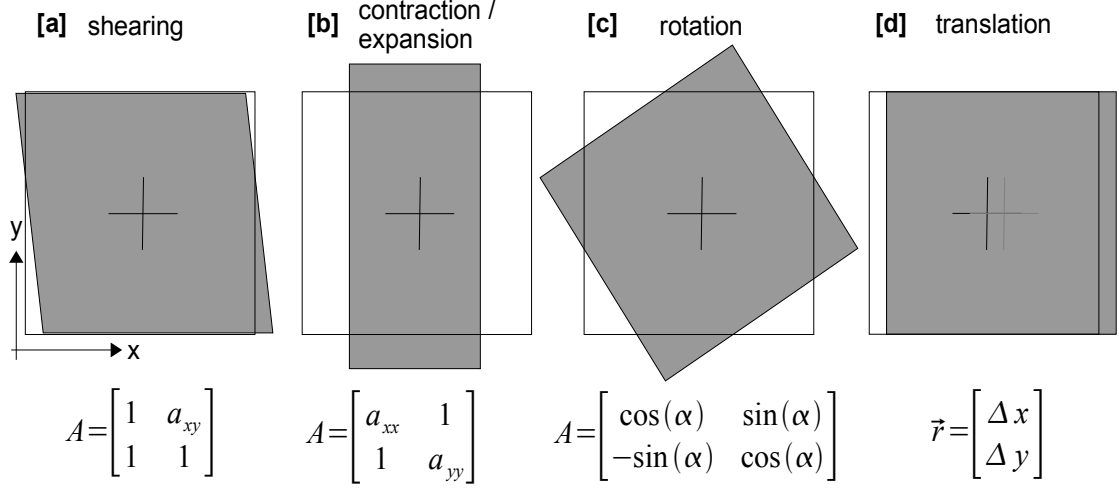
Fig 1.6 *Examples of linear transformations (a-c) and translation (d). Complex motion patterns can be modelled by combining all transformation matrices and the translation vector*

Hence, the time-variant localization vector becomes

$$\vec{R}(\vec{r},\tau)=A(\tau)\vec{r}+\vec{r}_{tr}(\tau) \tag{1.16}$$

Thus, Eq. [1.15] can be rewritten as

$$
\begin{aligned}
S'(t) &= \int_{\vec{r}} m_{T,0}(\vec{r}_0)\, e^{-j\gamma\int_0^t \vec{G}(\tau)\cdot\left(A(\tau)\vec{r}+\vec{r}_{tr}(\tau)\right)d\tau}\, d\vec{r}_0 \\
&= \int_{\vec{r}} m_{T,0}(\vec{r}_0)\, e^{-j\gamma\int_0^t \left(\left(A^T(\tau)\vec{G}(\tau)\right)\cdot\vec{r}+\vec{G}(\tau)\cdot\vec{r}_{tr}(\tau)\right)d\tau}\, d\vec{r}_0 \\
&= \int_{\vec{r}} m_{T,0}(\vec{r}_0)\, e^{-j\vec{r}\gamma\underbrace{\int_0^t A^T(\tau)\vec{G}(\tau)}_{k(t)}}\cdot e^{-j\gamma\underbrace{\int_0^t \vec{G}(\tau)\cdot\vec{r}_{tr}(\tau)d\tau}_{\varphi_{tr}(t)}}\, d\vec{r}_0
\end{aligned}
\tag{1.17}
$$

Two effects of motion on the received MR signal are observed in Eq. 1.17. First, the translation component $\vec{r}_{tr}(\tau)$ corresponds to a phase modulation of the MR signal:

$$\varphi_{tr}(t) = \gamma \int_0^t \vec{G}(\tau) \cdot \vec{r}_{tr}(\tau) \, d\tau \qquad [1.18]$$

Second, as obvious from a comparison of equations 1.12 and 1.17, the linear transformation A(t) that describes the object deformation can formally be interpreted as a modified k-space trajectory:

$$\vec{k}'(t) = \gamma \int_0^t A^T(\tau) \vec{G}(\tau) \, d\tau \qquad [1.19]$$

Hence, a modified k-space formalism is introduced that accounts for an affine object deformation in the spatial domain, which corresponds to a linear transformation in k-space. This property of the Fourier transform is referred to as the "Fourier similarity theorem" [bron97]. For instance, a contraction in the spatial domain corresponds to an expansion in k-space, and vice versa. Rotational motion is invariant in both domains [bron97], and a translation corresponds to a phase modulation $e^{-j\vec{k}\vec{r}_{tr}}$ of the acquired data ("Fourier shift theorem"). In conclusion, the received MR signal in the presence of motion can be described as in equation 1.20.

$$S'(t) = \int_{\vec{r}} m_{T,0}(\vec{r}) \, e^{-jA^T\vec{k}\vec{r}} \, d\vec{r}_0 \cdot e^{-j\vec{k} \cdot \vec{r}_{tr}} \, d\vec{r}_0 \qquad [1.20]$$

It is important to point out that the modified k-space formalism is only valid in the presence of affine motion patterns such as translations, expansion, rotation and shearing, which can be described by a linear transformation.

1.2.3 The point spread function (PSF)

For a closed-form description of the effect of motion on the reconstructed MR image, we consider an exemplary case where translational motion induces an undesired phase shift of the received MR signal (cf. Eq. 1.20):

$$\begin{aligned} S'(\vec{k}) &= \int_{\vec{r}} m(\vec{r}) e^{-j\vec{k}\vec{r}} d\vec{r} \cdot e^{-j\vec{k}\cdot\vec{r}_{tr}} \\ &= S(\vec{k}) \cdot e^{-j\vec{k}\vec{r}_{tr}} \\ &= S(\vec{k}) \cdot e^{-j\varphi_{tr}} \end{aligned}$$

[1.21]

In the presence of motion, Eq. 1.14 then becomes

$$m'(\vec{r}) = \mathcal{F}\{S'(\vec{k})\} = \mathcal{F}\{S(\vec{k}) \cdot e^{-j\varphi_{tr}(\vec{k})}\}$$

[1.22]

According to the Fourier theorem, a multiplication in k-space corresponds to a convolution in the spatial domain. Hence, Eq. 1.22 can be rewritten as

$$m'(\vec{r}) = \mathcal{F}\{S(\vec{k})\} * \mathcal{F}\{e^{-j\varphi_{tr}(\vec{k})}\}$$

[1.23]

where $\mathcal{F}\{S(\vec{k})\}$ corresponds to the image reconstructed from undisturbed data, and $\mathcal{F}\{e^{-j\varphi_{tr}(\vec{k})}\}$ corresponds to a convolution function that identifies the effect of motion. Hence, the reconstructed image can be described as the static image, which is reconstructed without the influence of motion, convoluted with a motion-induced function that is referred to as the point spread function (PSF):

$$m'(\vec{r}) = m(\vec{r}) * PSF(\vec{r})$$

[1.24]

Ideally, the PSF is a Dirac impulse, or the „identity“. Any deviation from the ideal case, such as imaging in the presence of motion, or the effect of undersampling, or the discrete data sampling process itself, can formally be described independently from the imaged object by means of the PSF. However, we will confine on the influence of motion for the time being.

A closed-form derivation of the PSF resulting from a translational, harmonic motion pattern of the imaged object is derived for a 2D acquisition in the following sections. An exemplary object translation in x-direction, i.e., along the readout direction, has the periodicity $T_{tr} = 2\pi / \omega_{tr}$ and is defined by

$$\vec{r}_{tr}(t) = \begin{bmatrix} x_{tr}(t) \\ 0 \\ 0 \end{bmatrix} \quad with \quad x_{tr}(t) = X_0 \sin(\omega_{tr} t) \qquad [1.25]$$

To describe the effect of motion during discrete data sampling, a discrete timing pattern is introduced:

$$t \rightarrow (n_x \Delta t_x + n_y T_R) \qquad [1.26]$$

where Δt_x is the sampling interval, and T_R is the repetition time, i.e., the time-distance between the acquisition of successive readouts. The indices n_x and n_y denote the consecutive numbers of the sampling points along one readout, and the number of the readout, respectively. Hence, Eq. 1.25 becomes

$$x_{tr}(t) = X_0 \sin\left(\omega_{tr}(n_x \Delta t_x + n_y T_R)\right) \qquad [1.27]$$

With Eq. 1.27, the motion-induced phase shift becomes

$$\begin{aligned} \varphi_{tr}(k_x, k_y) &= k_x x_{tr}(t) \\ &= k_x X_0 \sin\left(\omega(n_x \Delta t_x + n_y T_R)\right) \end{aligned} \qquad [1.28]$$

The indices n_x and n_y can be related to the spatial wavelength, λ, and the field of view (FOV) by Eq. 1.29:

$$k = \frac{2\pi}{\lambda} \quad \text{and} \quad FOV = n\lambda$$

$$\Rightarrow n_x = \frac{FOV_x k_x}{2\pi} \quad \text{and} \quad n_y = \frac{FOV_y k_y}{2\pi}$$

[1.29]

Hence, Eq. 1.28 becomes

$$\varphi_{tr}(k_x, k_y) = k_x X_0 \sin\left(\omega_{tr}(FOV_x k_x \Delta t_x + FOV_y k_y T_R)/2\pi\right)$$

[1.30]

An exponential expression of the phase shift following a sine function can be rewritten as a Fourier series [grad80]:

$$e^{-j\varphi_{tr}} = e^{-ja\sin(\theta)} = \sum_{\nu=-\infty}^{\infty} e^{-j\nu\theta} \cdot J_\nu(a)$$

[1.31]

where J_ν denotes the Bessel function of the ν-th order (Bessel sidebands). So in exponential notation, the motion-induced phase shift becomes

$$e^{-j\varphi_{tr}(k_x, k_y)} = \sum_{\nu=-\infty}^{\infty} e^{-j\nu\omega_{tr}(FOV_x k_x \Delta t_x + FOV_y k_y T_R)/2\pi} \cdot J_\nu(X_0 k_x)$$

[1.32]

To calculate the PSF, equation 1.32 is Fourier-transformed using the Fourier representation of an exponential oscillation, which is the delta function:

$$\mathcal{F}\{e^{-jk_x x_0}\} = 2\pi\,\delta(x - x_0)$$

[1.33]

Thus, the PSF becomes

$$PSF(x, y) = \sum_{-\infty}^{\infty} \delta(x - \nu x_g)\delta(y - \nu y_g) *_x \mathcal{F}\{J_\nu(2\pi X_0 k_x)\}$$

[1.34]

with the constants

$$x_g = \frac{\omega_{tr} FOV_x \Delta t_x}{2\pi} = FOV_x \frac{\Delta t_x}{T_{tr}} \quad \text{and} \quad y_g = \frac{\omega_{tr} FOV_y \Delta T_R}{2\pi} = FOV_y \frac{T_R}{T_{tr}} \qquad [1.35]$$

and the Fourier transform of the Bessel functions [haa86]

$$\mathcal{F}\{J_{ny}(2\pi X_0 k_x)\} = \begin{cases} \dfrac{2(-j)^{\nu} T_{\nu}(2\pi x / X_0)/X_0}{X_0 \sqrt{1-(2\pi x / X_0)^2}} & |x| > \dfrac{X_0}{2\pi} \\ 0 & |x| \leq \dfrac{X_0}{2\pi} \end{cases} \qquad [1.36]$$

where T_{ν} are the Tschebychev polynomials. Note, that the convolution given in Eq. 1.34 is one-dimensional in the direction of motion.

Hence, two effects are observed in the presence of motion, which are described by the PSF in equation 1.34. First, the convolution with the Fourier transform of the Bessel function results in a smearing, or „blurring", of the object structures in motion direction over the motion interval X_0. This blurring phenomenon entails a loss in resolution and image quality. More severely, the convolution of the image with the delta functions in Eq. 1.34 yields a periodic reproduction of the original image. This phenomenon is called ghosting. In general, a temporal periodicity of motion generates a spatial periodicity in the reconstructed image. The ghosting artifacts spread out perpendicular to the readout direction, and are independent of the motion direction. An example of artifacts resulting from periodic motion in a Cartesian acquisition is shown in Fig. 1.9 [b].

1.2.4 Motion-corrected MR imaging

Prospective motion correction with precompensated gradient waveforms

As it was previously described by Eq. 1.17, the influence of linear motion, which can be described in terms of a linear transformation matrix A (expansion, shearing, rotation) plus a translation r_{tr} yields a modified phase term in the expression for the received MR signal:

$$\varphi'(\vec{r},t)=\gamma\int_0^t\left[\left(A(\tau)^T\vec{G}(\tau)\right)\cdot\vec{r}+\vec{G}(\tau)\cdot r_{tr}(\tau)\right]d\tau \qquad [1.37]$$

The localization of the magnetization (spatial encoding) is included in the phase of the MR signal. Hence, in theory, the MR acquisition is motion-corrected if for each point in time and each signal source at $\vec{r}$, the effective MR signal phase is kept unchanged.

As it can easily be seen from Eq. 1.37, the affine transformation that expresses the motion pattern vanishes if a modified, precompensated gradient waveform $G_c(t)$ is applied [manke03]:

$$G_c(t)=\left(A^T(t)\right)^{-1}G(t) \qquad [1.38]$$

where $(A^T(t))^{-1}$ denotes the inverse matrix of $A^T(t)$, so equation 1.37 becomes

$$\varphi''(\vec{r},t)=\gamma\int_0^t\left[\left(\vec{G}_c(\tau)\right)\cdot\vec{r}+\vec{G}_c(\tau)\cdot r_{tr}(\tau)\right]d\tau \qquad [1.39]$$

Finally, to correct for the residual phase modulation resulting from the object translation, $r_{tr}(\tau)$, a complementary correction phase φ_c is introduced to restore the original signal phase, φ:

$$\varphi(t)=\varphi''(t,\vec{r})-\varphi_c(t) \qquad \text{where} \qquad \varphi_c(t)=\gamma\int_0^t\left(\left(A(\tau)^T\right)^{-1}\vec{G}(\tau)\right)\cdot\vec{r}_{tr}(\tau)d\tau \qquad [1.40]$$

For completeness, if the center of the transformation, $\vec{r}_0$, is not aligned with the iso-center of the gradient system, $\vec{0}$, the transformation applied for the compensated gradients yields a virtual shift of the object:

$$\Delta \vec{r}_0 = A \vec{r}_0 - \vec{r}_0 \qquad [1.41]$$

This additional shift has to be taken into account for the calculation of the complementary correction phase, $\varphi_c(t)$, in equation 1.40 to avoid an undesired virtual shift of the object as a result of the modified gradients.

Retrospective motion correction using regridding

As opposed to the prospective motion correction technique by means of precompensated gradient waveforms, a correction of motion is also possible as a post-processing step. As it was previously found in Eq. 1.19, motion during signal sampling corresponds to a modified k-space trajectory, $\vec{k}'(t)$. If the underlying motion model is known, the deviations between the ideal (motion-free) and actual k-space trajectory can be accounted for during image reconstruction as shown in Fig. 1.7.
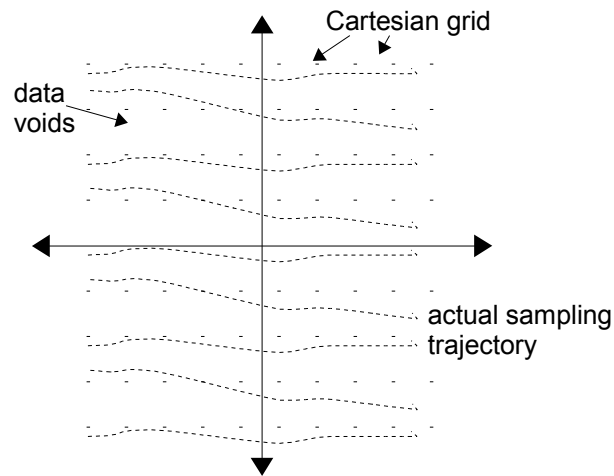
Fig 1.7 *Motion in MR imaging results in deviations between the ideal k-space sampling grids (dots) and the actual trajectory (dashed line). If the underlying motion pattern is known, the deviations can be accounted for during image reconstruction by means of „mapping" the data onto the correct position in k-space. However, regions with data overlap as well as regions with data voids (arrow) occur. The latter may potientially result in aliasing artifacts in the reconstructed image*

The retrospective approach results in an increased computational effort during image reconstruction, as the actual data in the presence of motion do not necessarily fall onto a rectangular (Cartesian) grid, and therefor they cannot be processed by means of the fast Fourier transform (FFT). However, non-Cartesian acquisition techniques, such as radial scanning techniques described in the following sections, require an image reconstruction from non-Cartesian data anyway, and efficient methods to interpolate these data onto a Cartesian grid exist [sul85].

1.2.5 Motion effects in non-Cartesian imaging techniques – radial scanning

The effect of motion described by Eq. 1.34 is valid for Fourier imaging of a general sinusoidally moving object. However, it cannot be directly applied to other imaging schemes with different k-space trajectories. For instance, the artifact level and shape may differ significantly if alternative k-space scanning techniques, such as a radial sampling trajectory with rotating readout orientations as illustrated in Fig. 1.8 [b], are employed.
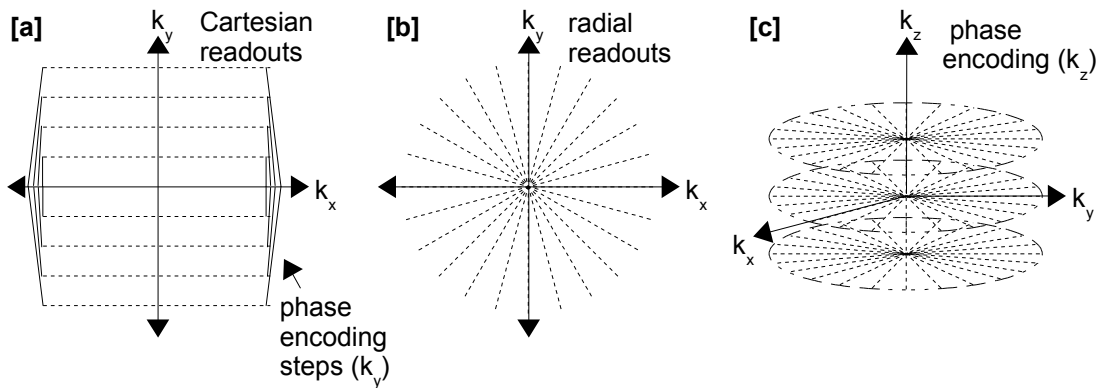
Fig 1.8 *Comparison of a Cartesian sampling pattern [a] and a radial acquisition [b]. In Cartesian sampling, k-space is traversed using an unidirectional readout gradient Gx, and successive readout lines are obtained by phase encoding gradients Gy applied prior to sampling. In radial sampling, [b], multidirectional readout gradients are applied to cover k-space in a radial fashion. A volumetric data set is obtained by adding a phase encoding gradient in the remaining spatial dimension ("stack of stars"), [c]*

In radial scanning, motion-induced data inconsistencies from one radial readout to another result in streaking (instead of ghosting) artifacts, with the amplitude smallest near the moving element, and often residing outside the anatomic boundaries of the subject [glov92]. For illustration, a reconstructed image using Cartesian and radial scanning of an object with a periodic motion pattern is shown in Fig. 1.9 [b] and [c], respectively.
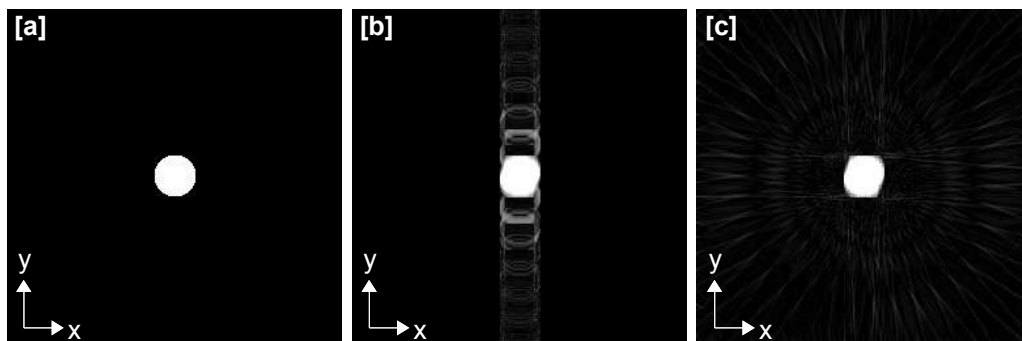
Fig 1.9 *Simulated results for a discoidal phantom [a]. Motion artifacts in a Cartesian acquisition [b] and radial scanning [c] for a moving discoidal phantom (motion in x-direction, amplitude = 6 pixel, periodicity = 20 / acquisition). In a Cartesian acquisition, discrete ghosts appear perpendicular to the readout direction. In radial scanning, motion artifacts are dispersed as streaks in all directions with a lower artifact amplitude when compared to Cartesian scanning*

In addition, a particular asset of radial scanning is that the acquisition is insensitive to motion that occurs perpendicular to the readout direction. For illustration, we reconsider Eq. 1.10 that describes the received baseband MR signal for a general object with the magnetization density $m_{T,0}(x,y)$:

$$S(t) = \int_0^{FOV_y} \int_0^{FOV_x} m_{T,0}(x,y) e^{-j\gamma \int_0^t (G_x(\tau) \cdot x + G_y(\tau) \cdot y) d\tau} dx\, dy \qquad [1.42]$$

In radial imaging, which is also referred to as frequency encoded imaging, successive frequency encoding gradients are applied in different directions, as illustrated in Fig 1.8 [b]. As opposed to Cartesian scanning, no phase encoding gradients are performed. If we consider the x-direction as the current readout direction, and the orthogonal gradient (G_y) integral is zero, equation 1.42 can be simplified to

$$S(t) = \int_0^{FOV_y} \int_0^{FOV_x} m_{T,0}(x,y) e^{-j\gamma \int_0^t (G_x(\tau) \cdot x) d\tau} dx\, dy \qquad [1.43]$$

Thus, if real-world effects such as B_0 and B_1 inhomogeneities are neglected, the signal that is received during a readout in x-direction is independent of the spin density localization in y-direction, as the y position is removed from the exponential phase expression in Eq. 1.43. Moreover, the acquisition is insensitive to translation or tissue expansion / contraction, as the integral of the magnetization density, or the total amount of magnetization along the y-dimensions is not affected by this subset of motion patterns. Hence, a radial acquisition is insensitive to motion (translation and expansion / contraction) which occurs perpendicular to the readout orientation.

In conclusion, radial scanning techniques have intrinsic advantages over Cartesian methods in the presence of motion, which is in good agreement with previous results described in the literature ([glov92], [ra94]). While motion correction (either prospective or retrospective) is generally possible for non-Cartesian methods as well, especially radial acquisition techniques exhibit a low sensitivity to motion to start with. Hence, these techniques are promising candidates for coronary MRA , which will be addressed in more detail the following sections.

1.3 Volumetric sampling with 3D-radial trajectories

In the previous section, radial scanning was found to exhibit a low sensitivity to motion, which is in good agreement with results in the literature [glov92]. Moreover, radial acquisitions have further specific advantages, such as a reduced sensitivity to undersampling [lau96]. For this reason, radial stack-of-stars techniques as shown in Fig. 1.8 [c] are well established for application in coronary MRA ([pet00], [spue04]) in the meantime. However, as a further interesting enhancement for CMRA, a volumetric, whole-heart coverage can be achieved by extending the current stack-of-stars acquisitions, which are radial in-plane, but Cartesian in the remaining phase encoding direction, to a true 3D radial acquisition as shown in Fig. 1.10. Thus, a volumetric data set with isotropic resolution can be obtained, while the beneficial assets of radial scanning are further accentuated. The mathematical supplements for such a scheme are provided in the following sections.

1.3.1 3D radial sampling of k-space

To achieve an isotropic coverage of k-space in all three spatial dimensions, the gradient orientations for the radial readouts need to be distributed equidistantly across the surface of a sphere. However, a perfectly equidistant distribution of points on the surface of a sphere is not trivial. An equivalent problem is encountered in electrostatics, when the positions of charges on a conducting sphere are need to be calculated by means of the Poisson equations. However, these calculations are complex, and do not even yield a solution for selected numbers of points, and are therefore not suitable for the present problem.

However, a nearly isotropic coverage of k-space with radial sampling in 3D can be achieved by distributing the end points of all projections, or the readout gradient orientations, respectively, along a spiral running on a sphere from one pole to the equator [won94]. This parameterization was chosen because it provides nearly isotropic k-space coverage for an arbitrary number of readouts. Furthermore, it requires only small changes of the gradient orientations between successive readout, which reduces eddy currents related to gradient switching. The latter aspect is of great importance [sche03] for fully refocused MR sequences, such as steady-state free precession [opp86]. Furthermore, the calculation of the gradient orientations is simple enough to be performed at runtime.

Per definition, a 3D radial acquisition comprises N readouts, and the corresponding normalized readout gradient components G_x, G_y, G_z described by Eq. 1.44 and 1.45, respectively.

$$G_x(n) = \cos(\varphi) \cdot \sqrt{(1 - G_z{}^2(n))}$$

$$G_y(n) = \sin(\varphi) \cdot \sqrt{(1 - G_z{}^2(n))}$$

$$G_z(n) = \frac{(n - 0.5)}{N} - 1$$

[1.44]

with

$$\varphi = \sqrt{(2 \cdot \pi \cdot N)} \cdot \sin^{-1}(G_z)$$

[1.45]

In Eq. 1.44, n = (1..N) denotes the index of the current readout. The resulting trajectories are illustrated in Fig. 1.10. The main feature of the given trajectory, which resembles the sampling distribution proposed in [won94], but only covers one half of the sphere, is that the horizontal distance between two trajectory starting points is equal to the vertical distance of the spiral passes, which yields a near-isotropic coverage of k-space.
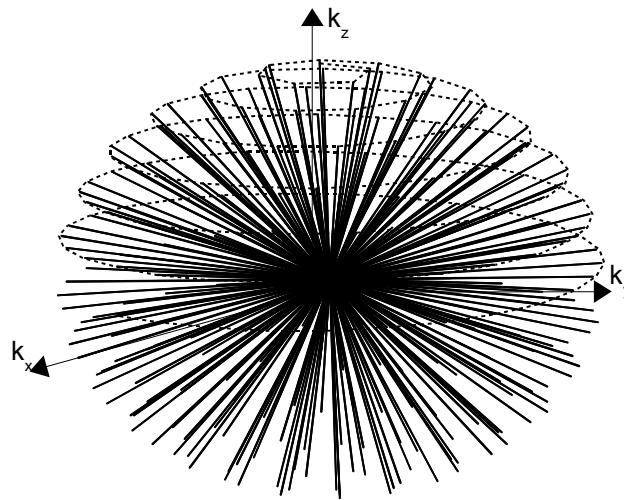
Fig. 1.10 *Nearly isotropic, 3D radial sampling pattern. The center of k-space is densely sampled, as each radial sampling trajectory (solid line) passes the k-space origin. The periphery is sparsely sampled. The successive gradient orientations of the radial readouts form a spiral on the surface of a sphere from the pole to the equator (dotted line). The horizontal distance between two trajectory starting points is equal to the vertical distance of the spiral passes*

The overall anisotropy of the distribution, measured by the standard deviation σ of the distance between adjacent points on the sphere, is less than 10% for a total number of projections $N > 100$ [won94].

1.3.2 Reconstruction of non-Cartesian k-space data using gridding

Gridding - aside from the previously described 3D radial acquisition, there are many alternatives to Cartesian acquisition methods. The main disadvantage with these methods is the difficulty of reconstructing the resulting data sets. As the data do not fall on a regular Cartesian grid in spatial-frequency space, the reconstruction cannot be performed with a fast Fourier transform (FFT). In principle, the non-Cartesian data can be demodulated point-by-point with the discrete Fourier transform (DFT). However, in numerical measures, this approach is very slow. A faster approach, which will be referred to as "gridding" ([sul85], [mey92], [schom95], [ra99]), is discussed in the following section; the data are first interpolated onto a regular Cartesian grid, and then the FFT is used to reconstruct an image.

The basic idea [pauly] of gridding is to convolve each data point with an appropriate gridding kernel [jack91], which is chosen to be wide enough to extend to the neighboring grid points, but as small as possible to keep computation times short. This algorithm accumulates the contribution of each data sample to the surrounding grid points on the Cartesian mesh. The basic procedure is illustrated in Fig. 1.11. After all samples have been processed, the FFT produces a reconstructed image. Finally, a division by the Fourier-transformed gridding kernel is necessary to eliminate undesired shading of the image.
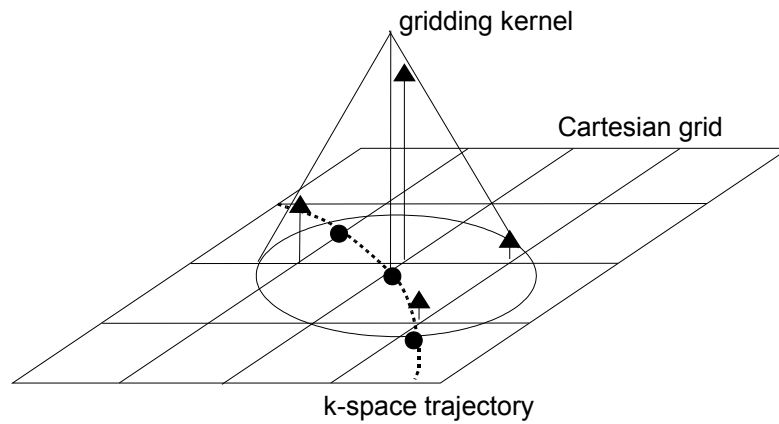
Fig. 1.11 *Scheme of a 2D gridding procedure for a 2D acquisition. The data samples line on an arbitrary trajectory through k-space (dashed line). The sampled data points are convolved with a gridding kernel and resampled on the cartesian grid (arrows)*

The three-dimensional version of gridding that has been implemented in the present work can be described mathematically. The non-Cartesian sampling function $S_{NC}(k_x, k_y, k_z)$ is given in Eq. 1.46.

$$S_{NC}(k_x, k_y, k_z) = \sum_i^3 \delta\left(\frac{(k_x - k_{x,i})}{\Delta k_x}, \frac{(k_y - k_{y,i})}{\Delta k_y}, \frac{(k_z - k_{z,i})}{\Delta k_z}\right) \qquad [1.46]$$

In Eq. 1.46, δ denotes the delta function. The non-Cartesian data $M_{NC}(k_x, k_y, k_z)$ are convolved with the gridding kernel $C(k_x, k_y, k_z)$ and then resampled on the Cartesian grid (cf. Eq. 1.47).

$$M_C = \left[\left(M_{NC}(k_x, k_y, k_z) \cdot S_{NC}(k_x, k_y, k_z)\right) * C(k_x, k_y, k_z)\right]$$
$$\cdot S_C\left(\frac{k_x}{\Delta k_x}, \frac{k_y}{\Delta k_y}, \frac{k_z}{\Delta k_z}\right) \qquad [1.47]$$

After the Fourier transform of the resampled Cartesian data, M_C, Eq. 1.47 results in Eq. 1.48, where FOV_x, FOV_y, and FOV_z are the field of views in x, y, and z direction, respectively.

$$m_C(x, y, z) = \left[\left(m(x, y, z) * s_C(x, y, z)\right) \cdot c(x, y)\right] * s_C\left(\frac{x}{FOV_x}, \frac{y}{FOV_y}, \frac{z}{FOV_z}\right) \quad [1.48]$$

Effects of gridding in image space - as evident from Eq. 1.48, two side effects are observed as a consequence of the gridding algorithm. First, the discrete sampling of the data on the Cartesian grid corresponds to a convolution with an equally spaced three-dimensional comb function, s_C, which produces periodic replication of the image at a distance of the FOV. This entails the undesired consequence that side lobes from the periodic replicas in the spatial domain, which are inherent to discrete data sampling in k-space, may "leak" into the reconstructed image (cf. Fig. 1.12). However, this problem can be addressed by oversampling the k-space data on a more dense grid, i.e., virtually increasing the sampled FOV, which will move the side lobes further away from the original image [pauly].
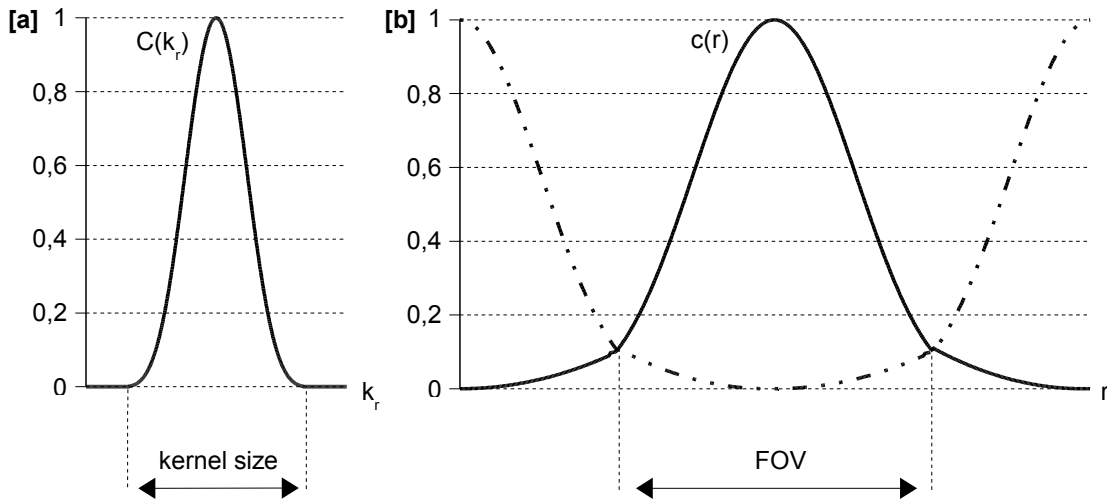
Fig. 1.12 *Function pair of a gridding kernel in k-space [a] based on a Kaiser-Bessel window, and the corresponding apodization function in the spatial domain [b]. Due to the finite extent of the gridding kernel, sidelobes from the periodic replicas (dotted line, [b]) may leak into the actual FOV. However, the distance between aliased replicas can be increased by using oversampling during image reconstruction*

Second, the resulting image is multiplied, or apodized, respectively, by the Fourier transform of the gridding kernel, c(x, y, z), resulting in undesired shading of the image. However, this function can be determined numerically, and an entirely homogeneous representation of the image is obtained by dividing the reconstructed data by the Fourier transform of the gridding kernel. However, in practice, it might be advantageous [pauly] to divide out only a part of c(x, y, z), because gridding artifacts such as the above mentioned side lobes from aliased replicas at the edge of the field of view get accentuated by the deapodization. Hence, in this work, a modified deapodization function d(x, y, z) was applied, which incorporates an empirical attenuation component, a (cf. Eq. 1.49).

$$d(x,y,z) = \frac{1}{c(x,y,z)+a} \qquad [1.49]$$

Selection of a convolution kernel - The selection of an appropriate convolution kernel has been addressed in the literature ([sul85], [jack91], [schom95]). For Cartesian data, the ideal gridding kernel is the three-dimensional sinc function, which performs an optimal interpolation of the sampled k-space data (Eq. 1.50).

$$C_{sinc}(k_y, k_y, k_z) = sinc\left(\frac{k_X}{\Delta k_x}\right) \cdot sinc\left(\frac{k_y}{\Delta k_y}\right) \cdot sinc\left(\frac{k_z}{\Delta k_z}\right) \qquad [1.50]$$

The corresponding Fourier transform c(x, y, z) is given in Eq. 1.51.

$$c_{sinc}(x, y, z) = rect\left(\frac{x}{FOV}\right) \cdot rect\left(\frac{y}{FOV}\right) \cdot rect\left(\frac{z}{FOV}\right) \qquad [1.51]$$

making deapodization superfluous. Unfortunately, the gridding kernel would be infinite in extent and therefore computationally impractical [pauly]. To abbreviate computation time, it is desirable to keep the gridding kernel small. On the other hand, a finite convolving function will contribute side lobes, which are aliased back into the image by the comb function, S_C, as discussed in the previous section. A good trade-off between these two constraints, namely the extent of the gridding kernel in the spatial-frequency domain, and the shape and amplitude of the side lobes in the image domain, is achieved with a three-dimensional Kaiser-Bessel function $C_{KB}(k_x) = C_{KB}(k_y) = C_{KB}(k_z) = C_{KB}(k_r)$, where the three orthogonal convolution functions are based on J_0, the zero-order modified Bessel function of the first kind [jack91].

$$C_{KB}(k_r) = \frac{1}{W} \cdot J_0\left(\beta\sqrt{1 - \left(\frac{2k}{W}\right)^2}\right) \qquad [1.52]$$

In Eq. 1.52, W denotes the kernel width, and β is a free design parameter that may be varied to determine the best possible performance. The inverse transform in image domain, $c_{KB}(x) = c_{KB}(y) = c_{KB}(z) = c_{KB}(r)$ is described by Eq. 1.53.

$$c_{KB}(r) = \frac{\sin\left(\sqrt{\pi^2 W^2 r^2 - \beta^2}\right)}{\left(\sqrt{\pi^2 W^2 r^2 - \beta^2}\right)} \qquad [1.53]$$

The function pair $C_{KB}(k_r)$ and $c_{KB}(r)$ is plotted in Fig. 1.12 for further illustration.

1.3.3 Density correction and SNR considerations for 3D radial sampling

One processing step that becomes necessary prior to the gridding procedure is to compensate for the non-uniform sampling density ([hoge97], [pipe00]), especially in a 3D radial acquisition. As evident from the sampling pattern plotted in Fig. 1.10, the sampling density is much higher in the center of k-space than in the periphery. Hence, some weighting must be included to account for the sampling density. This compensation is usually performed for each data point before the gridding operation, which is referred to as precompensation [pauly] using an appropriate weighting function, $W(k_x, k_y, k_z)$:

$$M_C = \left[(M_{NC}(k_x, k_y, k_z) \cdot W(k_x, k_y, k_z) \cdot S_{NC}(k_x, k_y, k_z)) * C(k_x, k_y, k_z) \right]$$
$$\cdot S_C\left(\frac{k_x}{\Delta k_x}, \frac{k_y}{\Delta k_y}, \frac{k_z}{\Delta k_z} \right) \qquad [1.54]$$

The appropriate weighting function is proportional to the k-space volume that is associated with each sample [ra99]. If we assume an ideal, isotropic 3D radial sampling pattern, this volume can be computed geometrically. Samples are located along radii at multiples of $\Delta k_x = \Delta k_y = \Delta k_z = \Delta k_r$. If N readouts are acquired in total, the central sample is acquired N times. For this sample, the weight is 1/N, multiplied by the volume of the central sphere with the radius $\Delta k_r / 2$ around that sample:

$$W_0 = \frac{4}{3N} \cdot \pi \cdot \left(\frac{\Delta k_r}{2} \right)^3 = \frac{\pi (\Delta k_r)^3}{3N} \cdot \frac{1}{2} \qquad [1.55]$$

The weighting for the first sample is given by the volume in the next annular surface outside the central sphere, divided by the number of samples:

$$W_1 = \frac{4}{3N} \pi \left[\left(\frac{3 \Delta k_r}{2} \right)^3 - \left(\frac{\Delta k_r}{2} \right)^3 \right] = \frac{\pi (\Delta k_r)^3}{3N} \cdot 13 \qquad [1.56]$$

For the i-th sample, the weighting becomes

$$W_i = \frac{4}{3N}\pi\left[\left(\frac{(2i+1)\Delta k_r}{2}\right)^3 - \left(\frac{(2i-1)\Delta k_r}{2}\right)^3\right] = \frac{\pi(\Delta k_r)^3}{3N}\cdot(12i^2+1)$$ [1.57]

Hence, the weighting is approximately quadratic as expected, but does not go to zero at the origin to obtain an appropriate DC value for the reconstructed image.

However, one drawback of the strongly non-uniform weighting that is necessary to compensate for the sampling density is that this process entails a loss in the overall signal-to-noise ratio (SNR) of the reconstructed image [pipe95], which will be derived in a quantitative manner in the following section. For simplicity, a quadratic weighting function, $W_i = i^2$, will be assumed for the following considerations. Furthermore, the resulting error (E, cf. Eq. 1.58) is calculated according to the error propagation from the error e_i of each individual data sample [vla02], which is weighted with the weighting function W_i.

$$E = \sqrt{\sum_{n=1}^{N}\sum_{i=1}^{I}(W_i \cdot e_i)^2}$$ [1.58]

In Eq. 1.58, n = 1..N is the index of the radial readout, and i = 1..I is the index of the acquired sample along one radial readout. It is assumed that the intrinsic error, or the noise inherent to each data sample, is uniform for all acquired data, so with e_i = const. = e, Eq. 1.58 becomes

$$E = e\cdot\sqrt{\sum_{n=1}^{N}\sum_{i=1}^{I}i^4}$$ [1.59]

The cumulative value of the finite series [bron97] can be rewritten as

$$E = e\cdot\sqrt{N\cdot I}\cdot\sqrt{\frac{(I+1)(2I+1)(3I^2+3I-1)}{30}}$$ [1.60]

Opposed to the quadratic weighting in a 3D radial acquisition, a Cartesian sampling pattern requires uniform weights, W_C, for all data samples. To allow for a comparison with the 3D radial acquisition, the total sum of weights should be equal for both sampling schemes.

$$\sum_{n=1}^{N} \sum_{i=1}^{I} W_C = \sum_{n=1}^{N} \sum_{i=1}^{I} W_i \qquad [1.61]$$

Combining Eq. 1.61 with the quadratic weights $W_i = i^2$ and solving the finite series according to [bron97] yields

$$W_C = \frac{(I+1)(2I+1)}{6} \qquad [1.62]$$

Combining equations 1.58 and 1.62 yields the resulting error for a Cartesian acquisition, E_C:

$$E_C = e \cdot \sqrt{(N \cdot I)} \cdot \frac{(I+1)(2I+1)}{6} \qquad [1.63]$$

The ratio of the errors in a radial acquisition, E_R, and a Cartesian acquisition, E_C, becomes

$$\frac{E_R}{E_C} = \frac{\sqrt{\dfrac{(I+1)(2I+1)(3I^2+3I-1)}{30}}}{\dfrac{(I+1)(2I+1)}{6}} = \sqrt{\frac{6}{5} \cdot \frac{(3I^2+3I-1)}{(2I^2+3I+1)}} \qquad [1.64]$$

For a large number of samples along one readout (I>>1), the quadratic term dominates, and Eq. 1.64 becomes

$$\frac{E_R}{E_C} \approx \sqrt{\frac{6}{5} \cdot \frac{3I^2}{2I^2}} = \sqrt{\frac{9}{5}} \qquad [1.65]$$

The ratio of the resulting error, or noise, respectively, shows that only 75% of the available SNR is obtained using 3D radial sampling, when compared to an equivalent Cartesian acquisition. These losses in SNR are an inherent property of the radial acquisition and have to be offset in practice by other advantages of radial sampling to justify its use. Moreover, it requires a high signal level to start with, which calls for the use of multiple surface coils for

signal reception and of adequate sequences. However, the available SNR level for the envisaged application, namely a volumetric whole-heart acquisition, can be considered sufficient to offset the above mentioned SNR losses, as a large volume is acquired, yielding a high signal level to start with. Furthermore, some SNR can be recovered by a more advanced weighting approach, which will be discussed in more detail in the following section.

1.3.4 Data-driven weighting functions for arbitrary sampling patterns

As discussed in the previous section, the strongly non-uniform weighting function necessary to compensate for the sampling density entails a considerable loss in SNR. In more detail, the available SNR in the reconstructed image is inversely proportional to the variance of the data weights [pipe00]. Hence, it appears desirable to employ a weighting function with reduced variance when compared to the straightforward quadratic weighting approach, which overweights the data sampled in the periphery of k-space.

One possible approach [pipe99] that provides an improved SNR is to consider the correlation between data samples, and not exclusively the pure sampling density. For illustration, we consider a very sparsely sampled radial acquisition as shown in Fig. 1.13.
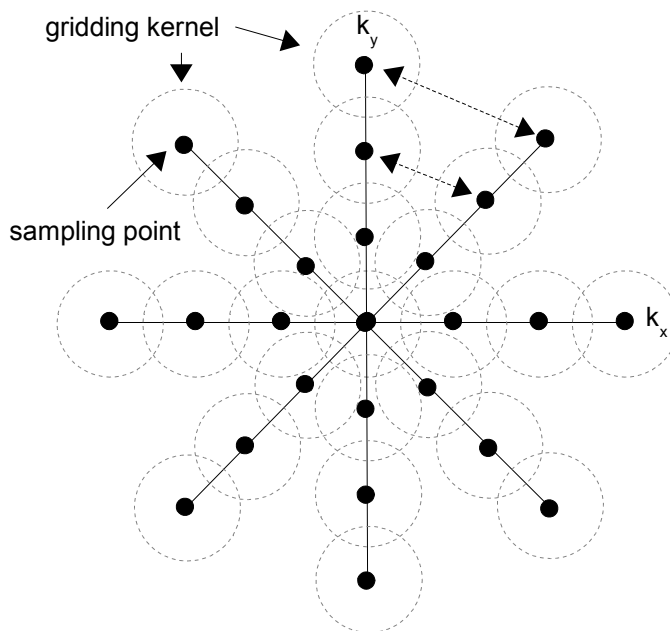
Fig. 1.13 *2D-example of a sparsely sampled radial sampling distribution. While the k-space origin is densely sampled, the distance between adjacent radial readouts increases with the radii from the origin. From a certain point (dotted arrow) on, the radial trajectories are too far apart, and there is no inter-trajectory correlation of the data, but only between neighbouring samples along one radial readout*

While the k-space origin is densely sampled, the distance between adjacent radial readouts increases with the radii from the origin. From a certain point on, the radial trajectories are too far apart (dotted arrow), and there is no inter-trajectory correlation of the data, but only between neighboring samples along one radial readout. To improve SNR, it is reasonable [pipe95] to keep the data weights constant from this point on, and not to increase the weighting according to the straightforward quadratic weighting function.

This basic idea has been investigated in this work using an iterative procedure similar to [pipe99] to calculate an appropriate weight for each data sample during the gridding procedure. First, an initial set of weights $W_0(\vec{k})$ with uniform weights for all data points along the radial trajectories of the given sampling pattern is assumed. Next, the data are gridded to the Cartesian grid. Due to the dense sampling in the k-space origin, an accumulation of data is produced by the gridding procedure towards the k-space origin. Next, the data are projected back onto the radial trajectories (inverse gridding). This will result in an estimate of the actual correlation of the data samples along the radial sampling pattern [pauly]. An approximate set of weights $W_{appr}(\vec{k})$ to compensate for the correlation between data samples is then obtained by a point-by-point division of the initial, uniform set of weights with the outcome of the forward and reverse gridding process, $W_1(\vec{k})$:

$$W_{appr}\left(\vec{k}\right) = \frac{W_0\left(\vec{k}\right)}{W_1\left(\vec{k}\right)} \qquad [1.66]$$

The result can be further improved in an iterative manner by taking the approximate solution as the input for a further forward and reverse gridding procedure:

$$W_{(n+1)}(\vec{k}) = \frac{W_{(n-1)}(\vec{k})}{W_n(\vec{k})} \qquad [1.67]$$

The iteration can be terminated by means of a convergence criterion, or, more simple, after a fixed number of iteration steps. Furthermore, it is not necessary to start with the unity matrix as the initial weighting estimate. Instead, the "analytical", quadratic weighting function is a good initial estimate. In that case, one single iteration will produce a very close approximation to the

desired weighting function to compensate for the correlation between data samples. For illustration, the analytical, quadratic weighting function (dotted line) is plotted in Fig. 1.14. The weighting function obtained with the iterative procedure is shown as a solid line in the same plot. The numerical result resembles the analytical result for the inner part of k-space, but flattens towards the outer part of k-space, which is in good agreement with the results in [pipe99] for a 2D radial acquisition.
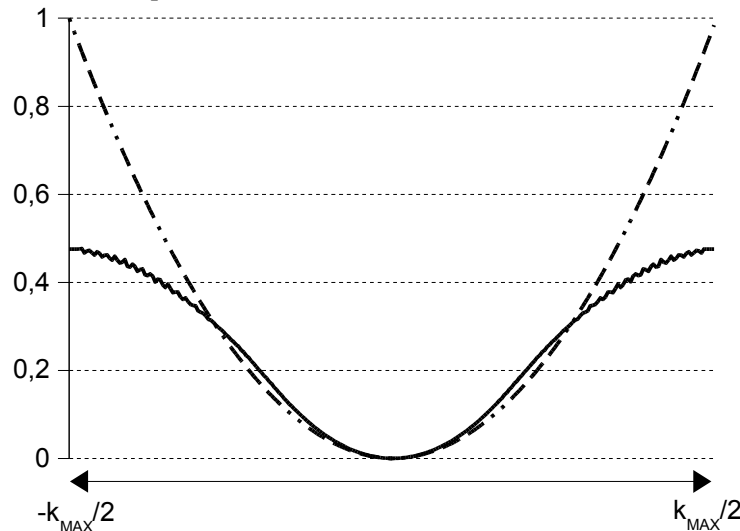
Fig. 1.14 *Weighting functions for a single projection of a 3D radial acquisition. Dashed line: analytical (quadratic) weighting function based on the sampling density. Solid line: iteratively calculated set of weights for one projection, based on the correlation between data samples. For the iteratively calculated set of weights, the weighting function flattens in the k-space periphery as the distance between two neighbouring radial trajectories exceeds the size of the gridding kernel*

The resulting weighting function obtained from the data-driven iteration as shown in Fig. 1.14 is provides an improved SNR for two reasons. First, high spatial frequency components are less overweighted when compared to the straightforward quadratic weighting, which corresponds to a lowpass filtering effect, theoretically at the expense of a slight decrease in resolution. Second, an increased in SNR results from the reduced variance of the data weights obtained with the iterative procedure. An overview of the available SNR using different weighting functions and sampling densities is given in Table 1.1.

There is an additional, desired side-effect related to the iterative weighting procedure. The computations are entirely data-driven and do not base on geometry, which allows for the calculation of weights for arbitrary sampling patterns. This is particularly beneficial if non-

isotropic sampling schemes are employed. In practice, even for the 3D radial sampling pattern, non-isotropies may occur, for instance if the acquisition is split into multiple interleaves. The resulting inappropriate weighting may result in artifacts in the reconstructed image. For illustration, an image (matrix size 256) reconstructed from 16,384 projections is shown in Fig. 1.15 [a]. For comparison, the sampling scheme was subdivided into 512 interleaves, where 32 projections were acquired in each interleaf. These measure might be necessary for specific applications, such as the self-navigated image reconstruction that is discussed in more detail in a following section. However, interleaving the acquisition results in a slight non-isotropy of the sampling pattern [won94]. If the straightforward weighting approach with uniform weighting functions for all readouts is employed, artifacts appear in the reconstructed image (cf. Fig. 1.15 [b]) as a small non-zero background signal. However, these artifacts can be reduced considerably if the iterative weighting procedure that provides an appropriate weight for each data sample is employed. The corresponding reconstructed image is shown in Fig. 1.15 [c].
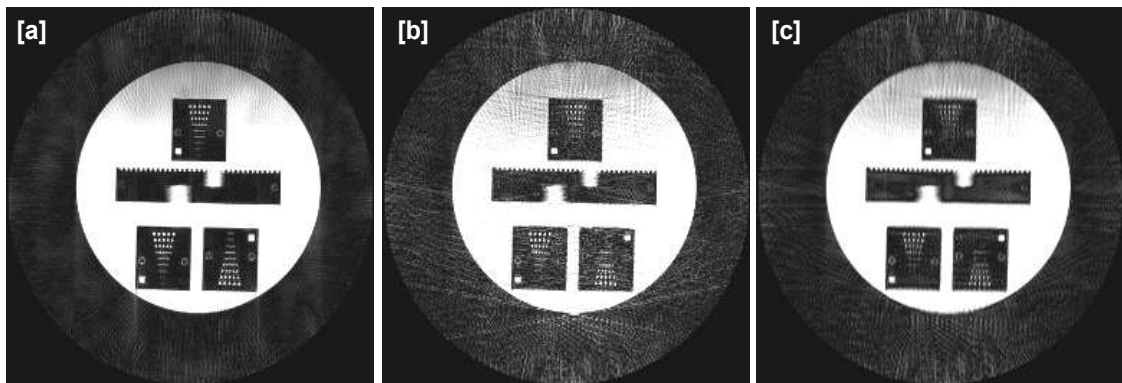
Fig 1.15   One slice through a phantom acquired with 3D radial sampling (matrix size 256, 25% sampling density) is shown in [a]-[c]. In [a], the data was acquired in one interleaf. In [b] and [c], the acquisition was subdivided into 512 interleaves, where each interleaf comprises 32 radial echoes. If the resulting non-isotropy of the sampling pattern is not taken into account during data weighting, artifacts such as streaking and a non-zero background signal appear in the reconstructed image, as shown in [b]. These artifacts can be reduced considerably using appropriate weighting obtained with the iterative weighting approach [c]

1.3.5 Off-center acquisition and motion correction in 3D radial sampling

Depending on the anatomy and application of the 3D radial acquisition, it may be desirable to position the acquired volume off-center. The excitation pulse needs to be translated in frequency by an appropriate shift Δf_{tr} for this purpose.

$$\Delta f_{tr} = \gamma \cdot G_s \cdot \Delta s \qquad\qquad [1.68]$$

where γ denotes the gyromagnetic ratio, and G_s is the strength of the slice selection gradient. Furthermore, the acquired echoes need to be shifted in frequency by an appropriate demodulation frequency Δf_{rc}.

$$\Delta f_{rc} = \gamma \left(G_M \cdot \cos(\varphi)\sin(\vartheta) \cdot \Delta m + G_P \cdot \sin(\varphi)\sin(\vartheta) \cdot \Delta p + G_S \cdot \cos(\vartheta) \cdot \Delta s \right) \qquad [1.69]$$

where G_M and G_P denote the gradients strength in the remaining orthogonal directions, and φ and ϑ denote the polar and azimuthal angle in the gradient coordinate system defined by the (m, p, s)-orientation. To shift the acquired volume by the desired off-center distances, the appropriate offset values for Δm, Δp and Δs are kept constant during the acquisition.

A further application of the demodulation technique is to dynamically shift the acquisition during scanning to cope with translational motion, such as that induced by respiration. If respiratory-induced translational motion can be measured during the acquisition, for instance using respiratory navigator pulses, the acquisition can be motion-corrected prospectively by decomposing the displacement to the (Δm Δp Δs) components in the gradient coordinate system.

Furthermore, it is possible to shift the acquisition retrospectively, i.e., after completing the scans, by shifting the linear phase by an angle increment $\Delta \beta$ of the acquired echoes according to the Fourier shift theorem:

$$\Delta \beta = \frac{2\pi}{I} \left(\Delta m \cdot \cos(\varphi)\sin(\vartheta) + \Delta p \cdot \sin(\varphi)\sin(\vartheta) + \Delta s \cdot \cos(\vartheta) \right) \qquad [1.70]$$

where Δm, Δp, and Δs are the displacements (measured in pixels), and I is the number of samples along one readout. Unlike the prospective correction, the retrospective correction does not allow for a translation of the excitation pulse along the slice direction as described in Eq. 1.69. However, in practice, it can be assumed that due to the large volumetric coverage of the 3D radial acquisition, the region of interest is always included in the imaged volume. Thus, a retrospective correction of rigid-body motion is feasible.

1.3.6 Effect of polar undersampling in a 3D radial acquisition

Aside from the low sensitivity to motion, the major motivation to incorporate radial sampling for coronary MRA within this work was its capability to reconstruct images from undersampled k-space data with surprising little aliasing artifacts, which has previously been described in detail in the literature [bar02]. This particular asset is investigated in a quantitative manner by means of the point-spread-function (PSF) for a true 3D-radial acquisition in this section.

  Strictly speaking, a 3D radial acquisition would require significantly more readouts than an equivalent Cartesian acquisition to ensure sufficiently dense sampling in all parts of k-space according to the Nyquist limit. If a cubic matrix of size N x N x N is acquired, and N sampling points are distributed along one readout, then N² readouts are necessary in total for a Cartesian acquisition, which corresponds to the surface area of one face of the cube. For a 3D radial acquisition, the area of one half-sphere needs to be covered with an equivalent density of readouts. Hence, $0.5 \cdot 4\pi \cdot (N/2)^2 = \pi/2 \; N^2$ readouts were necessary, theoretically resulting in a scan time increase of 57% when compared to an equivalent Cartesian acquisition.

  However, a radial acquisition is less prone to artifacts resulting from polar undersampling when compared to undersampling in a Cartesian acquisition. This is due to the fact that the k-space center, which contains the most relevant information for the reconstructed image, is still densely sampled, while undersampling is confined to the k-space periphery that contributes very little information to the reconstructed image.

  A quantitative approach to describe image artifacts and to judge the effect of polar undersampling is to calculate the point-spread-function (PSF). Ideally, the PSF should consist of one delta function in the center of image space. However, real-world image artifacts can best be described by the broadening of the central peak (blurring), or side lobes (ghosts / aliasing). For a qualitative comparison of the effect of undersampling, the central slice of the PSF for an undersampled Cartesian and 3D radial acquisition are shown in Fig. 1.16 [a] and [b],

respectively. In Fig. 1.16 [a], the PSF of a Cartesian acquisition with an undersampling factor of three, i.e., two out of three phase encoding steps were left out, is shown. This generates two extra peaks in the PSF, which will produce replicas of the acquired object within the reconstructed image that may completely mask relevant details of the image. In Fig. 1.16 [b], the PSF of an undersampled 3D radial acquisition is shown. To accentuate the effect of undersampling, a vastly undersampled acquisition comprising only 12.5% of the readouts compared to a fully sampled Cartesian acquisition was simulated. This corresponds to a maximal inter-trajectory distance $\Delta k_{it, max}$ in the periphery of k-space.

$$\Delta k_{it, max} = \sqrt{\frac{0.5\pi}{0.125}} = 3.54 \qquad [1.71]$$

In Eq. 1.71, $\Delta k_{it} = 1$ corresponds to the Nyquist distance that were necessary to exclude aliasing. To accentuate aliasing effects for the undersampled 3D radial acquisition shown in Fig. 1.16[b], the PSF is shown on a logarithmic scale for an improved visualization of low-amplitude components.

[a] PSF

2 FOV_y

2 FOV_x

[b] PSF [dB]

2 FOV_y

2 FOV_x
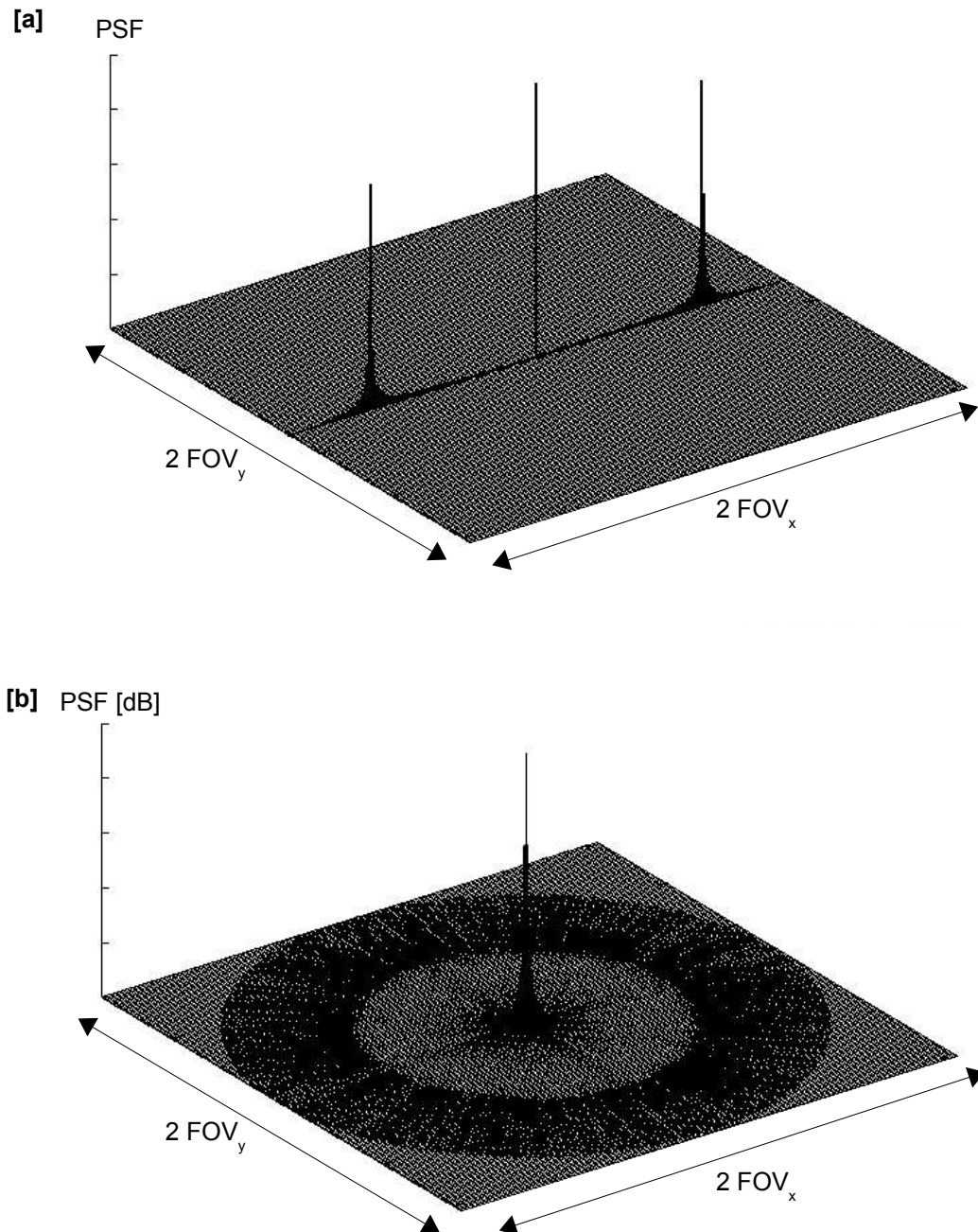
Fig. 1.16 *The central slice of the point spread function (PSF) resulting from an undersampled, three-dimensional acquisition is plotted in Fig. 1.11 [a] and [b], respectively. In [a], the PSF of a Cartesian acquisition with an undersampling factor of 3 (two out of three phase encoding steps were left out) is shown. The undersampling results in two extra peaks in the PSF, which will reproduce aliased representations of the object within the reconstructed image ("ghosts"). In [b], the PSF of a 3D radial acquisition with 8-fold undersampling is shown. Only 12.5% of the readouts neccessary for a Cartesian scan were acquired in this example. However, in the given, radial sampling pattern, aliased energy does not appear as discrete peaks, but as "smeared" streaks in radial direction with a low amplitude. This may introduce minor blurring and streaking artifacts, but no ghosts as observed in the Cartesian acquisition. In [b], the PSF was converted to a logarithmic scale (dB) for improved visualization of low-amplitude components*

In radial scanning, aliased energy does not appear as discrete peaks, but is "smeared" as low-amplitude streaks in radial direction. This may introduce minor blurring and streaking artifacts, but not discrete ghosts as observed in the undersampled Cartesian acquisition. For a quantitative evaluation of the PSF for different sampling densities in a 3D radial acquisition, one profile across the PSF, which is considered radially symmetric in all three spatial dimensions, is shown in Fig. 1.17. Again, the data are shown in a logarithmic scale to improve the visualization of low-amplitude components. The reference PSF for a fully sampled acquisition (157%, where 100% corresponds to a fully sampled Cartesian acquisition) is plotted as a solid line, while the PSFs for different sampling densities are shown as dotted lines in the same plot.
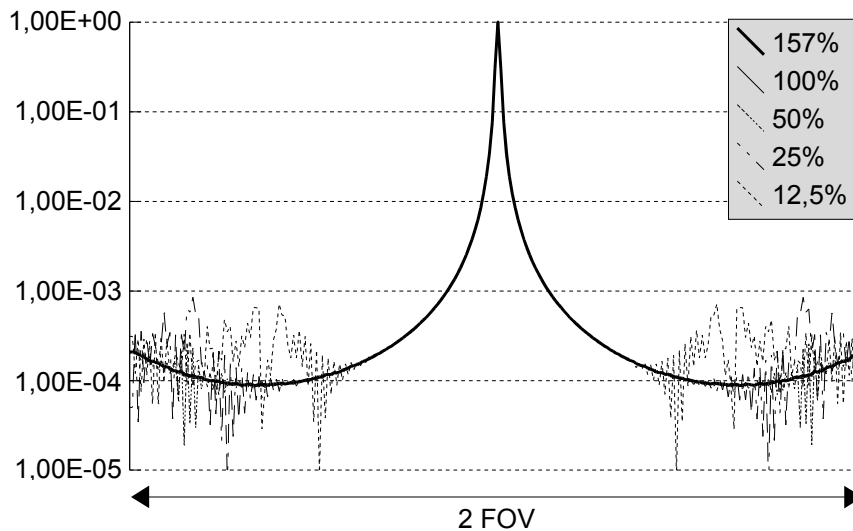
Fig. 1.17 *One profile across the radially symmetrical point spread function is shown for a 3D radial acquisition using different undersampling factors. One example for a fully sampled acquisition according to the Nyquist critereon is plotted as a thick line, while successively undersampled examples are shown as dotted lines in the same plot. Even for the lowest simulated sampling density of 12.5%, the amplitude of the side lobes is limited to 0.1% of that of the central peak. The plot is shown in a logarithmic scale to improve the visualization of low-amplitude components*

Even for the lowest simulated sampling density (12.5%), the amplitude of the side lobes is limited to 0.1% of that of the central peak. Also, no broadening of the central peak was observed, which indicates that spatial resolution is maintained even at a high degree of

undersampling. Thus, it is a particular asset of the 3D radial acquisition that undersampling to a large extent has a very small impact on image quality, which offers a great potential to reduce scan time without the need for advanced parallel imaging methods such as SENSE [prue99] or GRAPPA [gris02], which require a-priory information by means of coil sensitivity maps to reconstruct artifact-free images from undersampled k-space data.

However, by any means, undersampling will also affect the available SNR in the final image, which can be expressed as in Eq. 1.72:

$$SNR = \kappa \, dV \, \sqrt{(T_S)} \qquad\qquad [1.72]$$

where κ is a constant, dV is the voxel volume, an T_S is the total scan time of the imaging technique. Since the total scan time decreases linearly with the sampling density, a decrease in SNR following the root of the sampling density is expected. Hence, for the available SNR in the final image, the sampling density needs to be taken into account. An overview of the available SNR for different sampling densities and weighting approaches is given in Table 1.1, where 100% corresponds to the available SNR in a fully sampled Cartesian acquisition.

Table 1.1 *Numerically calculated results for the SNR using different sampling densities and weighting functions. Wa denotes the analytical, quadratic weighting function, and Wi denotes the iteratively calculated set of weights.*

Sampling density	SNR (Wa)	SNR (Wi)
100,0%	75,00%	75,00%
50,0%	53,00%	53,00%
25,0%	37,00%	38,00%
12,5%	26,00%	29,00%

The results of the simulations have shown that the 3D radial acquisition offers a large potential to reduce scan times by means of polar undersampling. Little aliasing artifacts are expected from the results of the simulations, even without the need for additional a-priori information such as the coil sensitivity profile, which are required for alternative accelerated imaging techniques such as SENSE [prue99] or GRAPPA [gris02]. In conclusion, the practical

degree of undersampling in a 3D radial acquisition is not limited by undersampling artifacts, but predominantly by the available SNR.

2. Improved thin-slab CMRA protocols with cardiac motion correction

2.1 Current state-of-the art and contribution

As previously described in the introduction, a shortcoming of today's coronary magnetic resonance angiography (MRA) is its low scan efficiency, as only small well-defined fractions of the cardiac and respiratory cycle are used for data acquisition. These precautions are necessary to cope with cardiac and respiratory motion.

For illustration, a simplified EKG-triggered coronary MRA protocol is sketched in Fig. 2.1. To avoid motion artifacts, a small temporal window (60-80ms) is used for data acquisition (AQ). A fat suppression prepulse (F) is commonly applied prior to sampling to obtain a fat-suppressed depiction of the coronary vessels. Furthermore, data are acquired with a well-defined offset from the R-wave, which is detected using a vector EKG system [fisch99] with four electrodes attached to the patient's breast. The offset is referred to as the trigger delay, T_D, which is commonly set to values of 500-700ms to acquire data in a phase with minimal cardiac motion in diastole. The adjustment of the trigger delay is usually carried out at the beginning of the examination according to the momentary cardiac frequency of the subject, and kept constant during the image acquisition.
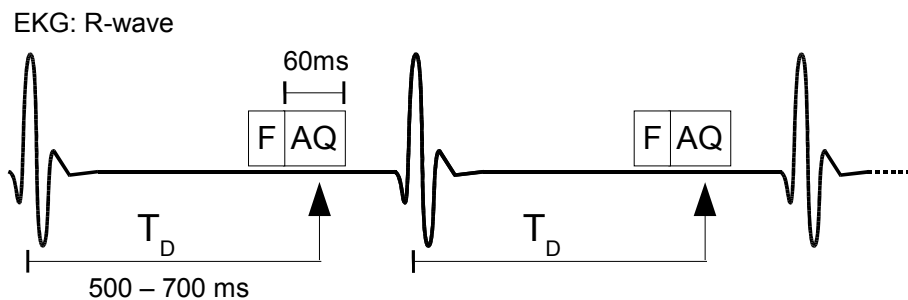
Fig 2.1 EKG-triggered coronary MR protocol. Data are acquired in a short cardiac acquisition window (AQ) only to minimize motion-induced image artifacts. Furthermore, a fixed offset (trigger delay, T_D) is defined from the onset of the cardiac cycle (R-wave) to position the acquisition in late diastole, where motion is expected to be minimal. A fat suppression prepulse (F) is commonly applied prior to data acquisition for a fat-suppressed depiction of the coronary vessels

Given an 80 ms cardiac acquisition window out of an 800ms RR-interval, and a respiratory gating efficiency of 50%, a typical value for the scan efficiency is 5%. While motion artifacts can be suppressed efficiently with these measures, the low scan efficiency results in very long scan times ranging from 5 to 10 minutes for each coronary vessel, which may not be tolerated by patients. To date, various strategies have been developed to improve the scan efficiency,

such as the simultaneous acquisition of two stacks to image the LAD and RCA within one pass [manke01], or accelerated protocols with echo-planar acquisitions [bot99], or patient-specific prospective respiratory motion correction [manke03].

  However, the present studies focus on a novel strategy to increase the scan efficiency, namely an extended cardiac acquisition window. The present approach has a large potential to decrease the scan time when compared to conventional scanning with a short cardiac acquisition window, because significantly more data is acquired in each RR interval. For this purpose, radial scanning techniques were employed, which were shown to exhibit a low sensitivity to motion. This particular result is in good agreement with the findings in the theory section as well as the recent results in the literature [spue04].

  As a further refinement, coronary vessels motion that occurs during the prolonged sampling interval is compensated by means of a novel, image-based retrospective motion correction technique, which corrects for relative motion between k-space subsets prior to the reconstruction of a final, high-resolution image.

  However, some obstacles have to be taken into account when using the present, motion-corrected CMRA protocol with extended cardiac acquisition windows. One difficulty arises from a recovering fat signal during prolonged sampling, which may hamper fat suppression. The problem has been solved by means of an steady state free precession (SSFP) sequence with intrinsic fat/water separation applied to coronary MRA for a fat-suppressed depiction of the coronary vessels, which will be described in more detail in a forthcoming section.

   Finally, inter-RR motion during image acquisition in terms of variations of the RR interval during image acquisition has been reduced considerably by a real-time adaption of the trigger delay in concert with a dynamic arrhythmia rejection technique. Initial *in vivo* results obtained in healthy adult volunteers conclude the second chapter.

2.2 Prospective vs. retrospective motion correction – an overview

The two main motion correction strategies, namely a prospective correction with precompensated gradient waveforms, and retrospective correction using regridding, have been presented in the theory section. However, the purpose of this section is to provide an overview which approach is best suited for cardiac motion correction. Both techniques have specific advantages and shortcomings. With prospective correction, motion effects are already compensated during the acquisition. In principle, an image quality equivalent to that obtained in a static object can be achieved, and no postprocessing is required. However, the corrections are inherently limited to linear (affine) motion models, unless higher order gradient systems are employed. More importantly, the motion model must be entirely known at the time of the acquisition to adapt the sequence properly, and the correction can only be applied globally to the entire object and not only to a certain region of interest. This may introduce additional artifacts from outer regions, which do not move according to the motion model. These artifacts (e.g. ghosting or streaking) induced by the motion correction process can in principle affect the entire image and, therefore, also the region of interest. A brief comparison of the specific benefits and limitations is given in Table 2.1.

Table 2.1 *Benefits and limitations of prospective vs. retrospective motion correction strategies*

Prospective correction	Retrospective correction
⊕ *no overlapping data or data voids in k-space regions*	⊖ *depending on the 3D imaging volume, only small motion amplitudes can be compensated*
⊕ *no post-processing is required*	⊕ *no modification of gradients required at runtime*
⊖ *limited to 3D affine transformations*	⊕ *higher order models (non-rigid) can be applied*
⊖ *correction can only be applied globally, potential artifacts resulting from regions that perform a different motion pattern*	⊖ *potential artifacts resulting from data voids in k-space*
⊖ *object motion state must be known at the time of the data acquisition*	⊕ *motion model can be extracted from image data itself*

The most prominent advantage of retrospective correction that the precise motion pattern does not have to be known at the time of the acquisition. Moreover, the motion parameters can be extracted from the image data itself.

This is an important benefit for motion-corrected coronary MRA, as the instantaneous detection of the motion state as required for prospective motion correction is extremely

difficult. For respiratory motion compensation, this difficulty is addressed by introducing a model instead, which delivers the estimated motion parameters from a few easily accessible motion quantities, such as the respiratory navigator [ehm89]. While approaches exist [foo00] to follow the motion of the coronary arteries throughout the cardiac cycle by means of simple slice following, a reliable and precise prediction of intra-RR coronary vessel motion remains a challenging task.

The EKG signal (R-wave) can indeed be used to determine the onset of the cardiac cycle ([eint1906], [eint1907]), and to synchronize the data acquisition with the beating heart. However, a precise prediction of intra-RR cardiac motion on the bases of the R-wave is currently not possible. Furthermore, to enable prospective correction, a pre-scan with very high spatial resolution were required to detect motion of the small and tortuous coronary arteries. The duration of such a pre-scan could easily reach the order of the actual imaging experiment, and therefore it is impractical for clinical applications. Thus, for intra-RR correction of coronary motion, retrospective correction appears to be the method of choice, as the motion parameters can be extracted directly from the high-resolution data acquired for imaging. Also, higher-order model such as non-rigid or elastic transformation could be employed as a further benefit. However, there is a trade-off between the greater flexibility of retrospective correction, and potential artifacts resulting from undersampled regions of k-space (signal voids, cf. Fig. 1.4). Also, it needs to be ensured that the region of interest does not leave the 3D imaging volume due to motion, otherwise retrospective correction is not possible. However, motion amplitudes in coronary vessel motion were shown to be small enough to be covered by means of retrospective corrections in the present work.

2.3 Radial MR sequences with extended cardiac acquisition windows[1]

2.3.1 Introduction

To overcome the long scan times in today's coronary magnetic resonance angiography (CMRA) it is desirable to extend the cardiac acquisition window, i.e., acquire more data in each RR interval.

With Cartesian, spoiled gradient echo (SPGRE) sequences used to date, the extend of the cardiac acquisition window has been limited by the available steady state magnetization on the one hand, and by cardiac motion on the other hand. To overcome the motion problem, radial scanning techniques are promising candidates, since they exhibit a low sensitivity to motion [glov92] as shown in the theory section. This idea is supported by recent results in cardiac CT, where helical sampling schemes with acquisition windows greater than 150ms yield good image quality.

Furthermore, steady-state free precession (SSFP) sequences are well established tools for cardiac imaging in the meantime [desh01], and allow for arbitrary long sampling intervals with high SNR and without saturation effects. Hence, a combination of SSFP and radial scanning is an interesting tool for coronary MRA, which has been explored in parallel by other groups ([lar02], [spue04]).

Thus, the feasibility of an extended cardiac acquisition window for shortened scan times in conjunction with SSFP sequences and radial scanning is an interesting question that is investigated in this section. First in-vivo experiments obtained in healthy adult volunteers prove the utility of the proposed technique.

2.3.2 Methods

Experiments were performed on seven healthy volunteers (age range 33-47 years, 7M). The examinations were performed on a whole body 1.5T MR system (Gyroscan ACS-NT 15, Philips Medical Systems) equipped with a five-element cardiac synergy receive coil. The image acquisition was EKG-triggered, with a delay set according to the heart rate and acquisition window length [kim01]. To eliminate artifacts introduced by respiratory motion, the measurement was navigator-gated (right hemi-diaphragm), using a gating window of 5mm. A

---

1   Related publication: C. Stehning, P. Börnert, T. Schäffter, O. Dössel. Radial Balanced FFE Imaging with Extended Sampling Windows for Fast Coronary MRA, Proc. ISMRM 10, 732 (2003)

radial stack-of-stars volumetric acquisition scheme as previously shown in the introduction (Fig. 1.8 [c]) was used in combination with a SSFP sequence [opp86] to obtain a fast acquisition with high signal-to-noise ratio ([spue04], [lar02]). The readouts of one readout train comprising 13 readouts were acquired subsequently in the phase encoding direction (k_z, cf. Fig 1.8 [c]). A centric order starting with the low k-space profiles was used to obtain a maximum efficiency of the magnetization preparation pulses.

To vary the acquisition window length, an integer number of N radial projections were sampled for each phase encoding step in k_z-direction, resulting in acquisition window lengths between 61ms (N=1) and 244ms (N=4). The following sequence parameters were used: FOV 360x360mm, slice thickness 1.5mm, 20 slices (overcontiguous), measured voxel size 1.12 x 1.12 x 3.0mm, reconstructed voxel size 0.7 x 0.7 x 1.5mm, TE 2.3ms, TR 4.7ms, flip angle α=60°. Prior to signal sampling, T_2 preparation (50ms), navigator and fat suppression were applied. The order of the different scans was randomized to exclude effects arising from the prolonged imaging session. The RCA and the LAD were located using a three-point planscan utility [stu99]. To evaluate the image quality, the SNR, contrast to noise (CNR) and the visible vessel length were measured. In addition, two reviewers scored the MR angiograms independently. For final presentation, the 3D data sets were reformatted using a software tool [eti02].

2.3.3 Results

In all examined volunteers and for all acquisition window lengths, the major parts of the proximal coronaries (RCA, LAD) were well depicted. The mean visible vessel lengths were 66-135 mm for the RCA and 65-89 mm for the LAD. Selected data sets of the RCA and the LAD are shown in Fig. 2.2.

Sporadic radial streaking artifacts and minor image blurring occurred, but a diagnostic image quality was obtained with all cardiac acquisition window lengths. All anatomical details remained visible in all volunteer examinations at acquisition windows greater than 200ms. Slightly decreased values for the visible vessel length were measured, but no significant decrease of the SNR and CNR was observed. For the left coronary artery (LAD), which was imaged in a volunteer with a high cardiac frequency (80bpm), an apparent decrease in the vessel diameter was observed as well as image blurring that mask small side-branches of the LAD (white arrow, cf. Fig. 2.2 [e]). In all experiments, the scan time was reduced by a large
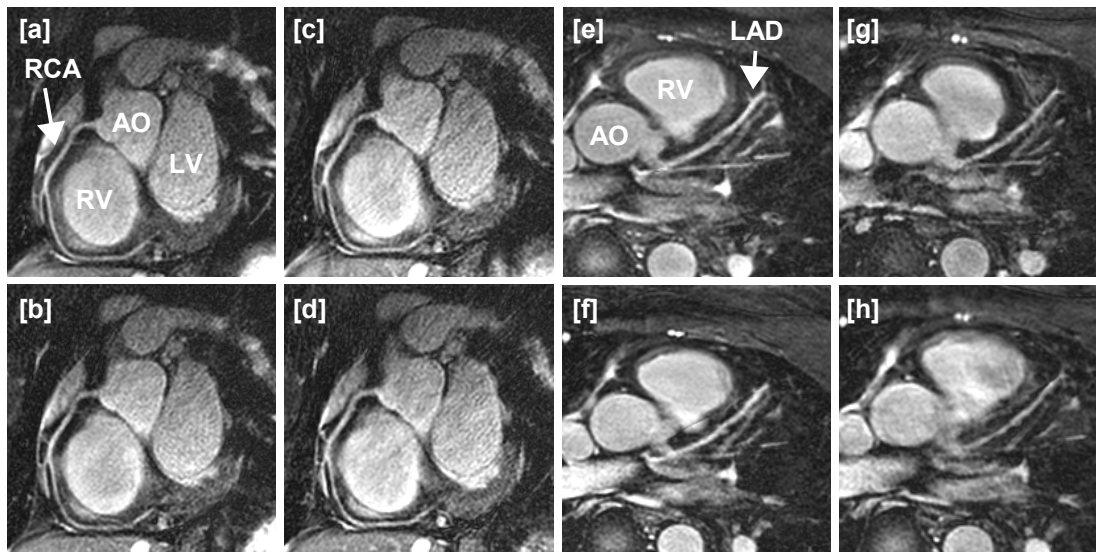
Fig. 2.2 *Reformatted views of the RCA [a-d] and the LAD [e-h] acquired in healthy volunteers using radial scanning and different acquisition window lengths: [a / e] TAQ = 61ms, [b / f] TAQ = 122ms, [c / g] TAQ = 183ms, [d / h] TAQ = 244ms. For the RCA, little motion artifacts are observed even for the longest cardiac acquisition window. For the LAD, which was acquired in a volunteer with a high cardiac frequency (80 bpm), an appearent decrease of the vessel diameter is observed, and small side-branches are blurred as a result of the extended acquisition window*

scale from 10 minutes to approximately 2-3 minutes by means of an extended cardiac acquisition window.

The essential results of the volunteer study have been summarized in Table. 2.1. The scan duration estimate is based on a 50% respiratory gating efficiency. The image quality scale was as follows: 0, poor, the main coronaries were blurred and not well depicted; 1, good, the main coronary arteries were clearly depicted; 2, excellent, the main coronary artery and its branches were clearly depicted. The displayed values for the vessel length, the SNR and CNR are mean values +/- standard deviation.

Table 2.1 *Results for radial SSFP coronary imaging using different acquisition window lengths, T_{AQ}. The visible vessel length, SNR and CNR were measured using a software tool. The image quality was scored by two independent reviewers (medical engineers). The image quality scale was as follows: 0, poor, the main coronaries were blurred and not well depicted; 1, good, the main coronary arteries were clearly depicted; 2, excellent, the main coronary artery and its branches were clearly depicted*

TAQ [ms]	scan duration [min]	vessel length [%]	SNR	CNR	scored image quality (0-2)
61	09:54	100 ± 0	203 ± 61	128 ± 37	1,8
122	04:36	93 ± 11	206 ± 58	133 ± 33	1,5
183	03:04	88 ± 16	181 ± 67	117 ± 36	1,4
244	02:28	84 ± 14	187 ± 54	111 ± 26	1,2

2.3.4 Discussion and conclusion

A major shortcoming of high resolution coronary MRA, namely a low scan efficiency and prolonged scan time, has been addressed in this study. We have shown that extended acquisition windows comparable with spiral CT are feasible using SSFP sequences in concert with radial scanning techniques, which have proved to be a very robust tool for cardiac studies. The scan time was reduced from ten to less than three minutes, while similar image quality was obtained in most volunteers when compared to conventional protocols using short cardiac acquisition windows. However, motion artifacts in terms of blurring that masks coronary side branches was observed in one volunteer with a high cardiac frequency. Thus, the presented radial scanning technique is a promising candidate for coronary MRI due to its low sensitivity to motion to start with, but the integration of motion correction during an extended sampling window is an interesting approach to further improve the image quality, which will be addressed in a forthcoming section.

2.4 Continuous epicardial fat suppression[2]

2.4.1 Introduction

The coronary arteries are surrounded by an epicardial fat layer for protection (Fig. 2.3). Especially in MR images obtained with SSFP sequences, fat and blood exhibit similar signal intensities, or gray levels, respectively, which may impair contrast. Hence, in coronary MRA, contrast preparation such as the suppression of epicardial fat is an essential step to improve the depiction of the coronary vessels. For this purpose, spectrally selective saturation prepulses [ros84] are applied prior to signal sampling (cf. Fig. 2.1).
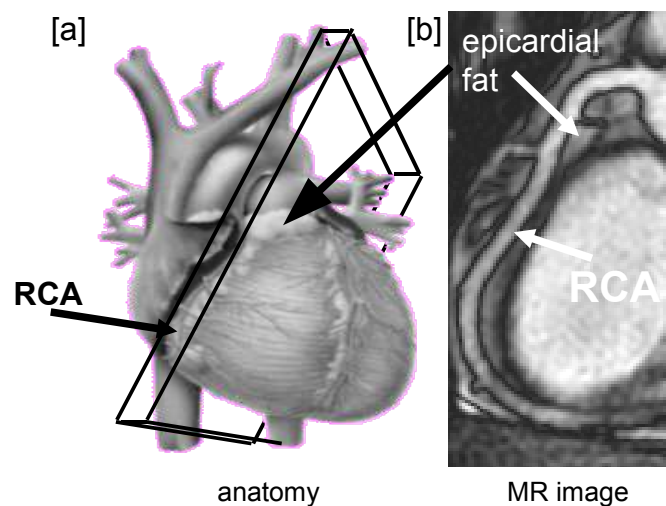

Fig. 2.3 The coronary arteries are surrounded by an epicardial fat layer for protection (dotted arrow, [a]). A double-oblique slice that was used to image the RCA is drawn in black. In MR images obtained with SSFP sequences ([b], fat and blood exhibit similar signal intensities, or gray levels, respectively, which may impair contrast. Thus, the suppression of lipid signal is desirable

However, if extended acquisition windows as described in the previous section are used, fat suppression is a challenging task due to the T_1 relaxation of the lipid signal over the prolonged cardiac acquisition window, as shown in Fig. 2.4. Furthermore, image artifacts may result from the transient fat signal recovery during sampling ([cra88], [har01]).

---

2 Related publication: C. Stehning, P. Börnert, K. Nehrke, O. Dössel. Continuous Epicardial Fat Suppression for Coronary MRA using Balanced FFE with Long Cardiac Acquisition Windows – A Comparison of Two Techniques, Proc. ISMRM 12, 702 (2004)
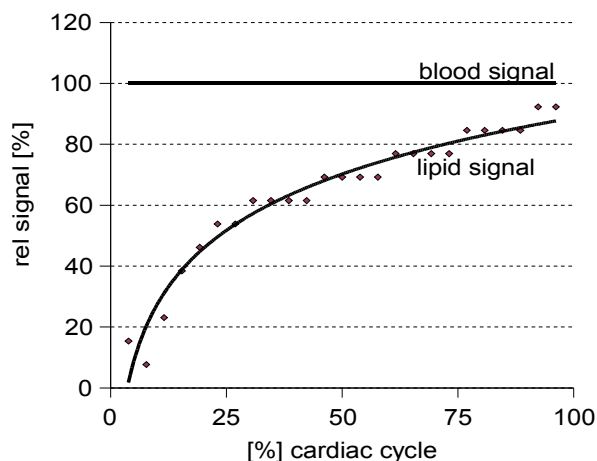
Fig 2.4 *Measured relative signal intensity of lipid (anterior chest wall fat and epicardial fat) compared to blood signal after one initial spectrally selective fat suppression prepulse applied at the onset of the cardiac cycle. The dynamic recovery of the fat signal follows an exponential T1 relaxation (T1=250ms at 1.5T)*

As an alternative to fat suppression prepulses, a variety of fat-suppressed imaging techniques exist, most of which are based on a multiple acquisition of the image, for instance two- or three-point Dixon methods [dix84]. However, a repeated image acquisition is prohibitive in coronary MRA due to the long scan times. Hence, two approaches that allow for fat-suppressed imaging without significant increase in scan time are investigated in this study. A straightforward approach [sche01] is the integration of multiple fat suppression pulses into the acquisition (cf. Fig. 2.5 [b]). Alternatively, in SSFP imaging, voxels with lipid signal can be detected and eliminated retrospectively by phase discrimination (Fig. 2.5 [c]).

In this section, both techniques are evaluated in phantom- and in vivo experiments, and the achieved fat suppression and image quality were compared in a qualitative manner.
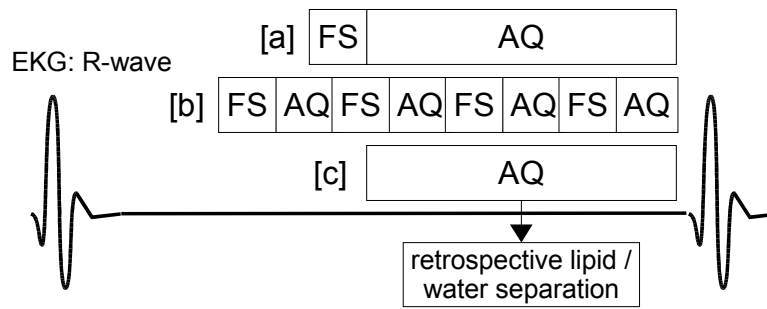
Fig 2.5 Comparison of different fat-suppressed MR sequences. A conventional protocol [a] comprises a single fat suppression prepulse prior to imaging. In the modified protocol shown in [b], multiple fat saturation pulses (FS) are interwoven with the acquisition. In phase sensitive SSFP imaging [c], a fat/water separation is performed retrospectively during image reconstruction

2.4.2 Methods

The acquisition of fat-suppressed images, for instance in coronary MRA, is usually based on selective saturation of lipids followed by the actual imaging experiment [ros84]. A narrow-band RF pulse (flip angle ~110°) that selectively excites the lipid protons, which have a chemically shifted resonance frequency about 3.4 ppm below that of water protons (220Hz @ 1.5T), is followed by a gradient spoiler to dephase the lipid signal in the transverse plane. During the zero-crossing of the remaining longitudinal magnetization in $-M_z$ direction, the k-space center is sampled for optimized fat suppression. This technique is referred to as selective presaturation by inversion recovery, SPIR. Hence, a straightforward approach to provide fat suppression during prolonged sampling is the integration of multiple SPIR pulses into the acquisition. An example employing an SSFP sequence is shown in Fig. 2.6. The steady state is interrupted using a $T_R/2$ $\alpha/2$ tip-up pulse followed by a gradient spoiler that dephases residual transverse magnetization. Next, a SPIR pulse is applied to saturate lipid protons. Finally, the steady-state is resumed with a $-\alpha/2$ $T_R/2$ tip-down pulse. This procedure is repeated periodically during the acquisition.

An alternative approach is a phase-sensitive SSFP technique [har03] that provides separate fat- and water images without additional complexity or scan time increase in a standard SSFP sequence. In SSFP, the phase of the refocused spins alternates for each resonant frequency interval equal to the reciprocal of the sequence repetition time (T_R). An appropriate selection of
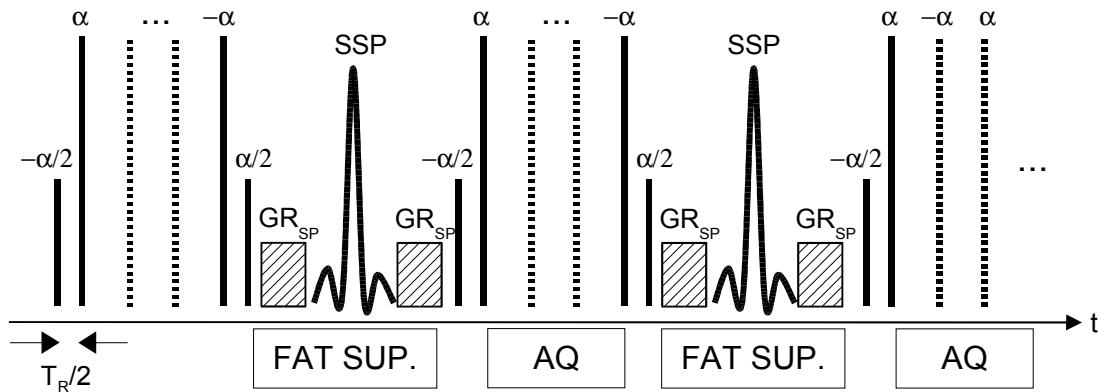
Fig 2.6 *Fat-suppressed MR sequence. Multiple fat saturation pulses are applied during sampling. The steady-state magnetization is stored in longitudinal orientiation using a TR/2 a/2 tip-up pulse followed by a gradient spoiler (GRSP) to dephase residual transversal magnetization. Next, a spectrally selective pulse (SSP) tips the lipid magnetization into the transversal plane and dephases the lipid signal with a second gradient spoiler. The steady-state imaging sequence is then resumed using a -a/2 TR/2 tipdown pulse*

the T_R results in a 180° phase difference between lipid and water signals, as shown in Fig. 2.7. This phase difference can be used for lipid/water separation by means of a phase discrimination.
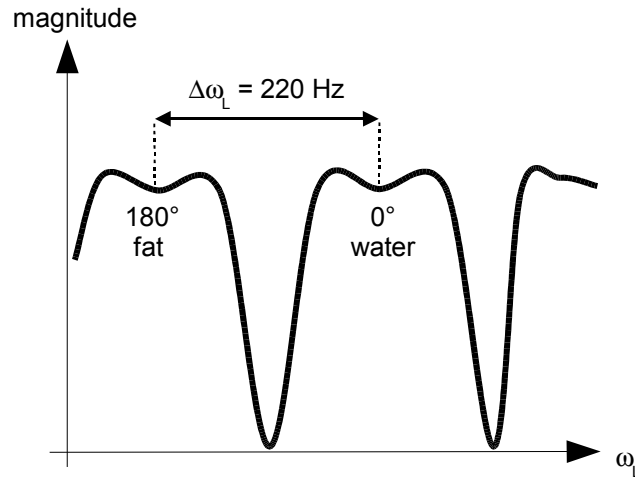
Fig 2.7 *Frequency response in SSFP imaging: given an appropriate TR equal to the inverse of the chemical frequency shift between water and lipid resonance (220Hz -> TR = 4.6ms), water and lipids fall into adjacent passbands, but have opposite signal phase. Hence, the complex data can be reconstructed into separate fat- and water images by a simple phase discrimination*

For a comparison of both techniques, a spherical phantom which was filled with water and vegetable oil as shown in Fig. 2.8 [a] was used.

In vivo experiments using both techniques were performed on seven healthy volunteers (age range 27-47 years, 7M). The examinations were performed on a whole body 1.5T MR system (Gyroscan INTERA, Philips Medical Systems) equipped with a five-element cardiac synergy receive coil. The image acquisition was EKG-triggered with a heart-rate specific trigger delay T_D [kim01] and respiratory-gated [ehm89] with a 2D-selective navigator placed on the right hemi-diaphragm (gating window 5mm). A regional saturation (REST) pulse was applied to suppress signal from the anterior chest wall. The respiratory navigator and REST-slab were applied prior to sampling. An SSFP sequence combined with radial stack-of-stars sampling as previously shown in Fig. 1.8 [c] was used in both fat suppression techniques. The following sequence parameters were used: α=60°, TR=4.4ms, FOV 330x330x30mm³, measured voxel size 1.12 x 1.12 x 3.00mm³, reconstructed voxel size 0.7 x 0.7 x 1.5mm³. For the retrospective fat elimination method, a slightly increased T_R = 4.6ms was used to obtain an opposite phase between water and off-resonant fat voxels [har03]. Prior to phase discrimination, a basic phase correction was performed separately for each reconstructed slice. The mean absolute phase of all voxels in one slice was calculated and corrected. Next, the complex data was reconstructed into separate fat- and water images by a discrimination of the phase sign.

To visualize the epicardial fat signal recovery, or the performance of the continuous fat suppression technique, respectively, an extended cardiac sampling window (T_{AQ}=240ms) was subdivided into 4 temporal segments (segment length T_{SEG}= 60ms). The segments were reconstructed separately as a time series. For comparison, a conventional imaging protocol with identical scan parameters, but with only one initial fat saturation pulse at the onset of the cardiac sampling window was acquired. For final presentation, the 3D data sets were reformatted using a software tool [eti02].

2.4.3 Results

The result of the phantom experiment is shown in Fig. 2.8. The phase sensitive SSFP sequence provided a reliable separation of lipid and water voxels. However, partial volume effects in terms of signal cancellation occurred at the oil/water interface (cf. Fig. 2.8 [b]). As a consequence thereof, an apparent decrease in the water level in the phantom was observed (cf. Fig 2.8 [c]) when compared to a fat-suppressed image obtained with a conventional fat suppression prepulse.
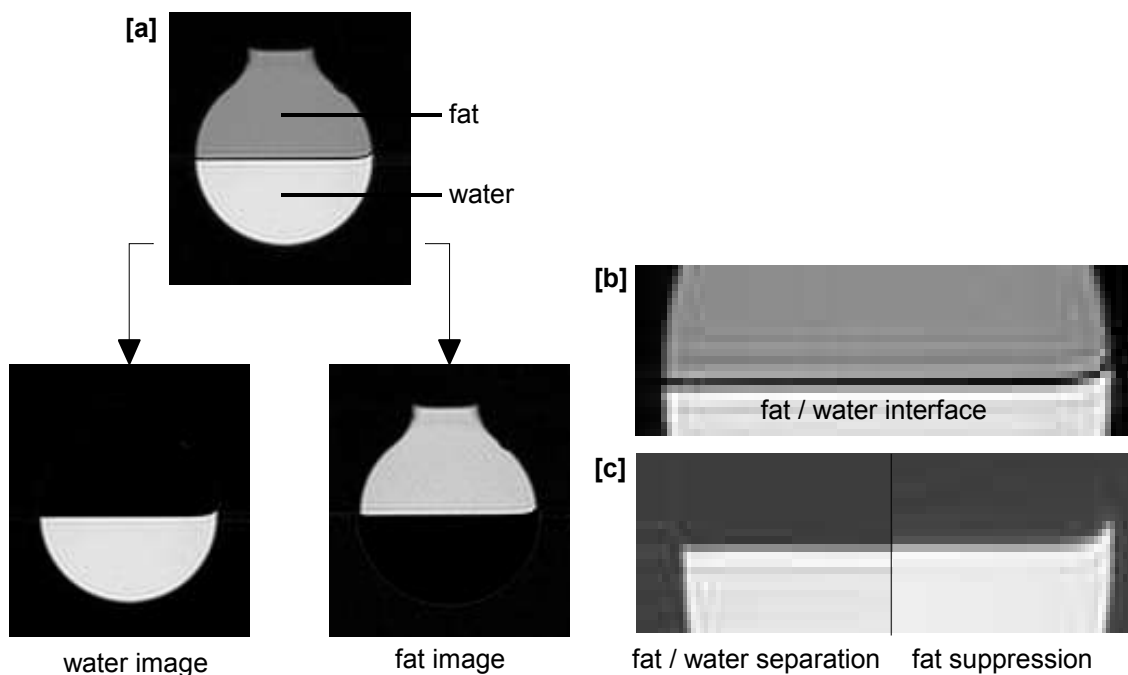
Fig 2.8 *Phantom experiment. A spherical phantom filled with water and vegetable oil is reconstructed into separate water- and fat images by means of a phase-sensitive SSFP acquisition [a]. However, partial volume effects (signal cancellation) occur at the oil / water interface [b]. If a fat-suppressed image obtained with a conventional lipid saturation prepulse is compared with an image obtained with the phase-sensitive SSFP, an appearent difference in the water level is observed ([c], left and right)*

An exemplary image of the RCA for a late temporal segment (~200ms delay to preparation) obtained in a volunteer is shown in Fig. 2.9. In Fig. 2.9 [a], a conventional protocol comprising one SPIR pulse during preparation was used. A strong signal from epicardial fat is visible due to fat relaxation.

In Fig. 2.9 [b], inter-segment SPIR pulses were applied, resulting in a significantly improved fat suppression when compared to a conventional protocol using one prepulse at the beginning of the acquisition. However, artifacts related to the interruption of the steady state resulted in inhomogeneous depictions of the blood pool as well as a pronounced image blur (dotted arrows), especially at the outer bounds of the FOV. The retrospective fat elimination, Fig. 2.9 [c], yielded a superior fat suppression in all volunteers, making additional fat suppression pulses superfluous. Furthermore, artifacts as a consequence of interruptions of the steady state
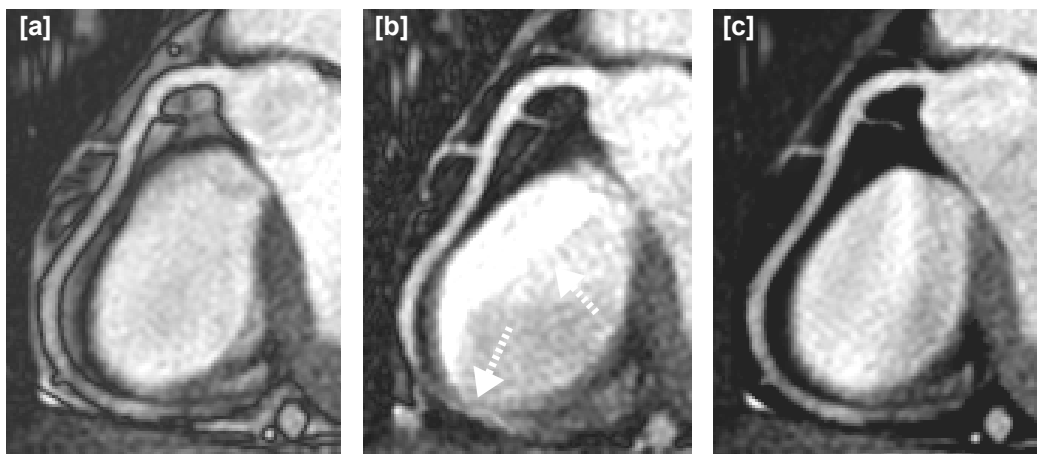
Fig 2.9 Reformatted RCA images obtained in a healthy volunteer using different fat suppression strategies. In [a], a conventional protocol comprising a single fat suppression prepulse prior to sampling was used. A strong signal from the epicardial fat is observed resulting from the fast T_1 relaxation of fat. In [b], multiple fat suppression pulses were interwoven with the acquisition. In [c], a phase-sensitive SSFP sequence was used, and fat voxels were eliminated retrospectively by means of phase discrimination. A slightly decreased image quality in terms of an inhomogeneous depiction of the blood pool in the RV and blurring that obscured distal parts of the RCA was observed in [b] (dotted arrows)

were nonexistent, as the steady state was maintained during the cardiac acquisition window. However, an apparent vessel diameter decrease was observed when compared to an angiogram obtained with conventional fat suppression prepulses, with can be well explained with the partial volume effect already observed in the phantom study.

2.4.4 Discussion and conclusion

Prolonged cardiac acquisition windows, e.g. for increased scan efficiency in coronary MRA, require continuous fat suppression. An acceptable suppression of epicardial fat over a prolonged sampling period was achieved with both methods under investigation, without increasing the scan time significantly. However, the straightforward approach, comprising multiple SPIR pulses during sampling, is currently limited by image quality losses resulting from the interruptions of the steady state. This drawback could be overcome by more robust startup/rundown cycles ([fox03], [har01]) as a future refinement. However, these starter sequences are lengthy when compared to the simple $\alpha/2$ tipdown/tipup pulse employed in this study. As a consequence thereof, the scan efficiency is reduced, since no data can be acquired during starter sequences and fat saturation. Opposed to that, the retrospective removal of fat voxels from the complex images were proved to be a reliable tool for efficient epicardial fat suppression in coronary MRA, and does not reduce the scan efficiency at all. However, an apparent narrowing of the coronary arteries occurred as a result of partial volume effects. Since the spatial extent of these effects is limited to the size of a voxel, a high spatial resolution is required to overcome this drawback. As an estimate, the voxel size must be smaller than the vessel wall diameter (~0.7mm) to avoid an apparent decrease of the vessel lumen. However, high resolution imaging is a prerequisite of coronary MRA anyway, which countervails the potential partial volume effects observed with the complex SSFP sequence.

## 2.5 Coronary MRA with intra-RR motion correction[3]

2.5.1 Introduction

As previously described, MR sequences with extended cardiac acquisition windows in concert with radial scanning allow to reduce scan times in coronary MRA. However, cardiac motion that occurs during prolonged sampling may still hamper image quality, as it was observed *in vivo* in one volunteer with a high heart rate in Fig. 2.2. To overcome this restriction, a radial stack-of-stars SSFP sequence with intra-RR motion correction is investigated in this section. Multiple independent k-space segments (Fig. 2.10) are acquired in an extended sampling window in each RR interval, and inter-segment motion is detected using a self-guided, epicardial fat tracking procedure, and corrected in a post-processing step. Finally, combining data from all motion-corrected segments forms a high-resolution image. Experiments on healthy volunteers are presented to show the basic feasibility of this approach. Since more data is acquired in each RR-interval, scan efficiency is increased considerably, while image quality was maintained, or even improved, when compared to conventional protocols with a short cardiac acquisition window.

2.5.2 Methods

Experiments were performed on seven healthy male volunteers (age range 30-36 years). The examinations were conducted on a whole body 1.5T MR system (INTERA, Philips Medical Systems) equipped with a five-element cardiac phased array coil. The sequence is described in more detail in the following sections.

MR sequence - The image acquisition was performed during free breathing using respiratory gating [ehm89] and slice tracking [dan97] with a pencil-beam navigator placed on the right hemi-diaphragm (gating window 5mm). The acquisition was EKG-triggered with a heart rate dependent trigger delay [kim01]. Respiratory navigator and regional saturation (REST) slab were applied prior to sampling [stu99]. A steady state free precession (SSFP) sequence with balanced gradient integrals was employed. It provides high SNR and T2-like contrast [lar02] without the need for additional T2-preparation prepulses, and does not entail magnetization saturation effects over an extended cardiac sampling window [gio02]. The following sequence

---

3   Related publication: C. Stehning, P. Börnert, K. Nehrke, O. Dössel. Free breathing 3D balanced FFE coronary MRA with prolonged cardiac acquisition windows and intra-RR motion correction, Magn Reson Med 2005, 53:719-23
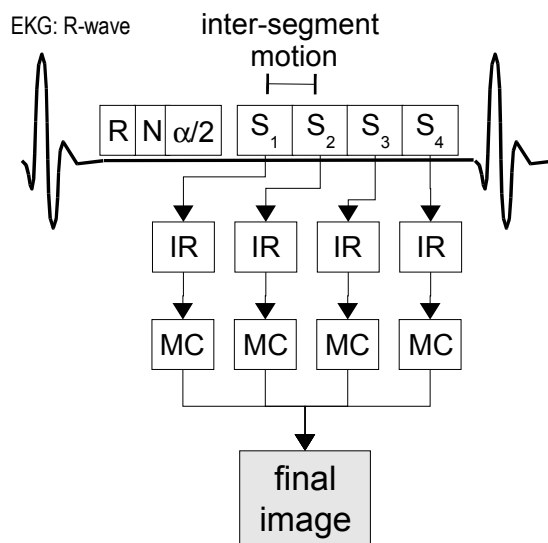
Fig. 2.10 *Scheme for intra-RR motion corrected coronary MRA with independent acquisition of multiple k-space segments (S_1-S_4). N denotes the respiratory navigator, R the regional signal saturation and an $\alpha/2$ tip-down pulse, respectively. The segment length is kept sufficiently short to reduce intra-segment motion. To cope with inter-segment motion, motion correction (MC) is performed separately for each segment after image reconstruction (IR). Finally, the combination of data from all segments forms the final image*

parameters were used: flip angle α = 60°; T_R = 4.6ms; FOV 330x330x30mm³; measured voxel size 1.12 x 1.12 x 3.00mm³; reconstructed voxel size 0.7 x 0.7 x 1.5mm³; cardiac acquisition window T_{AQ}=240ms. To cope with cardiac motion during the prolonged sampling interval, the acquisition was subdivided into segments (S_1..S_4, cf. Fig 2.10), which were kept sufficiently short (T_S = 60ms) to reduce intra-segment motion.

Compared with a conventional protocol with acquisition windows of typically 60ms or less, four times as many data were acquired in each cardiac cycle. In principle, this allows for a scan time reduction by a factor of four. In this work, however, the scan time was halved and oversampling (factor of two) was employed to increase the SNR at the same time, to achieve a reasonable trade-off between the two parameters. The data were acquired over roughly 150 RR-intervals using radial 3D stack-of-stars sampling as previously shown in Fig. 1.8 [c]. Each segment was angularly undersampled (50% sampling density compared to a fully sampled Cartesian acquisition). However, the undersampled segments (Fig. 2.11, [a]-[c]) were interleaved in a way that a fully sampled data set is obtained from a combination of the k-space segments (Fig. 2.11 [d]) to avoid aliasing artifacts in the final image.
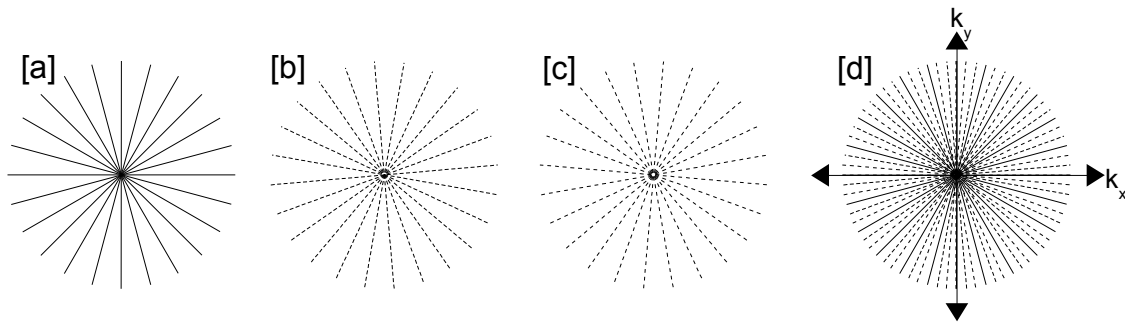
Fig. 2.11 *Radial acquisition scheme comprising multiple angularly undersampled k-space segments ([a]-[c]). A fully sampled data set is obtained from the combination of all segments [d]*

Due to the low sensitivity to undersampling in a radial acquisition [lar02], intermediate images used for motion detection could be reconstructed from undersampled data (cf. Fig. 2.11 [a] – [c]) with little aliasing artifacts. A "smooth" triangular-shaped phase encoding order (e.g. profile number order 1, 3, 5, 6, 4, 2, 0, -2, -4, -6, -5, -3, -1 for 13 phase encoding steps in the k_z-direction) was applied to ensure small gradient transitions between successive readouts, and between subsequent segments, and thus reduce eddy current related disturbance of the steady state [sche03]. For comparison, a conventional protocol using equivalent parameters, but a short acquisition window (T_{AQ}= 60ms), a spectrally selective fat suppression prepulse, and no angular undersampling was performed in two volunteers. An additional pre-scan (~1 min) to measure the coil sensitivity maps was performed to facilitate an optimal combination [roem90] of the complex data acquired with the multi-element receive coil.

Motion detection - while approaches are known to detect motion directly in k-space [lark04], the motion model, i.e., the coefficients of an affine transformation that describes the relative object deformation between the segments, were determined in the image domain. To detect motion exclusively for the coronary vessels, in principle, geometric-driven approaches, such as the definition of landmarks on the coronary vessels, were necessary. However, the registration accuracy then depends on the feature detection precision, and subjectivity is introduced if features are manually or semi-automatically detected. In addition, this procedure is very time consuming and therefor impractical for clinical practice.

Hence, for the present approach, a novel approach for the detection of motion based on an automated pre-segmentation of the coronary vessels was employed. This procedure will be

referred to as epicardial fat tracking (EFT) and is described in the following. It was assumed that the motion of the coronary arteries is identical to the motion of the epicardial fat that surrounds them. This assumption is supported by a recent study [ngu03], where respiration-induced coronary motion was measured by means of epicardial fat navigator echoes.

Hence, a fat-only image obtained with the previously described fat/water separation technique that shows a „footprint" of the imbedded coronary artery was used for a pre-segmentation of the coronary vessel structure. A simple 3D mask as shown in Fig. 2.12, was sufficient to exclude signal from other fat structures, such as the chest wall (cf. Fig 2.12 [c]). In the present work, this mask was positioned manually. However, an automated masking could be achieved as a further refinement, for instance by using the pre-defined shim volume that is placed across the heart prior to image acquisition.
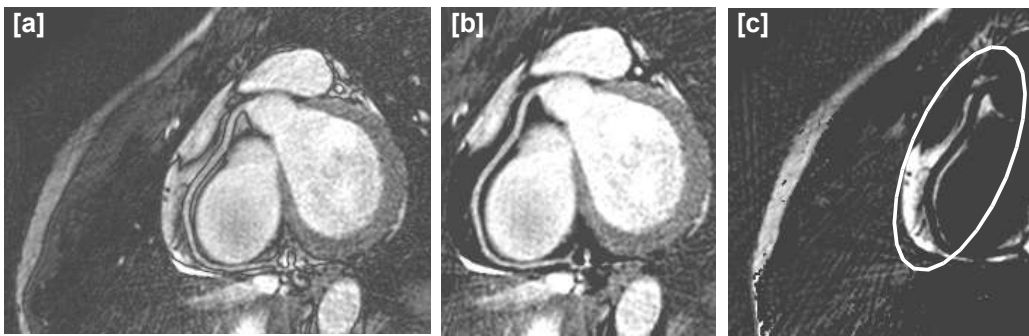
Fig. 2.12 *Images of the RCA reconstructed from one angularly undersampled k-space segment obtained with a phase-sensitive SSFP sequence. In [a], the magnitude representation is shown. In [b], the water-only image of RCA is shown. In [c], the fat-only image is shown, where the outline of the RCA can be segmented with a simple elliptical mask. Assumed that the imbedded coronary vessel performs identical cardiac motion as the surrounding epicardial fat, the measurement of RCA displacement and deformation during the cardiac cycle can easily be performed using the epicardial fat images*

The vessel "footprints" were used to track coronary vessel motion and deformation through the cardiac cycle with respect to a reference (i.e., the first acquired segment in the RR-cycle) using a freely available image registration tool [hartk02] without further user interaction.

To optimize image alignment, the normalized mutual information (NMI) based on joint entropy H(t,s), or „information" in the joint image was used as a similarity measure:

$$NMI = \frac{H(t) + H(s)}{H(t,s)}$$

[2.1]

with

$$H(t) = -\sum_a p(a) \log p(a)$$
$$H(s) = -\sum_b p(b) \log p(b) \qquad [2.2]$$
$$H(t,s) = -\sum_a \sum_b p(a,b) \log p(a,b)$$

where p(a) is the probability distribution (i.e., the gray level) in the target image, p(b) is the distribution of the source image, and p(a,b) is the joint distribution of the source- and target images. With the NMI approach, it is assumed that the statistical dependence of the voxel intensities is maximal, or the „information" contained in between the images is minimal, when the images are geometrically aligned. This approach is more robust [stud99] if the two images to be matched only partly overlap, when compared to e.g the cross-correlation, which requires that the object of interest is entirely in the field of view in both images. The motion registration procedure is shown in Fig 2.13 for further illustration.
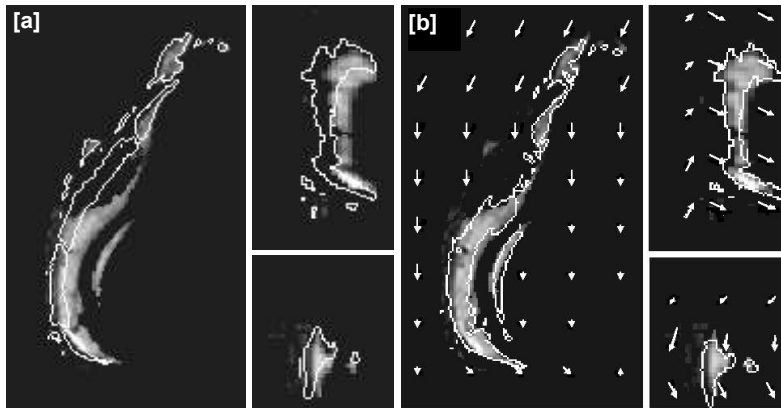
Fig. 2.13 *Illustration of epicardial fat tracking process. Three orthogonal views of the epicardial fat-only image are shown. The reference is shown in grey, while the contour of the epicardial fat at a later time in the cardiac cycle is shown in white in [a]. After registration, the resulting affine transformation forms a displacement field (white arrows), which is used for image based motion correction. A good agreement between reference and the motion-corrected segment is evident in [b]*

Three orthogonal views of the epicardial fat with the RCA "footprint" are shown as gray level images, while the contour of the fat structure acquired in time-shifted segment in the cardiac

cycle is shown as a white outline. The inter-segment translation and deformation detected by means of image registration yields a vector field, which is displayed as white arrows. For motion correction, a 3D affine transformation was used. While a quantitative analysis of the precision of the corrections has not been performed, a good agreement between the reference and the time-shifted segment after motion-correction is obvious in Fig. 2.13 [b].

Since the motion detection- and correction are performed in the image domain, in principle, higher order transformations such as an elastic or non-rigid transformation could be employed to match the data acquired in the subsequent segments. However, non-rigid registration and transformation algorithms require considerable computation times. Furthermore, recent results have shown that an affine model can cover cardiac motion during approx. 50% of the cardiac cycle [rib04]. Hence, in this work, the affine transformation was considered sufficient to keep the computational burden within certain limits. However, more complex (non-rigid) motion models could be employed as a future refinement without loss of generality.

Motion-corrected image reconstruction - the data from each radially sampled k-space segment were reconstructed individually using a regridding routine [sul85]. After all segments were motion corrected, i.e., matched onto the reference, the fat-suppressed, water-only images were combined to a final, high-resolution image using a sum of squares approach. The present procedure is very similar to a prior approach [schae99], while motion detection is performed exclusively for the coronary vessel using EFT, and does not rely on a block matching algorithm based on the entire images as in the previous approach.

For final presentation, the coronary vessels were reformatted using a software tool [eti02]. For two volunteers, the images were compared to the conventional protocol as described in the MR sequence section. Signal-to-noise ratio (SNR), contrast-to-noise ratio (CNR) and visible vessel length were compared quantitatively, while image quality and fat suppression were judged by two independent reviewers.

2.5.3 Results

All examinations were completed successfully and the proximal parts of the coronary vessel under investigation (RCA) could be visualized in all volunteers. A reliable fat suppression by means of fat/water separation was achieved in all examinations using the previously described phase detection technique.

Selected reformatted images of the RCA, which were acquired in a reduced scan time by means of extended cardiac acquisition windows (T_{AQ} = 240ms) and intra-RR motion correction are shown in Fig. 2.14 [c] and [d], respectively.
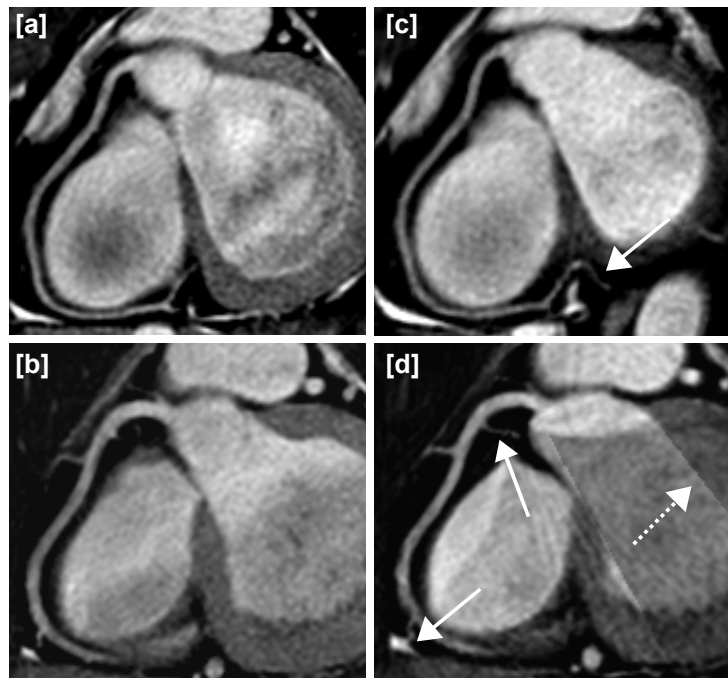
Fig. 2.14 Reformatted images of the RCA obtained with a conventional protocol (a,b), and with the novel sequence comprising high scan efficiency and intra-RR motion correction (c,d). Higher SNR and CNR are evident in the motion-corrected images. Also, more details such as small distal branches could be reconstructed using motion-corrected scanning (solid arrows). Some artifacts resulting from the retrospective correction may occur, as regions may comprise image data from a subset of the acquired segments only (dashed arrow). However, these effects do not occur within the region of interest, such as the coronary vessel

For comparison, reference images obtained using a conventional protocol with a short cardiac acquisition window of TAQ = 60ms were acquired in two volunteers (Fig. 2.14 [a] and [b]). The essential results of a comparison of both techniques are summarized in Table 2.2.

A clear depiction of the coronary vessels was achieved with both protocols, while SNR, CNR and fat suppression were improved using the motion-corrected scan protocol. An at least equivalent image quality was obtained with the motion-corrected CMRA sequence, while the scan time was halved. Furthermore, small distal branches, which could not be reconstructed from data acquired with a conventional protocol, could be visualized (solid arrows).

Table 2.2 *Comparison of a conventional protocol and motion-corrected scanning. Scan time, SNR, CNR, visible vessel length (VVL), number of secondary vessels seen, the achieved fat suppression and scored image quality are given as mean values over two volunteers. The image quality scale was as follows: 0 = poor, the main coronaries were blurred and not well depicted; 1 = good, the main coronary arteries were clearly depicted; 2 = excellent, the main coronary artery and its branches were clearly depicted. The fat suppression scale was as follows: 0 = no fat suppression, 1 = some fat suppression, 2 = sufficient fat suppression, 3 = perfect fat suppression*

	conventional protocol	motion-corrected scanning
sampling density	1	200% (4 segm x 50%)
AQ window	60 ms	240 ms (4 segm x 60 ms)
scan time	~8 min	~4 min
SNR	1	1,26
CNR	1	1,08
VVL	121 mm	120 mm
#sec vess.	2.5	3
image quality	2	2
fat supp.	2	3

2.5.4 Discussion and conclusion

The self-guided, image-based motion correction technique based on epicardial fat tracking (EFT) was found to be robust and to provide specific motion information for the coronary vessel under investigation. Also, potential obstacles such as flow artifacts or intensity modulations did not affect the EFT registration. A self-guided, three-dimensional motion correction of the volumetric thin-slab data based on the epicardial fat structure in undersampled subimages was found to be feasible in all volunteers. Since motion detection and correction are performed entirely in image space, the corrections are not limited to affine models as in prospective motion correction approaches [manke03].

Furthermore, the lipid/water separation that is associated with EFT provides a reliable fat suppression, which is essential for a good depiction of the coronary arteries. However, partial volume effects may occur, which, in the worst case, result in signal voids over one entire voxel. This may lead to an apparent decrease in vessel diameter. Therefore, a high spatial resolution that approaches the vessel wall diameter (0.7-1.4mm) is mandatory.

The motion-corrected MRI sequence provides considerably improved scan efficiency for coronary MRA, as a larger fraction of the cardiac cycle is used for data acquisition. The

increased scan efficiency can be utilized to reduce the scan time, or to increase the SNR, or to choose a trade-off between both parameters. In this work, a fourfold scan efficiency resulted in a halved scan time along with an SNR increased by approximately 26%. This is below the theoretical value of $\sqrt{2}$, however, the deviations between the expected and measured SNR increase are due to current limitations of the reconstruction process, which converts images into unsigned magnitude data. Also, the applied motion correction may be imperfect for some image regions, which means that undersampling artifacts do not cancel out entirely. Nevertheless, more details of the coronary vessels, such as small distal branches, could be depicted in the motion-corrected data set as a result of the improved SNR.

However, some image artifacts (diagonal bends, dashed arrow) related to retrospective motion correction occurred in one volunteer, which is shown for illustration in Fig. 2.14 [d]. The volumetric image data slabs may not perfectly overlap anymore after retrospective motion correction. Instead, some regions may comprise image data from a subset of the acquired segments only. This results in a regionally lower signal intensity and SNR. However, these effects do not occur in the region of interest, for which motion is measured, such as the coronary vessels.

In conclusion, the feasibility of a cardiac motion-corrected sequence with increased scan efficiency has been shown. A superior fat suppression was achieved, and SNR/CNR were improved, while the scan time was reduced for more patient comfort.

In this work, we have confined the study to an extended sampling window in late diastole. Employing the proposed motion correction technique over an even wider acquisition window could be an interesting further refinement. Recently, encouraging results have shown that an affine model can cover cardiac motion during 50% of the cardiac cycle [rib04].

Also, we have confined this study to the right coronary artery, which is subject to most excessive motion. More data is required for the left coronary artery (LAD), and further experiments in patients in a clinical environment are necessary to prove the clinical feasibility of the proposed sequence.

2.6 Inter-RR motion correction for CMRA

2.6.1 Introduction

Despite increasing acquisition speed in coronary magnetic resonance angiography (CMRA), high resolution scans still need to be acquired over several cardiac cycles. Therefore it is crucial to ensure that the respective data segments are acquired in identical cardiac phases, e.g. the late diastolic rest period. Therefore, the acquisition is electrocardiographically (EKG-) triggered, and data is acquired in a fixed, well-defined offset from the R-wave as previously shown in Fig. 2.1. However, heart rate fluctuations may entail a temporal shift of the targeted heart phases within the cardiac cycle. To avoid a mix of cardiac phases in the acquired MR data, resulting in image blur and motion artifacts, arrhythmia rejection can be applied, i.e., data are rejected if the RR-interval is out of fixed predefined limits. Advanced approaches [bot04] also reject data of the preceding RR interval in the presence of arrhythmia, to optimize image quality at the expense of a slightly increased scan time, however.

However, a shortcoming that prevalent arrhythmia rejection techniques with fixed, predefined RR interval windows have in common is the difficulty to cope with slow drifts or permanent deviations between the pre-assumed and actual heart rate. These may occur especially in long coronary scans due to various factors such as emotional stress or relaxation of the patient. Persistent deviations between the assumed and the actual heart rate would result in a rejection of all acquired data, and the scan had to be re-acquired with different settings, or arrhythmia rejection needs to be disabled completely.

To overcome this drawback, a dynamic technique is proposed. To cope with slow drifts and long-term heart rate variations, the cardiac trigger delay is constantly adapted to ensure that data is always acquired in identical cardiac phases. To cope with fast fluctuations of the heart rate (arrhythmia), data are rejected if two successive RR-intervals show a marked relative difference in duration (cf. Fig. 2.15). This allows for a suppression of artifacts related to cardiac arrhythmia and inter-RR variabilities of the cardiac cycle, with no significant increase in scan time.

2.6.2 Methods

To achieve a continuous adaption of the acquisition to the current heart rate, the actual RR-interval duration is continuously monitored using the data obtained from the vector-EKG [fisch99]. A prediction of the upcoming RR interval is based on the measured duration of the

current RR-interval, which is a simple but most reliable method [hay71]. While alternative approaches [bue04] also take additional information obtained from respiratory navigators into account to cope with respiratory sinus arrhythmia (RSA) [bai20], the present approach predominantly focuses on slow drifts of the heart rate during prolonged scanning. An empirical formula, which provides an estimate of the optimal, heart-rate specific trigger delay, was used to place the acquisition into a period with minimal coronary motion:

$$T_{D,n} = 0.47\, T^2_{RR,(n-1)} + 0.35\, T_{RR,(n-1)} + 0.631 - T_{AQ} \qquad [2.3]$$

In Eq. 2.3, $T_{D,n}$ denotes the current trigger delay, which is a function of the measured RR-interval duration $T_{RR,(n-1)}$ of the preceding cardiac cycle, and the acquisition window duration, T_{AQ}. This approach has previously been proposed [kim01] to calculate an optimal, patient-specific trigger delay at the beginning of the image acquisition to cope with inter-patient variability of the cardiac cycle. As an extension, the employed empirical formula has been used for a dynamic adaption of the trigger delay during the acquisition in this work. However, this simple approach cannot cope with quick changes of the heart rate from one cardiac cycle to the next (arrhythmia), because the trigger delay for the current acquisition is calculated from the preceding RR-interval. Thus, an additional rejection criterion is introduced. Data from the current cardiac cycle is rejected if its RR interval duration differs significantly ($\Delta T_{RR} = T_{RR}(n) - T_{RR}(n-1) > 100ms$) from that of the preceding cardiac cycle (cf. Fig 2.15).
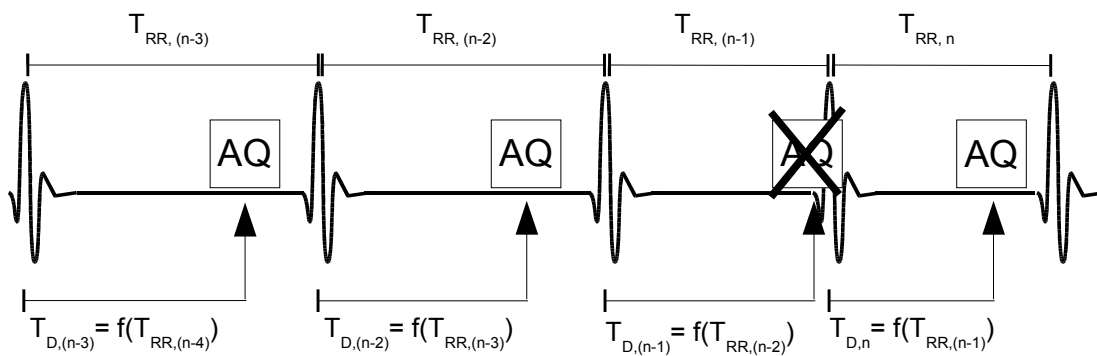

Fig 2.15 *Adaptive triggering and dynamic arrhythmia rejection. To cope with slow drifts and long-term heart rate variations (inter-RR motion), the cardiac trigger delay is constantly adapted to ensure that data is always acquired in identical cardiac phases. The underlying model defines the actual trigger delay as a function of the previous RR interval. To cope with fast fluctuations of the heart rate (arrhythmia), data are rejected if two successive RR-intervals show a marked relative difference in duration*

To prove the basic feasibility of the proposed technique, a volunteer study was conducted in three healthy adults. One conventional scan using a fixed trigger delay rejection was compared with the data obtained using the adaptive trigger delay. For both scans, a transverse 2D slice through the heart containing a section of the proximal right coronary artery (RCA) was acquired using echo-planar imaging (EPI).
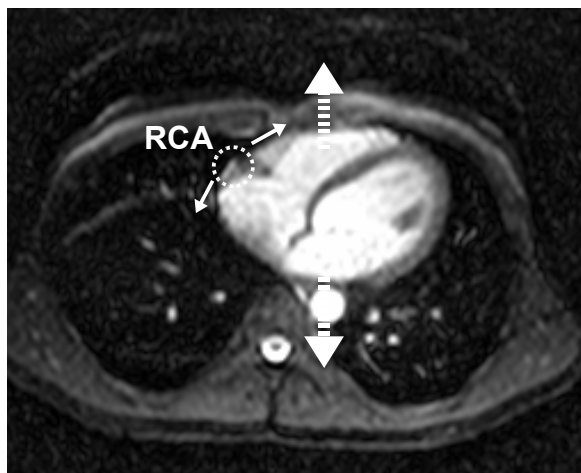

Fig. 2.16 *2D imaging slice acquired with an EPI sequence in a single shot (duration 80ms). One complete 2D slice is acquired in each RR interval, resulting in a time-series over a scan duration of approx. 2 minutes. The right coronary artery (RCA) is imbedded in the AV-groove (dotted circle). While bulk cardiac motion in AP-direction (dotted arrows) is considered to be respiration-induced, a rotational „jitter" of the RCA (solid arrows) is considered to result from inter-RR motion*

The sequence parameters were as follows: $\alpha=30°$, EPI-factor 13, single shot, TR=12.7 ms, FOV 320x260x10mm³, measured voxel size 2.50 x 2.7 x 10mm³, reconstructed voxel size 1.25 x 1.25 x 10mm³. A fat saturation prepulse was applied before each shot. The acquisition was EKG-triggered, but free-breathing.

One entire slice was acquired in each RR interval over a total scan time of 120 heart beats during free-breathing. The resulting time-series was analyzed by measuring the position of the RCA section relative to a reference (one selected frame). While an anterior-posterior (AP) shift of the entire heart was considered to be induced by respiration, a rotational trajectory ("jitter") of the RCA section in right-left (RL) direction was classified as the result of a shift in the acquired cardiac phase. The position of the RCA section, or the jitter amplitude, respectively, was measured using an freely available image processing tool [mricro].

2.6.3 Results

The result of the volunteer study is shown in Fig. 2.17. The measured displacement ("jitter") of the RCA section in RL-direction for a conventional protocol is plotted as a dotted line, while the corresponding displacement obtained using dynamic triggering is plotted as a black solid line.
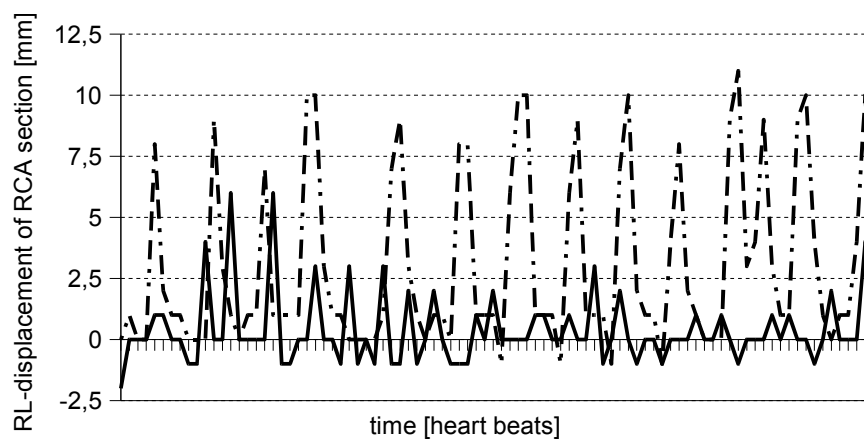
Fig 2.17 *Comparison of cardiac motion induced right-left (RL) displacement of the RCA section. Using a fixed trigger delay, a „jitter" of the RCA of approximately one centimeter (dotted line) is observed. Using an adaptive trigger delay with dynamic arrhythmia rejection (solid line), the variations can be reduced considerably*

2.6.4 Discussion and conclusion

Although experiments have only been performed in a very small number of subjects so far, a noticeable reduction of inter-RR motion resulting from variation of the cardiac cycle over the prolonged scan time was observed. The presented approach combines a dynamic adaption of the trigger delay to cope with slow heart rate fluctuations along with dynamic arrhythmia rejection to exclude image artifacts arising from data acquired during cardiac arrhythmia. Furthermore, the selection of the optimal cardiac acquisition window position was fully automated, and the ease-of-use was improved as a desired side-effect. However, a patient study in a clinical environment including a larger number of subjects is necessary to further validate the initial *in vivo* results obtained with the present approach.

3. Fast volumetric CMRA sequences with isotropic resolution using 3D radial sampling

3.1 Current state-of-the art and contribution

Current thin-slab techniques, such as e.g. the radial stack-of-stars acquisition described in the previous chapter, were well established as coronary MRA protocols in the meantime ([kim01], [stu99], [bot01]).

However, a persistent shortcoming of CMRA is the complex and time-consuming examination, requiring extensive scout scanning prior to the actual image acquisition. These preparations are necessary to locate individual anatomical details, such as the coronary arteries (Fig. 3.1 [a]), and to plan a particular measurement. As an improvement, it is desirable to acquire an extended volume covering the entire heart (Fig. 3.1 [b]), making initial planning rather simple. Provided that a high and isotropic resolution is maintained, slices and arbitrary views can be reconstructed retrospectively from the whole-heart data set without compromising image quality [bot04].
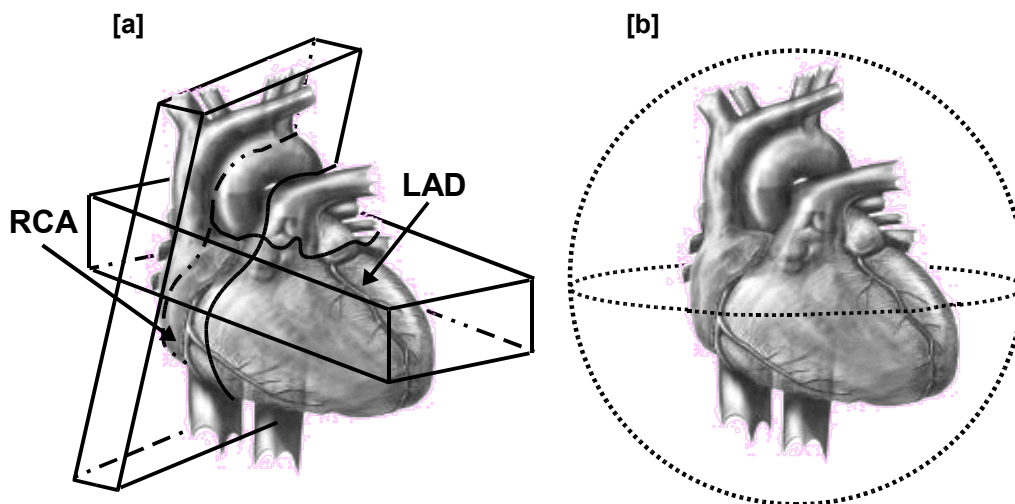
Fig 3.1 Current thin-slab protocols for coronary magnetic resonance angiography (CMRA) require precise planning of double-oblique slices [a] to capture the proximal segments of the tortuous coronary vessels (RCA/LAD). Multiple pre-scans may be necessary to locate the coronary vessels, and to plan the actual high resolution image acquisition

However, to keep the scan time within certain limits, an accelerated acquisition is mandatory. Recently, whole-heart coronary MRA protocols based on Cartesian with parallel imaging techniques [prue99] have been introduced for this purpose [web03]. However, this approach requires a precise coil sensitivity map to be measured prior to the actual image acquisition, which may, in turn, compromise the improved ease-of-use expected from the whole-heart

imaging approach. Alternatively, non-Cartesian techniques such as radial and spiral acquisitions are promising candidates. Especially three-dimensional radial acquisitions offer a great potential for scan time reduction, as they allow undersampling of the outer regions of k-space in all three spatial dimensions with very little aliasing artifacts, as it was previously found in the theory section. Unlike parallel imaging techniques, this approach does not require additional a-priory information such as a coil sensitivity map.

Consequently, a thin-slab stack-of-stars CMRA protocol as described in the previous chapter has been enhanced to a true 3D radial, whole-heart coronary MR imaging technique that provides a volumetric coverage with isotropic resolution in all three spatial dimensions in this work.

The employed 3D-radial sampling scheme has previously been described in literature for gadolinium contrast-enhanced imaging of the pulmonary vasculature during the bolus passage [bar02] in a breath-hold. However, the objective of the present work was to extend this approach to a free-breathing, whole-heart acquisition with sufficient resolution to depict the coronary arteries for optimized ease-of-use in clinical practice. For this purpose, the 3D radial acquisition was combined with an SSFP sequences [opp86] to provide high SNR, T2-like contrast and a short T_R, implemented and tested on a clinical 1.5T MR scanner. Furthermore, an image reconstruction tool based on 3D regridding of the radial MR data was developed. First phantom- and in-vivo results were obtained in healthy volunteers to demonstrate the utility of the proposed technique.

As a further extension, two particular assets of the employed 3D radial sampling pattern with respect to motion-corrected scanning were investigated. In radial or frequency-encoded scanning, the acquisition is insensitive to motion perpendicular to the readout direction. Thus, a significant reduction of motion artifacts was achieved using a „smart" order of radial readouts.

Furthermore, each radial readout provides information on the entire imaged volume. In turn, it is possible to extract motion information from each sampled echo. Thus, a self-navigated acquisition was developed that eliminates the need to acquire additional respiration tracking data by extracting motion information directly from the data acquired for imaging. Since the large coverage of the applied volumetric acquisition ensures that the region of interest is always included in the imaged slab, retrospective correction of respiratory motion is feasible with the present approach. This is a considerable benefit over previously known 2D or thin-slab approaches ([kim90], [pipe99b], [man00], [lar04], [schae99]) with image-based motion detection, which are fundamentally limited to the correction of in-plane motion.

Finally, the scan time was again reduced considerably by employing an experimental 32 element coil array on a 32 channel MR scanner. A volumetric whole-heart MR image with high and isotropic resolution was acquired in scan time less than four minutes during free breathing without the need for additional scout scans, coil sensitivity pre-scans, or respiratory navigator echoes. First *in vivo* results obtained in healthy volunteers using the proposed technique conclude the third chapter.

3.2 Fast whole-heart imaging with 3D radial sampling[4]

3.2.1 Introduction

Fast volumetric imaging with isotropic resolution, such as that provided by the previously described 3D radial acquisition technique, is desirable in a number of clinical applications of MRI. One example, namely whole-heart coronary magnetic resonance angiography (CMRA), is investigated in this section. This approach addresses a major shortcoming of coronary MRA, which is the complex and time-consuming examination, requiring extensive scout scanning prior to the actual image acquisition. These preparations are necessary to locate the coronary arteries, and to plan a particular measurement [stu99]. As an improvement, it is desirable to acquire an extended volume, e.g. the entire heart [web03], with high and isotropic resolution instead, making initial planning rather simple. Slices and arbitrary views can then be reconstructed retrospectively from the volume data set. In the present work, a 3D radial acquisition as described in the theory section was combined with a respiratory navigator-gated SSFP sequence to acquire a large volume covering the entire heart with high resolution during free breathing. Different views and slices containing e.g. the left anterior descending artery (LAD) and the right coronary artery (RCA) were reformatted retrospectively after completing the scans.

3.2.2 Methods

The 3D radial sampling scheme described in the theory section was implemented and tested on a clinical whole body 1.5T MR system (Gyroscan INTERA 1.5T, Philips Medical Systems) equipped with a five-element cardiac synergy receive coil. Prior to *in vivo* experiments, a phantom study was conducted to evaluate the available resolution and SNR for the employed 3D radial acquisition at different sampling densities. A standard resolution phantom as shown in Fig. 3.1 (diameter 220mm, thickness 50mm) filled with water doped with copper sulfate was used. The spatial resolution was measured by positioning an intensity profile across the structures. For a signal drop between two structures of more than 50%, the resolution was considered sufficient to resolve this structure. For signal-to-noise (SNR) evaluation, the SNR

---

was defined as the ratio of the mean signal intensity of a bright region within the phantom and the standard deviation of the noise signal intensity in a region outside the phantom.

The in-vivo experiments were performed on ten healthy volunteers (age range 33-47 years, all male). Written informed consent was obtained from all participants. A fat suppression prepulse was applied prior to signal sampling to suppress signal from epicardial fat. The image acquisition was EKG-triggered, with a delay of approx. 600ms, which was adapted to the subjects' heart rate. This helped to position the data acquisition window in late diastole, where motion is expected to be minimal [kim01].

To eliminate artifacts caused by respiratory motion, the measurement was navigator-gated [ehm89] using a gating window of 5mm. The respiratory navigator, based on a 2D pencil beam RF pulse, was positioned on the dome of the right hemi-diaphragm. It was applied immediately before the image acquisition to ensure precise motion information [spuen02]. To cope with residual motion within the defined respiratory gating window, prospective motion correction was employed. The underlying rigid body motion model assumes a fixed correlation factor (cf=0.6) between the SI translation of the diaphragm and the SI displacement of the heart [wan95]. For motion compensation, the excitation pulse and the acquired radial echoes were translated in frequency by according to Eq. 1.68 and 1.69, respectively.

An SSFP sequence (α=60°) was used, which was shown ([desh01], [lar02]) to provide a high signal-to-noise ratio (SNR) and high contrast between myocardium and blood . The acquisition comprised 16,384 radial readouts (25% sampling density), which were acquired over 512 cardiac cycles, with 32 readouts acquired in each cardiac cycle. An $\alpha/2$-TR/2 start-up sequence [dei94] followed by 20 dummy cycles was employed to establish the steady state. The resulting data acquisition window within the cardiac cycle was 136ms, which is rather long but feasible due to the low sensitivity to motion of the employed radial sampling scheme. The following sequence parameters were used: matrix: 256^3, FOV: $(300 \text{ mm})^3$, measured voxel size: $(1.17 \text{ mm})^3$, TE: 2.1ms, TR: 4.2ms, radial sampling ratio: 25%, receiver bandwidth 781Hz / pixel. The data from each receive coil were separately reconstructed, and the resulting image magnitudes were combined. The reconstruction time was approximately 30s per coil on a standard PC (Pentium III @ 1GHz). To visualize the RCA and LAD, the isotropic image data set was reformatted [eti02]. The total scan time was approx. 12 to 14 minutes at a respiratory gating efficiency of ~50%.

3.2.3 Results

Phantom Study - experiments using four different undersampling factors (100%, 50%, 25%, 12.5%, compared to a Cartesian acquisition) were performed. The results are shown in Fig. 3.1. The measured SNR and achieved spatial resolution at the different sampling densities are summarized in Table 3.1.
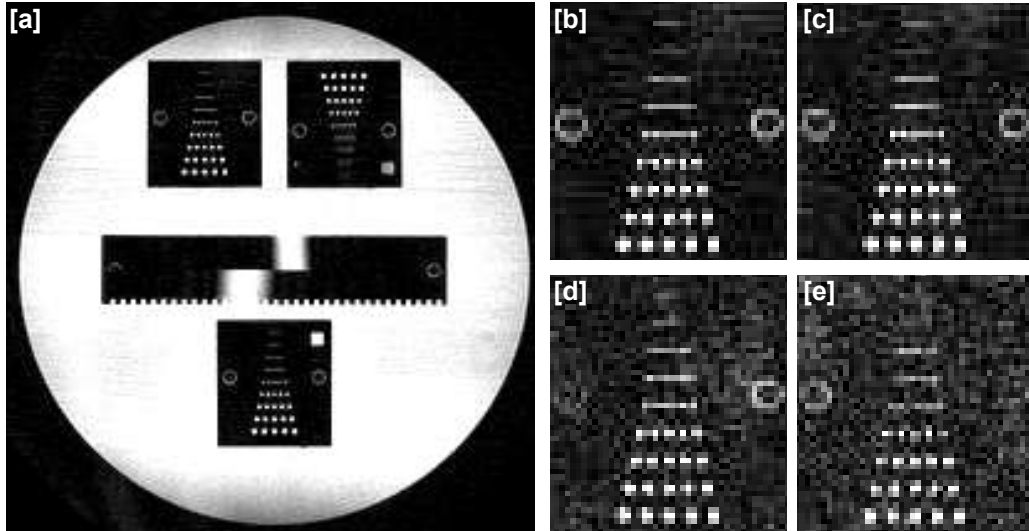
Fig. 3.1 *Reconstructed images of a resolution phantom [a]. A selected region of the phantom is shown in [b]-[e]. The phantom was imaged with different sampling densities, [b]=100%, [c] =50%, [d]=25%, [e]=12.5%*

Table 3.1: *Measured resolution and SNR using different sampling densities and weighting functions. Wa denotes the analytical, quadratic weighting function, and Wi denotes the iteratively calculated set of weights (cf. Fig. 1.14)*

Sampling density	Res. (Wa) [mm]	Res. (Wi) [mm]	SNR (Wa)	SNR (Wi)
100,0%	1.00	1.25	255	260
50,0%	1.25	1.25	221	230
25,0%	1.25	1.25	159	190
12,5%	1.25	1.5	93	135

The measured SNR achieved with the iterative weighting was higher than that obtained with the quadratic weighting, which is due to the reduced variance of the data weights as previously described in the theory section. However, the differences were larger than the theoretical values

summarized in Table 1.1, since the iterative weighting strategy underweights high spatial frequencies, which corresponds to a lowpass filtering effect, and virtually improves the measured SNR. As a consequence thereof, a slight decrease of the resolution was observed at the lowest sampling ratio when using the iterative weighting approach. However, a loss in resolution was not observed when choosing a sampling density of at least 25%. The SNR further decreased with the sampling density, which is in fair agreement with the expected results according to the SNR considerations in the theory section.

In-Vivo Results - throughout the volunteer study, a large volume comprising the entire heart and thorax was scanned. To illustrate the volume coverage, different views obtained from a single 3D data set are shown in Fig. 3.2.
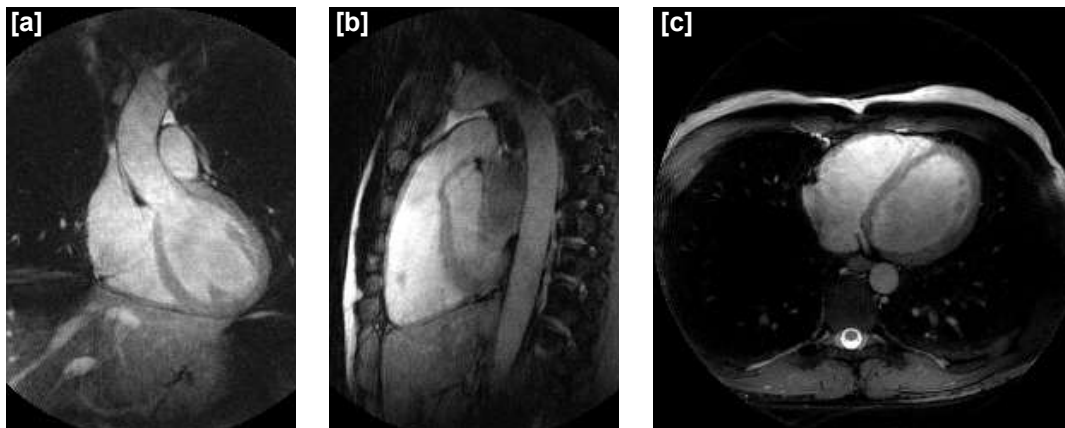
Fig. 3.2 *Reformatted coronal, sagital, and transversal views of a 3D volume data set illustrating the large volume coverage of the 3D radial, whole heart acquisition. The data were acquired using a sampling density of 25% (acceleration factor 4)*

No significant streaking artifacts are visible. Furthermore, no motion artifacts appear in the reconstructed images. In Fig. 3.3, selected results are given for the RCA and the LAD. The RCA and proximal parts of the LAD could be visualized retrospectively from the 3D data set.
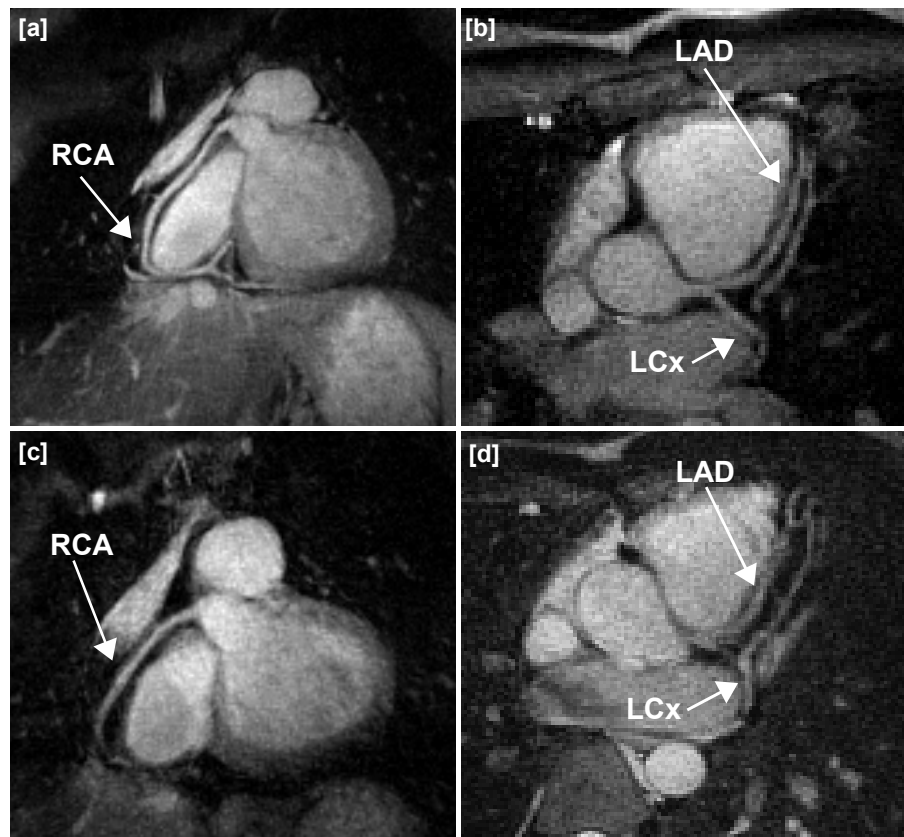
Fig. 3.3 *Reformatted views for of the coronary arteries for two volunteers, reconstructed from the volumetric data set. The corresponding sampling density was 25% (acceleration factor 4)*

3.2.4 Discussion and conclusion

With regard to the phantom study, it is noteworthy that, using the presented 3D radial acquisition, the undersampling factor may be decreased to 12.5% compared to a Cartesian acquisition. Acceptable artifact levels as well as no significant decrease in resolution were observed. This result is in good agreement with the findings from the calculation of the PSF described in the methods section. Artifacts are therefore not a predominant limitation of undersampled 3D radial acquisitions for high-contrast applications such as MRA. However, the SNR decreases with the extend of undersampling, as previously discussed in the theory section. The minimum useful sampling ratio for in-vivo measurements is therefore not limited by the undersampling artifacts, but predominantly by the available SNR. The observed decrease in SNR is in fair agreement with theory (square root of number of measured data). However, the way SNR was measured does not distinguish between random, uncorrelated noise and

systematic errors introduced e.g. by radial streaking artifacts. For this reason, some deviations between the measured and expected SNR are to be expected. For *in vivo* coronary MRA, a sampling density of 25% was chosen, which offered a good trade-off between SNR and scan time.

Compared to a conventional coronary MRA protocol [stu99], the examination was considerably simplified. One breath hold localizer scan was sufficient to plan the volumetric image acquisition. All scans were completed successfully and the major parts of the coronary arteries could be visualized retrospectively from the volumetric data set. Only the reformatting of the coronary arteries along a curved surface remained a tedious procedure that needed considerable user interaction. One possible way to improve this procedure would be a simple planar reformatting approach, for instance with a three-point-plan-scan utility.

The total scan time of a conventional protocol comprising a high-resolution localizer scan (~3 min. @60 bpm during free breathing) and two individual high resolution scans for the RCA and the LAD (~5 min. each) is approximately 13 minutes, not including the time needed for planning or repetition of misplanned scans. The total scan time of our protocol was approximately 10-14 minutes (@ 60bpm during free-breathing), which is comparable or even shorter than the scan time required for a conventional MRA protocol. Undersampling k-space in all three dimensions at a sampling density of 25% and prolonging the acquisition window resulted in a scan time decrease of a factor of six, compared to an equivalent volumetric, isotropic Cartesian acquisition. No significant artifacts were visible. This results partly from the still acceptable PSF of the 3D-radial acquisition at low sampling density as discussed on the theory section, but is also a consequence of the robustness against motion of the radial acquisition implemented in this sequence.

In conclusion, a 3D radial sampling method combined with a balanced FFE sequence and prospective respiratory motion correction was implemented on a clinical scanner and employed for coronary MRA. The volumetric scanning technique offers a considerable improvement over the current protocols, as the imaging session is greatly simplified and the risk of misplanned slices is minimized. Multiple anatomical details can be reconstructed from a single volumetric data scan without requiring additional imaging. The employed three-dimensional radial acquisition allows a high degree of undersampling, which increases the acquisition speed significantly. However, there is a trade-off between the reduced scan time and a decreased SNR.

Refinements of this techniques, for instance ways to further reduce the scan time by means of respiratory motion correction, are discussed in the following sections. In principle, these approaches do not reduce the SNR, but abbreviate scanning by a more efficient use of the data acquired throughout the respiratory cycle.

## 3.3 Respiratory motion-insensitive scanning with readout reordering[5]

3.3.1 Introduction

Respiratory motion during data acquisition is a major source of image artifacts in MRI. In cardiac or abdominal MRI, navigator gating or breath-holds are applied to reduce respiration-induced motion artifacts. However, these techniques either prolong the scan time, or patients may not tolerate them well. For faster scanning and improved patient comfort, a technique that allows free breathing during a continuous, 3D radial data acquisition is presented in this section. Motion artifacts are suppressed by using readout orientation arrangement (ROAR). The basic idea of this approach is not to reject and re-measure data that have been acquired in a period with respiratory motion, but to reorder the acquired profiles in a "smart" way that reduces the sensitivity to motion when respiration is present ([man00], [hub01]). This allows for a more efficient use of the scan time throughout the respiratory cycles, resulting in a greatly improved scan efficiency comparable to that obtained with prospective motion correction techniques [manke03]. However, a detailed knowledge of the motion pattern, such as a pre-defined affine motion model, is not necessary for the current approach. This increases the range of potential applications of respiratory motion correction to abdominal MRI, where every organ undergoes a different motion pattern, and thus a matching, global motion model is difficult to define. Initial *in vivo* results obtained in volunteers are presented that prove the basic feasibility of this technique, which was successfully applied in volumetric, abdominal MRI to image liver, spleen and kidneys simultaneously.

3.3.2 Methods

As derived in a previous section, it is a particular asset of radial sampling that the acquisition is insensitive to motion perpendicular to the readout orientation. For a 3D-radial acquisition, the polar axis can be aligned with the expected direction of motion, for instance the z-direction, as illustrated in Fig. 3.4. Thus, the readouts that lay approximately in the k_xk_y-plane are not sensitive to motion in the z-direction.

---

5   Related publication: C. Stehning, W. Dannels, K. Nehrke, K. Nehrke, O. Dössel. Free Breathing MRI Using Isotropic 3D-radial Sampling With Motion-Dependent Readout Orientation (ROAR), Proc. ESMRMB 21, (2004)
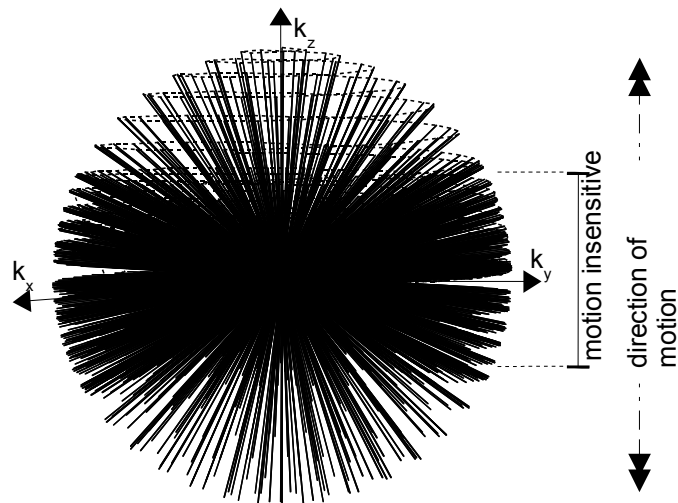
Fig. 3.4 *It is a particular asset of a radial sampling that the acquisition is insensitive to motion that occurs perpendicular to the current readout direction. Hence, if motion occurs predominantly in k_z direction, the readouts that lay approximately in the k_xk_y-plane are insensitive to motion*

This basic idea has been applied to abdominal MRI, where the precise extend of respiratory motion in the abdomen may be unknown, and it may differ between the individual organs. However, it can be assumed that respiratory motion is mostly limited to the foot-head, or superior-inferior (SI) direction, respectively [wan95]. Therefore, based on a real-time decision, motion-sensitive readouts that are oriented approximately in the SI direction were scanned during quiet end-expiration, while motion-insensitive readouts were acquired during inspiration. This is illustrated in Fig. 3.5.
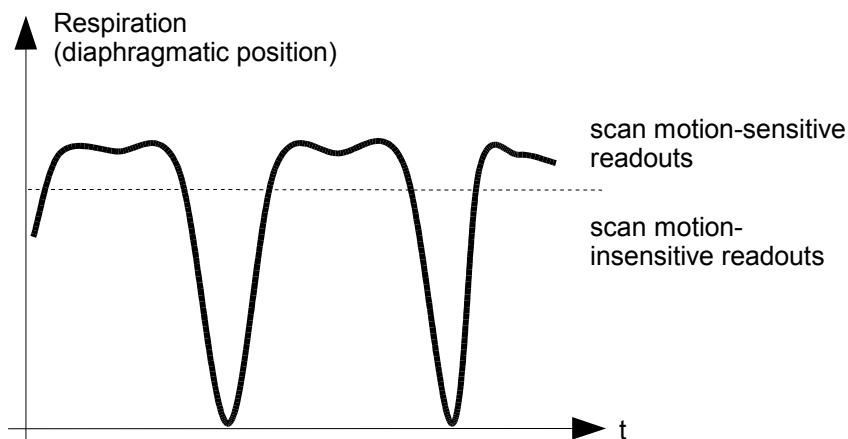
Fig. 3.5 *Basic idea of readout orientation arrangement (ROAR). Motion sensitive profiles are scanned during the quiet end-expiratory state. During inspiration, motion insensitive profiles are acquired. Thus, more efficient use of the respiratory cycle is made when compared to respiratory gating*

The respiratory state was tracked using a simple respiration bellow. The following hardware and sequence parameters were used: Philips INTERA 1.5T scanner, FOV 320mm, FFE, TR=10ms, TE=4.6ms, $\alpha=10°$, resolution 160^3, isotropic voxel size $(2\ mm)^3$, 50% undersampling, scan time ~2 min. A conventional protocol without readout reordering was acquired for comparison. The examinations were performed on ten healthy volunteers. The obtained image quality was compared.

3.3.3 Results

Selected results for abdominal MRI are illustrated in Fig. 3.6 [a] and [b], respectively.

While 3D radial sampling already provides a low motion-sensitivity, further image quality improvements were achieved using ROAR. Liver, spleen and kidneys were imaged during free breathing with little motion artifacts.
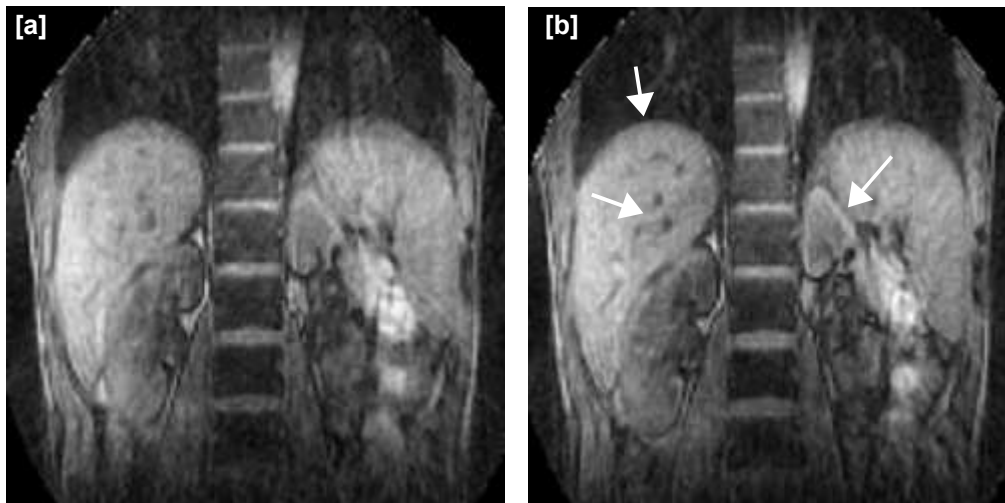
Fig. 3.6 *Exemplary slice of volumetric data set obtained during free breathing with free-running 3D radial acquisition [a]. Liver, spleen and kidneys were imaged with little motion artifacts. Using a "smart" readout orientation arrangement (ROAR, [b]), image quality was further improved especially at borders and fine structures (white arrows)*

3.3.4 Discussion and conclusion

The employed radial sampling with readout reordering allows free breathing during a continuous data acquisition, while motion artifacts are effectively suppressed. While an estimate of the motion direction is necessary to plan the acquisition, neither the exact motion amplitude nor its form (rigid body, affine, etc.) has to be known. This is an advantage over motion correction techniques such as tracking [ehm89] or affine transformations [manke03]. As a further benefit, a relatively simple external respiration sensor is sufficient, and the data acquisition is not interrupted by respiratory navigators. The latter aspect is of special interest for steady-state sequences, such as the employed fast low angle shot (FLASH) sequence [fra86], which has been combined with the 3D radial sampling scheme to image the abdomen in this study. However, certain limitations apply. Since the number of available motion insensitive profiles is limited, the proposed acquisition requires, to a certain extend, a regular breathing pattern with sufficiently long rest periods, in which the motion sensitive profiles are acquired. Furthermore, the rapid alternation of gradient orientations may entail image artifacts induced by eddy currents for some sequences, especially fully refocused gradient echo sequences such as steady state free precession (SSFP). To overcome these limitations, a more advanced acquisition that does not require external respiration sensors, or navigator pulses, and makes use of both motion-insensitive radial scanning and motion correction, is presented in the following section.

3.4 Self-Navigated image reconstruction[6]

3.4.1 Introduction

Free breathing, three dimensional (3D) cardiac MRI using pencil-beam navigators has received considerable attention, because it enables high resolution imaging and does not require patient cooperation as necessary for breath-holding. For respiratory gated data acquisition during free breathing, an end-expiratory gating window is defined prior to image acquisition, and data that have been acquired outside the predefined respiratory gating window are rejected and re-measured in the next RR interval.

However, fluctuations of the breathing pattern during prolonged scans may adversely affect the scan efficiency and prolong the scan time. Furthermore, the correlation between the navigator information and the actual position of the heart may be compromised by temporal delays [spuen02] between the navigator signal and actual image acquisition, which may arise from magnetization preparation pulses and startup cycles necessary to approach the steady state. Also, the 2D-selective navigator pulses ("pencil beams") are preferably localized at the dome of the right hemi-diaphragm to avoid contamination of the magnetization in the region of interest. While a stable correlation between the superior-inferior (SI) displacement of the diaphragm and the heart over a large number of subjects has been reported [wan95], hysteretic effects may occur [neh01], such as those induced by the difference in relative displacement between the diaphragm and the heart that reduce the precision of the motion estimation. Finally, the localization of the navigator beam requires special attention [stu99b], which may decrease the utility and reproducibility of coronary MRI.

To address these shortcomings, a self-navigated, whole-heart scanning approach using 3D radial sampling [won94] was developed and investigated in phantom- and initial *in vivo* experiments. A particular asset of the radial scanning technique includes its insensitivity to motion [glov92], which has been described in detail in the theory section. Hence, a sufficient suppression of respiratory motion artifacts can be obtained by a simple rigid-body motion correction of the individual profiles, which greatly improves the scan efficiency when compared with respiratory gating using a small, predefined gating window [ehm89]. Furthermore, the large coverage of the applied volumetric acquisition ensures that the region of interest is always included in the imaged slab, which is a prerequisite for retrospective tracking

---

6   Related publication: C. Stehning, P. Börnert, K. Nehrke, H. Eggers, M. Stuber. Free-Breathing Whole-Heart Coronary MRA with 3D-Radial SSFP and Self-Navigated Image Reconstruction, Magn Reson Med 2005 (in press)

of respiratory motion. This is a considerable benefit over 2D or thin-slab scanning approaches with retrospective motion detection ([lar04], [sha01], [kim90], [man00]), which are fundamentally limited to the correction of in-plane motion.

One possible approach to extract through-plane motion information directly from the echoes acquired for imaging is presented in phantom studies in [wie01]. However, we investigated an alternative approach in this study, with the goal of correcting for respiratory motion in free breathing, whole-heart coronary MRI. For this purpose, the 3D radial acquisition was subdivided into interleaves as shown in Fig. 3.7. The respiratory "navigators" were incorporated into the acquisition by means of extracting respiratory information from the first echo acquired for imaging in each cardiac cycle, which was acquired in foot-head direction, while the subsequent radial readout orientations required for an isotropic k-space coverage form a spiral on the surface of a sphere.

This approach offers two benefits. First, an effective respiratory motion information is provided that allows for precise motion correction for the first readouts, which are most sensitive to motion in foot-head direction. However, depending on the length of the cardiac acquisition window, the motion information might already be outdated at the end of the acquisition window, which is a known problem in free-breathing coronary MRA [spuen02]. Using the proposed acquisition order, however, the readouts acquired towards the end of the cardiac acquisition window are not sensitive to motion in the k_Z direction anyway, as it was previously shown for the readout orientation arrangement presented in the previous section. Hence, a minimal sensitivity to respiration is obtained independent of the length of the cardiac acquisition window.

Furthermore, no additional pencil-beam pulses were necessary, which reduces the planning effort and improves the ease-of-use of coronary MRI.

3.4.2 Methods

MR sequence - for this study, the previously described [won94] radial sampling pattern was subdivided into m = *1..M* interleaves, where one interleaf was acquired in each cardiac cycle. Each interleaf comprises n = *1..N* projections, and successive interleaves were derived from the first one by a polar rotation about a polar angle, φ. To allow for self-navigation, the sampling scheme was slightly modified so that the first echo acquired in each RR interval is oriented in the SI direction to obtain maximum sensitivity to respiratory motion. The 1D-FT transform of

this echo will be referred to as the "SI projection" (SI = superior – inferior). The resulting trajectories for the first, second, and M^{th} interleaf are illustrated in Fig. 3.7 [a-c], respectively.
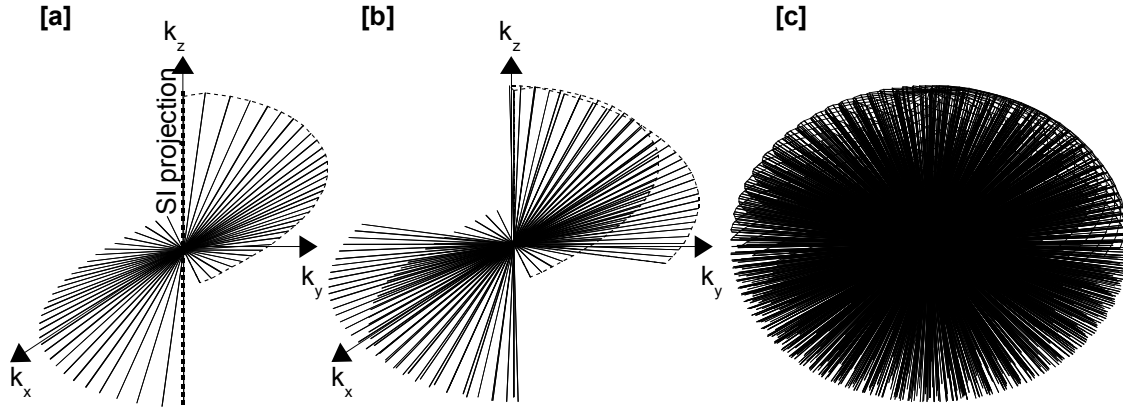
Fig. 3.7 *For the self-navigated, 3D radial acquisition, the sampling pattern is subdivided into interleaves, an example of which is shown in [a]. The dashed line is the first echo of each interleaf, which is oriented in the superior-inferior (SI) direction. Motion information is extracted from 1D Fourier transform of this echo, which is referred to as the SI projection. The orientations of the successive radial readouts follow a spiral path on the surface of a sphere from the pole to the equator (dotted line). The next interleaf is obtained from the previous one by a polar rotation about the k_z-axis [b]. By adding more interleaves with every RR interval, k-space is finally densely sampled [c] to reconstruct a motion-corrected image*

The corresponding normalized readout gradient strengths, G_x, G_y, and G_z, are given in equations 3.1 and 3.2. Compared to the sampling scheme described in Eq. 1.44, the equations were modified to orient the first readout of each interleaf in z-direction, and the number of successive readouts on the spiral path from the pole to the equator is reduced from N to (N-1), so Eq. 1.44 becomes

$$G_x(n) = \cos(\varphi) \cdot \sqrt{(1 - G_z{}^2(n))}$$

$$G_y(n) = \sin(\varphi) \cdot \sqrt{(1 - G_z{}^2(n))}$$

[3.1]

$$G_z(n) = \begin{cases} -1 & \text{for n=1} \\ \dfrac{n-1.5}{N-1} & \text{for n=2..N} \end{cases}$$

and

$$\varphi = \sqrt{\frac{2\pi(N-1)}{M}} \sin^{-1}\left(G_Z(n)\right) + \frac{2\pi \cdot i}{M} \qquad [3.2]$$

However, the isotropy of the sampling distribution, measured by the standard deviation σ of the distance between adjacent sampling points, is sufficient ($\sigma < 10\%$) only for ($N \gg M$). If the number of interleaves M is increased, and the number of radial readouts per interleaf N is decreased to obtain a sufficiently short cardiac acquisition window, this precondition is not fulfilled. Hence, a careful weighting of the data is necessary to account for the non-isotropic sampling density in k-space, which was achieved by means of the iterative, data-driven weighting approach described in the theory section.

The sequence was implemented on a clinical 1.5 Tesla MR system (Philips Medical Systems, Best, NL) equipped with a 5-element cardiac phased array coil. Although self-guided scanning techniques were successfully employed to replace EKG-triggering [lar04], we used a conventional EKG patient monitoring system for cardiac triggering for the time being. A steady state free precession (SSFP) [opp86] sequence was used to sample with a high signal-to-noise ratio (SNR) and to increase the contrast between myocardium and blood. The use of this bright-blood sequence further ensured that the cardiac blood volume contributes a major part of the MR signal, which makes respiration-induced bulk cardiac shifts easy to detect by means of a center-of-mass approach described in a following section. Furthermore, a regional saturation (REST) slab was applied prior to sampling to suppress signal from the static anterior chest wall. Fat-saturation and T2-preparation pulses were applied for improved image contrast. An $\alpha/2$-$T_R/2$ start-up sequence with 20 dummy cycles was used to approach the steady state, and $N = 32$ echoes followed by an -$\alpha/2$-$T_R/2$ tip-up pulse were acquired within each RR interval, resulting in $i_{MAX} = 512$ interleaves. The following sequence parameters were used: matrix: 256^3; 16,384 radial readouts (25% sampling density); FOV: (300 mm)^3; measured voxel size: (1.17 mm)^3; TE: 1.8ms; TR: 3.6ms; flip angle $\alpha=60°$; and receiver bandwidth, 781Hz / pixel. The data from each receive coil were separately reconstructed using a 3D re-gridding routine as described in the theory section, and the resulting images were combined with a sum-of-squares approach. The reconstruction time was approximately 30s per coil on a standard PC (Pentium III @ 1GHz). To visualize the right coronary artery (RCA), the isotropic image data set was reformatted using a software tool [eti02].

Motion detection and correction - in 3D radial sampling, every readout passes through the k-space origin, and information about the entire excited volume is included in the measured data. In detail, a 1D projection of the entire volume can be obtained by a 1D Fourier transform of the acquired echo. As described in the theory section, motion that occurs perpendicular to the readout orientation cannot be seen in these projections. However, rigid body motion that occurs in parallel to the readout orientation can be extracted from these profiles, or directly from k-space data using the Fourier shift theorem.

In the present implementation, respiration-induced bulk cardiac motion was extracted directly from the SI projection. The displacement or shift, Δs [unit pixels], relative to a reference position, s_{REF}, was calculated using a first momentum ("center of mass") approach given in Eq. 3.3, which provides sub-pixel precision. Unlike cross-correlation approaches used to measure displacement for conventional pencil-beam navigators, the center of mass approach does not require a well-defined air/tissue interface, which is not present in the SI projection obtained through the entire imaging volume.

$$\Delta s = c \cdot \frac{\sum_{i=1}^{I} m(i) \cdot i}{\sum_{i=1}^{I} m(i)} - s_{REF} \qquad [3.3]$$

In Eq. 3.3, i represents the index of a sampling point along the projection in SI direction, m(i) is the corresponding magnitude of that sample, I is the total number of samples along one readout, and c is a patient-specific linear factor.

For motion-corrected image reconstruction, the successive echoes of one interleaf measured in each cardiac cycle were modulated with a linear phase in k-space, according to the Fourier shift theorem (cf. Eq. 1.70). For the correction of *in vivo* data, a linear correlation factor of $f = 0.16$ [wan95] between the measured shift of the center of mass in SI-direction, Δs, and the translations in anterior-posterior direction, Δp (cf. Eq. 1.70), was assumed, while motion in left-right direction was neglected.

Phantom and in vivo study - to evaluate the precision of self-navigated image reconstruction compared with a reference, i.e., an image reconstructed with a conventional pencil-beam navigator for prospective respiratory motion correction, a phantom study was conducted. A

cylindrical head phantom filled with standard copper sulfate solution was positioned on a sinusoidally moving table [hub00] with a peak velocity of 18.6 mm/s in z-direction. An image obtained without motion correction was visually compared with motion-corrected images obtained with the respective motion correction techniques. Furthermore, the positions measured using the pencil-beam navigator versus the position measured with the "SI projection" were compared in a scatter plot.

To evaluate the performance of respiratory motion detection *in vivo*, the measured center-of-mass position was compared with the respiration-induced SI displacement measured with the pencil-beam navigator as a reference. This measurement was performed with and without EKG-triggering, respectively, to evaluate the impact of cardiac triggering on the precision of the image-based respiratory motion detection.

For the *in vivo* study, three healthy adult volunteers were scanned in a clinical environment at the Kennedy Krieger Institute, Baltimore, Maryland, USA, and two volunteers were scanned at the Philips Research Laboratories in Hamburg, Germany, using an identical scan protocol. Written informed consent was obtained from all participants, and the protocol was approved by the Institutional Review Board.

3.4.3 Results

The results of the phantom study are shown in Fig. 3.8 [a-c], respectively. While conventional navigator tracking (Fig. 3.8 [b]) already eliminates a large portion of motion-induced artifacts and blurring, a further increase in image quality was obtained using the self-navigated image reconstruction (Fig. 3.8 [c]).
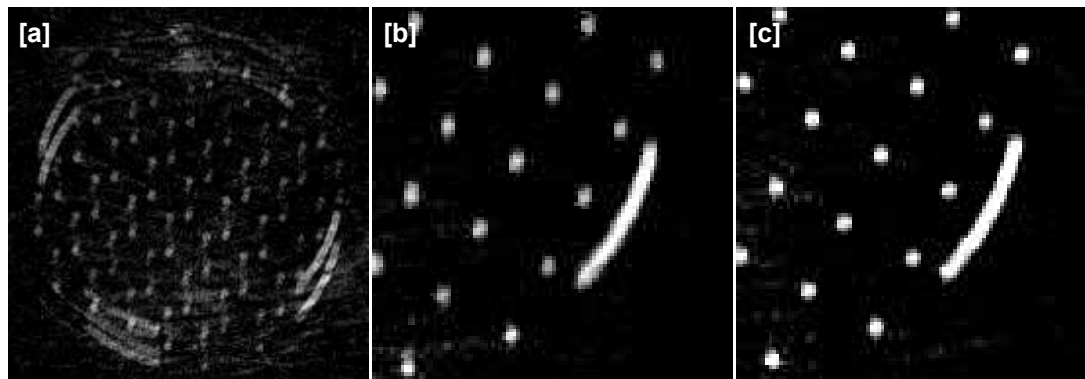
Fig. 3.8 *A sinusoidally moving phantom is imaged without motion correction [a], with navigator tracking [b], and with self-navigated image reconstruction [c]. While motion artifacts are reduced to a large extend using conventional navigator tracking, a further improved image quality is observed using self-navigation [c]*

The phantom position measured using the pencil-beam navigator versus the position measured with the "SI projection" is shown as a scatter plot in Fig. 3.9.
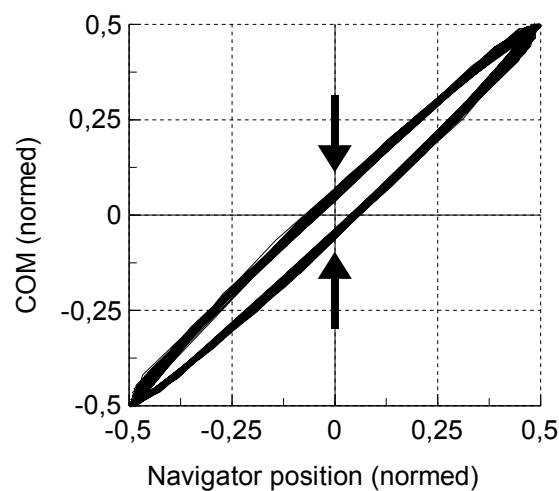
Fig. 3.9 *Lissajous plot of the normalized positions of the sinusoidally moving phantom measured with the pencil-beam navigator (abcissa) against the position determined with the SI-projections (ordinate). Deviations between both measurements depend on the velocity of the phantom. The maximum deviation occurs at the center of the stroke, where the velocity of the sinusoidally moving phantom is maximal (black arrows)*

A linear relationship between both measurements is evident, but hysteresis is observed. The resulting deviation between both lines (black arrows) was 2.63 mm.

A set of SI projections acquired *in vivo* through the thorax with and without EKG triggering is shown in Fig. 3.10 [a] and [b], respectively. The measured COM position is drawn as a solid line, while the diaphragmatic position measured with a conventional pencil-beam navigator is drawn as a dotted line into the same plot.
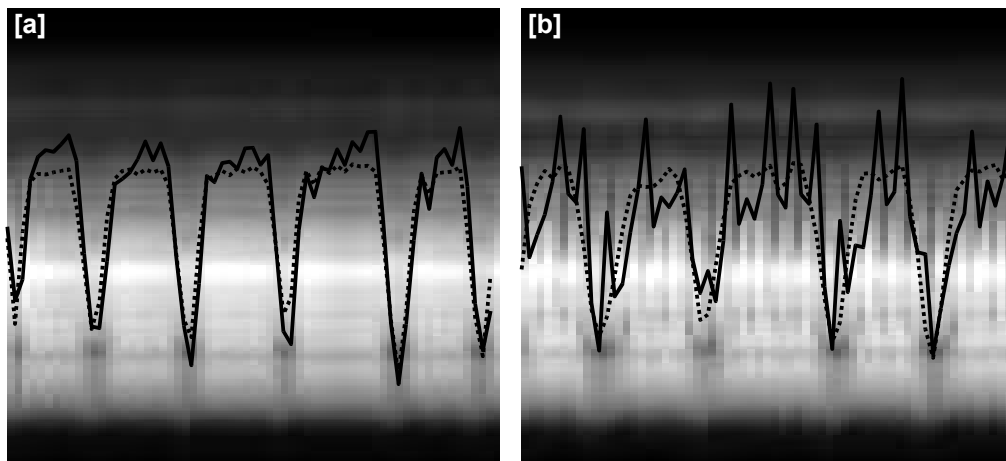
Fig. 3.10 Two exemplary sets of SI projections through the thorax acquired in vivo are shown in [a] and [b], respectively. In [a], EKG-triggering was employed, while the projections were acquired without cardiac synchronization in [b]. The measured center of mass (COM) position is plotted as a solid line, while the diaphragmatic position measured with a conventional pencil-beam navigator positioned on the dome of the right hemi-diaphragm is plotted as a dotted line for comparison. Without cardiac synchronisation [b], deviations between the two measurements as well as a marked variance of the measured COM position is observed

While a good agreement between the two measurements was observed with EKG triggering, a marked variance of the COM position was observed without cardiac synchronization.

Selected reconstructed images acquired *in vivo* are presented in Fig. 3.20. A motion-corrected image using the pencil-beam navigator for respiratory tracking is shown in [a], while an image obtained with self-navigation is displayed in [b].

On both images, a long segment of the proximal RCA is visualized. Some residual motion artifacts, as evidenced by minor blurring and streaking, are present in both images. However, the vessels appear with good delineation and contrast with both motion correction techniques. The total scan time was approx. 8 minutes during free breathing at a sampling density of 25% (acceleration factor 4).
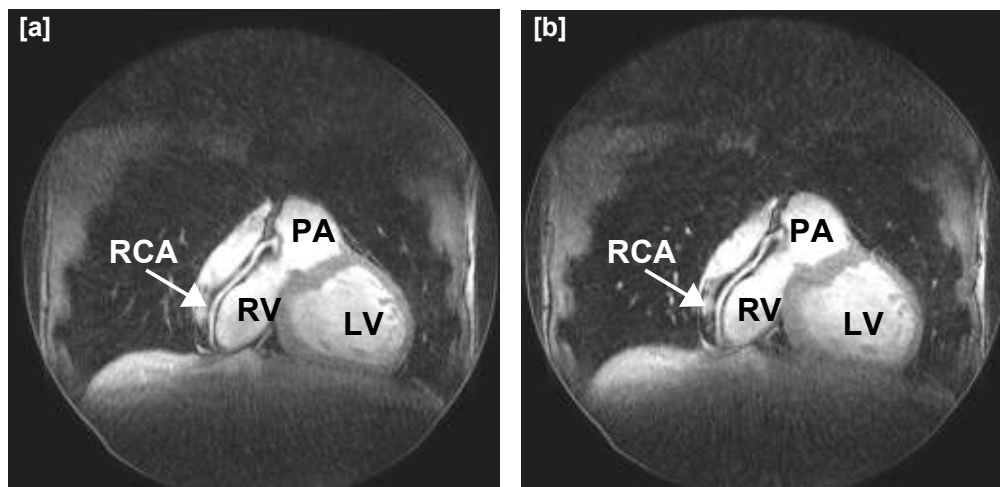
Fig. 3.11 *A reformatted view of the RCA from a volumetric acquisition obtained with navigator tracking [a] and with self-navigated image reconstruction [b]. LV = left ventricle, RV = right ventricle, PA = pulmonary artery, RCA = right coronary artery. Similar image quality was obtained with both method. The sampling density was 25% in both acquisitions*

3.4.4 Discussion and conclusion

The results of the phantom study show that the self-navigated acquisition can provide even improved image quality when compared to conventional navigator tracking, which is a result of the shortened temporal delay between "SI projection" and image acquisition. The pencil-beam navigator is commonly measured before the startup cycles, which are necessary to approach the steady state in SSFP imaging [dei94]. Thus, the motion information may already be outdated at the beginning of the data acquisition window. In contrast, with self-navigation, the SI projection is measured immediately at the beginning of data sampling. As a consequence, less blurring was observed, which is in good agreement with previous reports [spuen02]. The measured hysteresis (Fig. 3.9, black arrows) of 2.63mm is in good agreement with the expected results for a phantom moving at a peak velocity of 18.6 mm/s and a temporal delay of 72 ms, caused by 20 dummy cycles at a TR of 3.6ms (2 x 3.6ms x 18.6 mm/s = 2.68 mm).

The *in vivo* study has shown that a signal synchronous with respiration can be extracted directly from the acquired readouts in foot-head direction (SI-projections, cf. Fig. 3.10), where a good correlation with conventional navigator data was found. Nevertheless, EKG triggering is required to exclude an impact of intrinsic cardiac motion on the measurement. However, this is a limitation of motion detection using conventional navigators as well, if the navigator is placed on the heart and not on the right hemi-diaphragm. Furthermore, to date, cardiac triggering is a prerequisite for coronary imaging anyway.

While improved image quality was obtained in moving phantom experiments using self-navigation when compared to navigator gating, a similar image quality was observed *in vivo*. This preliminary result forms a contrast to the conclusion drawn in [spuen02], where a significant impact of the delay between navigators and image acquisition was observed *in vivo*. However, this discrepancy may be attributed to the employed radial scanning technique, which is very insensitive to motion to start with.

Residual motion artifacts primarily originate from static structures (e.g. anterior chest wall) in the imaged volume. However, this is a limitation of conventional navigator tracking as well. To overcome this shortcoming, the implementation of image-based respiratory gating could potentially yield a reduction of these motion artifacts at the expense of an increased scan time.

In principle, additional projections in different orientations (e.g. anterior-posterior, AP) could be acquired during the image acquisition for a multi-directional motion determination [sachs00]. Furthermore, the self-navigated reconstruction described in this chapter is not limited to the correction of rigid-body motion. Instead, the motion correction could be extended to a fully affine model [neh01].

In conclusion, a fast, free breathing, whole-heart 3D coronary MRI technique with isotropic spatial resolution and intrinsic suppression of respiratory motion artifacts was implemented on a clinical scanner. No pencil beam navigator had to be positioned prior to imaging, and motion correction was performed as a post-processing step without user interaction, which improves the ease of use in coronary MRA considerably. In principle, immediate imaging without prior scout scanning is feasible using the self-navigated acquisition in concert with the volumetric imaging technique that does not require slice planning.

3.5 Whole-heart coronary MRA in less than 5 minutes on a 32 channel MR system[7]

3.5.1 Introduction

A volumetric whole-heart imaging CMRA sequence with self-guided correction of respiratory motion has been presented in the previous chapter. However, despite scan time reductions by means of an increased scan efficiency throughout the respiratory cycle, scan times were still in the order of 8 minutes, which could be prohibitive in clinical practice, especially for patients under stress. Hence, it is the objective of the present section to propose an accelerated whole-heart sequence with identical resolution and coverage, but with a scan time significantly less than five minutes. For this purpose, an experimental 32 element coil array was employed for parallel data acquisition on a 32 channel MR equipment. Using an optimized parallel image reconstruction approach to maximize SNR and minimize the undersampling artifact level, reduction factors up to 16, or a sampling density of 6.25%, respectively, (compared to a fully sampled Cartesian acquisition) were feasible. Thus, the net scan time was reduced to the order of 2 minutes.

3.5.2 Methods

In vivo experiments were performed in four healthy adult volunteers on a 32 channel 1.5T clinical MR scanner (Achieva, Philips Medical Systems, Best, NL). A whole-body 32 channel array coil prototype as shown in Fig. 3.12 was used for parallel signal reception.

---

7   Related publication: C. Stehning, M. Stuber, P. Börnert, K. Nehrke, O. Dössel. Fast Whole-Heart Coronary MRA Using 3D-Radial SSFP With 32 Channel Parallel Acquisition and Self-Navigated Image Reconstruction, 13th Scientific Meeting ISMRM, Miami (oral presentation)

Fig. 3.12 *Experimental 32 element coil array*

To optimize SNR and minimize aliasing artifacts, the magnitude images reconstructed from each individual coil were weighted with estimated coil sensitivity maps [roem90]. These measures ensure that each coil contributes a localized region with optimal SNR to the final image, and does not contaminate other parts of the image with streaking artifacts resulting from polar undersampling. After the combination of all pre-weighted images, the resulting image I_{res} is de-weighted with the sum of all sensitivity maps for a homogeneous presentation following Eq. 3.4 [roem90].

$$I_{res} = \sum_i M_i \cdot \frac{\sum_i M_i \cdot I_i}{\sum_i M_i^2} \qquad [3.4]$$

In Eq. 3.4, M_i denotes the coil sensitivity map for the i-th coil, I_i represents the image acquired with that particular coil, and $M_i \cdot I_i$ is a pixel-by-pixel multiplication. While alternative approaches [gris00] use coil sensitivity profile estimates based on a Gaussian fit centered at the position of the particular coil, the sensitivity maps were obtained from lowpass-filtered image data in the present work, so no additional reference scan was necessary.

To cope with respiratory motion, the self-navigated image acquisition as described in the previous chapter was employed. In one subject, additional prospective respiratory gating was employed for optimized image quality [spue02]. For this purpose, the projection data acquired with the previously described "SI-projections" were processed in realtime on the MR scanner

for an accept / reject decision, while residual motion within the acceptance window was corrected using a rigid body translation model as described in the previous section.

To cope with intrinsic cardiac motion, the acquisition was EKG-triggered with a cardiac acquisition window of T_{AQ} = 115ms. The following sequence parameters were used: matrix: 256^3; FOV: $(300\ mm)^3$; measured voxel size: $(1.17\ mm)^3$; TE/TR: 1.8/3.6ms; SSFP with flip angle 60°; receiver bandwidth 781Hz / pixel. 4,096 radial readouts out of $0.5 \times p \cdot 256^2 = 102{,}944$ necessary to fulfill the Nyquist limit were acquired, resulting in an acceleration factor of 25, or 16 compared to a fully sampled Cartesian acquisition. The total scan time was approx. 2 minutes during free breathing using self-navigated respiratory tracking as described in the previous section, and approx. 4 minutes with additional respiratory tracking. The image qualities obtained with both techniques were compared qualitatively.

3.5.3 Results

An exemplary image reconstructed from angularly undersampled data acquired with a single coil is shown in Fig. 3.13 [a]. While selected regions of the image show a good SNR, or signal-to-artifact level, respectively, radial streaks still emerge into regions that are not covered by the particular coil. However, using image-based coil sensitivity estimates (cf. Fig. 3.13 [b]), streaking artifacts outreaching to remote regions could be reduced considerably. Thus, a final image with suppressed streaking artifacts can be obtained with a combination of pre-weighted data from all coils according to Eq. 3.4. An exemplary resulting image (transversal slice) is shown in Fig 3.13 [c].
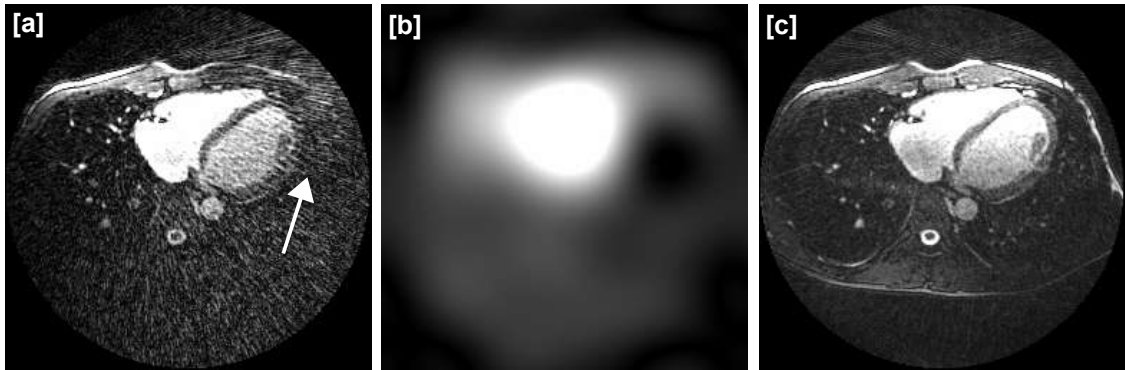
Fig. 3.13 *A single coil image reconstructed from angularly undersampled data is shown in [a]. Selected regions that are close to the respective coil element, such as the right ventricle, are acquired with good SNR and low artifact level, while radial streaks resulting from polar undersampling outreach to remote image regions (white arrow). Using a coil sensitivity estimate derived from lowpass-filtered image data [b], a contamination with streaking artifacts can be eliminated, and a final artifact-suppressed image can be obtained with a combination of pre-weighted data from all coils [c]*

A reformat depicting the right coronary artery (RCA) for one volunteer is shown in Fig. 3.14. In 3.14 [a], a rigid body correction of respiratory motion as described in the previous chapter was used (100% scan efficiency). In [b] and [c], additional respiratory gating (50% gating efficiency) was used at the expense of an increased scan time. The resulting scan times were 2 minutes [a] and 4 minutes ([b], [c]) at a heart rate of 60bpm.

Fig. 3.14 *Reformat depicting the right and left coronary artery for one volunteer using retrospective tracking [a], and additional prospective respiratory gating ([b], [c]). Better image quality, a sharper delineation of the vessel and less blurring was observed using respiratory gating, and more distal parts of the coronary vessels could be reformatted from the volumetric data set*

3.5.4 Discussion and conclusion

The applied 3D-radial sampling in combination with the parallel acquisition was shown to provide a good image quality and low aliasing artifacts despite a very low sampling density (6.25 %). Using a clinical 32-channel system, the whole-heart data set with high and isotropic resolution was acquired in as little as 2 minutes during free breathing. While long segments of the coronary arteries (RCA) were clearly depicted with both respiratory motion correction strategies, a sharper delineation of the vessel- and ventricle borders was observed using additional prospective respiratory gating, when compared to a rigid-body motion correction of all acquired data. This is in good agreement with previous results in the literature [spue02]. Furthermore, less blurring was observed, and more distal parts of the RCA could be reformatted from the data set using additional respiratory gating. Despite the reduced gating efficiency of 50%, scan times were still significantly lower than 5 minutes, making the present respiratory gated approach well-suited for clinical practice.

In conclusion, the ease-of-use of coronary MRA was maximized using the fast, self-navigated, whole-heart imaging approach, which could be performed in a few minutes without the need for an extensive planning procedure. Furthermore, the acquisition can be performed during free breathing for optimal patient comfort, without the need for additional respiratory bellows or navigator pulses. A suppression of aliasing artifacts and optimization of the available SNR was achieved using a parallel image reconstruction approach with coil sensitivity maps estimated directly from image data. No additional reference scan to estimate precise RF field maps as in alternative approaches ([sod97], [prue99]) was necessary. In principle, any scout scanning

prior to imaging becomes superfluous using the proposed technique. Hence, the total duration of the MR examination can be reduced considerably for optimal patient comfort, and, last but not the least, an increased throughput of coronary MRA in clinical practice. Further experiments are desirable to validate the feasibility of the technique in a clinical environment.

Conclusion

Two major shortcomings of today's coronary magnetic resonance angiography have been addressed in this work. First, the long scan times resulting from the low scan efficiency have been improved considerably. To achieve this goal, radial scanning was employed, which was shown to have low sensitivity to motion and allows the application of extended cardiac acquisition windows. Furthermore, a self-guided motion correction technique that requires very little user interaction was developed to cope with intra-RR motion. Relative motion between data subsets is measured exclusively for the coronary vessels, and retrospective motion correction is performed prior to reconstructing a final, high-resolution image. No additional pre-scans were necessary to measure the coronary vessel motion, as the motion model by means of the parameters of an affine transformation were extracted directly from the data acquired for imaging. Moreover, the underlying MR sequence provides a water-only, fat-suppressed depiction of the coronary vessels without the need for conventional fat suppression prepulses as a desired side-effect. In conclusion, a novel CMRA approach with intra-RR cardiac motion correction was developed, implemented and evaluated on a clinical MR scanner. First *in vivo* images prove the feasibility of the present technique.

To improve the ease of use and the clinical throughput in coronary MR imaging, the second, major part of this work was focused on a novel whole-heart CMRA protocol, which allows for an accelerated acquisition of a volumetric data set covering the entire thorax with sufficient resolution to depict the coronary arteries. For this purpose, a CMRA sequence using steady state free precession (SSFP) and 3D radial trajectories has been developed and implemented on a clinical scanner, and appropriate software to reconstruct images from 3D radial MR data by means of 3D-regridding has been programmed. Using the proposed technique, extensive slice planning becomes superfluous, and a whole-heart data set can be acquired without prior scout scanning in a scan time competitive to current thin-slab protocols.

However, there is a trade-off between the increased acquisition speed and a decrease in SNR. These losses in SNR are an inherent property of the radial acquisition and have to be offset in practice by other advantages of radial sampling to justify its use. Moreover, it requires a high signal level to start with, which calls for the use of multiple surface coils for signal reception and of adequate sequences. However, the available SNR level for the envisaged application, namely a volumetric whole-heart acquisition, can be considered sufficient to offset the above

mentioned SNR losses, as a large volume is acquired, yielding a high signal level to start with. Furthermore, the future transition to higher field strengths and the application of multichannel coil arrays will help to provide improved SNR.

Further benefits of the volumetric acquisition with radial scanning were investigated in the third chapter. One particular asset, namely that the acquisition is insensitive to motion perpendicular to the readout direction, has been utilized to reduce the sensitivity to respiratory motion by rearranging the readouts in a "smart" order. Moreover, motion information has been extracted directly from the data acquired for imaging, which allows for a correction of respiratory motion without the need for additional navigator echoes. First in-vivo results prove the feasibility of this "self-navigated" imaging approach, resulting in a further improved ease-of-use, since no navigator beams need to be planned prior to image acquisition. Extending the image-based motion detection to cope with intrinsic cardiac motion to replace EKG triggering could be an interesting future refinement.

In conclusion, a volumetric CMRA protocol with improved ease-of-use and intrinsic correction of respiratory motion has been presented in this work. Furthermore, novel strategies to cope with cardiac motion based on the acquisition of multiple heart phases in every RR interval have been developed. A combination of both approaches, namely volumetric whole-heart scanning including multiple cardiac phases, could not be performed to date due to hardware limitations, especially the available computer memory. For future studies, this could be a very interesting goal, as a high resolution, time-resolved whole heart („4D") data set may potentially provide substantial functional information on the cardiac vasculature, and therefore greatly improve the diagnostic value of cardiac MR images.

While the basic feasibility of the presented techniques has been verified *in vivo* in healthy adult volunteers, further evaluation of the proposed techniques in patients in a clinical environment is desirable to gather extended experience in a greater number of subjects. However, selected approaches that were presented in this work have already been transferred to external sites, such as the National Heart, Blood and Lung Institute (NHLBI) in Washington DC, USA, as well as the Johns Hopkins University School of Medicine in Baltimore, MD, USA, for further evaluation. We are looking forward to the outcome of these future studies.

References

[abr83] : Abragam A, The principles of nuclear magnetism, Oxford University Press, 1983

[amh05]: Statistical fact sheet. www.americanheart.org -> publications & ressources

[bai20]: Bainbridge FA. The relation between respiration and the pulse rate. J. Physiol 1920; 54: 192-202

[bar02]: Barger AV, Block WF, Toropov Y, Grist TM, Mistretta CA. Time-resolved contrast-enhanced imaging with isotropic resolution and broad coverage using an undersampled 3D projection trajectory. Magn Reson Med 2002; 48: 297-305

[bloch46]: Bloch F, Hansen WW, Packard M. Nuclear induction. Phys Rev 1946; 69: 127

[bot01]: Botnar RM, Stuber M, Danias PG, Kissinger KV, Boernert P, Manning WJ. Coronary magnetic resonance angiography. Cardiol Rev 2001; 9: 77-87

[bot04]: Botnar RM, Leiner T, Kissinger KV, van Yperen G, Manning WJ. Improved motion compensation in coronary MRA. Proc. ISMRM 2004 2004; 12: 2555

[bot99]: Botnar RM, Stuber M, Danias PG, Kissinger KV, Manning WJ. A fast 3D approach for coronary MRA. Magn Reson Imag 1999; 10: 821-5

[bron97] : Bronstein, Semendjajew, Musiol, Mh   lig, Taschenbuch der Mathematik, Harri Deutsch, 1997

[bue04]: Buehrer M, Huber ME, Kozerke S, Boesiger P. Prediction of heart rate variation during coronary MRA, using a neuronal network. Proc. ISMRM 2004; 11:

[cra88]: Crawley AP, Wood ML, Henkelmann RM. Elimination of transverse coherences in FLASH MRI. Magn Reson Med 1988; 8:

[dan97]: Danias PG, McConnell MV, Khasgiwala VC, Chuang ML, Edelman RR, Manning WJ. Prospective navigator correction of image position for coronary MR angiography. Radiology 1997; 203: 733-6

[dei94]: Deimling M, Heid O. Magnetization prepared true FISP imaging. Proc SMRM 1994; 2: 495

[desh01]: Deshpande VS, Shea SM, Laub G, Simonetti OP, Finn JP, Li D.. 3D magnetization-prepared true-FISP: a new technique for imaging coronary arteries. Magn Reson Med 2001; 46: 494-502

[dix84]: Dixon WT. Simple proton spectroscopic imaging. Radiology 1984; 156: 189-94

[ehm89]: Ehmann RL, Felmlee JP. Adaptive technique for high-definition MR imaging of moving structures. Radiology 1989; 173: 255-63

[eint1906]: Einthoven W, Ueber die Deutung des Elektrocardiogrammas, Archiv fuer die ges. Physiologie, Bonn, 1906

[eint1907]: Einthoven W, Ueber die Form des menschlichen Electrokardiogramms, Archiv fuer die ges. Physiologie, Bonn, 1907

[eti02]: Etienne A, Botnar RM, van Muiswinkel AM, Bösiger P, Manning WJ, Stuber M. "Soap-bubble" visualization and quantitative analysis of 3D coronary magnetic resonance angiograms. Magn Reson Med 2002; 48: 658-66

[eti02]: Etienne A, Botnar RM, van Muiswinkel AM, B"siger P, Manning WJ, Stuber M. "Soap-bubble" visualization and quantitative analysis of 3D coronary magnetic resonance angiograms. Magn Reson Med 2002; 48: 658-66

[fisch99]: Fischer SE, Wickline SA, Lorenz CH. Novel real-time R-wave detection algorithm based on the vectorcardiogram for accurate gated magnetic resonance acquisitions. Magn Reson Med 1999; 42: 361-70

[foo00]: Foo TKF, Ho VB, Hood MN. . Radiology 2000; 214: 283-89

[fox03]: Foxall DL. Starter sequence for steady state free precession imaging. Proc. ISMRM 2003 2003; 959: 210

[fra86]: Frahm J, Haase A, Matthaei D. Rapid three-dimensional MR imaging using the FLASH technique. J Comput Assit Tomogr 1986; 10: 363-8

[gio02]: Giorgi B, Dymarkowski S, Maes F, Kouwenhoven M, Bogaert J.. Improved visualization of coronary arteries using a new three-dimensional submillimeter MR coronary angiography sequence with balanced gradients. Am J Roentgenol 2002; 179: 901-10

[glov92]: Glover GH, Pauly JM. Projection reconstruction for reduction of motion effects in MRI. Magn Reson Med 1992; 28: 275-89

[grad80] : Gradshteyn IS; Ryzhik IM, Table of integrals, series and products, Academic Press, 1980

[gris00] : Griswold MA, Jakob PM, Nittka M, Goldfarb JW, Haase A, Partially parallel imaging with localized sensitivities (PILS), , 2000

[gris02]: Griswold MA, Jakob PM, Heidemann RM, Nittka M, Jellus V, Wang J, Kiefer B, Haase A. Generalized autocalibrating partially parallel acquisitions (GRAPPA). Magn Reson Med 2002; 47: 1202-10

[haa86]: Haacke EM, Patrick JL. Reducing motion artifacts in two-dimensional Fouriertransform imaging. Magn Reson Imag 1986; 4: 359-76

[haa99] : Hacke ME, Brown RW, Thompson MR, Venkatesan R, Magnetic resonance imaging: physical principles and sequence design, Wiley, 1999

[haacke99] : Hacke ME, Brown RW, Thompson MR, Venkatesan R, Magnetic resonance imaging: physical principles and sequence design, Wiley, 1999

[har01]: Hargreaves BA, Vasanawala SS, Pauly JM, Nishimura DG. Characterization and reduction of the transient response in steady-state MR imaging. Magn Reson Med 2001; 46: 149-58

[har03]: Hargreaves BA, Vasanawala SS, Nayak KS, Hu BS, Nishimura DG. Fat-suppressed steady-state free precession imaging using phase detection. Magn Reson Med 2003; 50: 210-3

[hartk02]: Hartkens T, Rueckert D, Schnabel J, Hawkes D, Hill D, Bildverarbeitung fuer die Medizin: Algorithmen, Systeme, Anwendungen. Proceedings des Workshops vom 9. - 11. M„rz 2003 in Erlangen, Springer, 2002

[hay71]: Haywood LJ, Saltzberg SA, Murthy VK, Huss R, Harvey GA, Kalaba R. Clinical use of R-R interval prediction for ECG monitoring: time series analysis by autoregressive models. J Assoc Adv Med Instrum 1971; 6: 111-6

[hoge97]: Hoge RD, Kwan RKS, Pike B. Density compensation functions for spiral MRI. Magn Reson Med 1997; 38: 117-28

[hub00]: Huber ME, Stuber M, Botnar RM, Bösiger P, Manning WJ. Low-cost MR-compatible moving heart phantom. J Cardiovasc Magn Reson 2000; 2: 181-7

[hub01]: Huber ME, Hengesbach D, Botnar RM, Kissinger KV, Bösiger P, Manning WJ, Stuber M. Motion artifact reduction and vessel enhancement for free-breathing navigator-gated coronary MRA using 3D k-space reordering. Magn Reson Med 2001; 45: 645-52

[jack91]: Jackson J, Meyer CH, Nishimura DG, Macovski A. Selection of a convolution function for Fourier inversion using gridding. IEEE Trans Med Imag 1991; 10: 473-8

[kim01]: Kim WY, Stuber M, Kissinger KV, Andersen NT, Manning WJ, Botnar RM. Impact of bulk cardiac motion on right coronary MR angiography and vessel wall imaging. J Magn Reson Imag 2001; 14: 383-90

[kim90]: Kim WS, Mun CW, Kim DJ, Cho ZH. Extraction of cardiac and respiratory motion cycles by use of projection data and its applications to NMR imaging. Magn Reson Med 1990; 13: 25-37

[kram98]: Kramer C. Integrated approach to ischemic heart disease: The one-stop-shop. Cardiol Clin 1998; 16: 267-76

[kum75]: Kumar A, Welti D, Ernst R. NRM Fourier zeugmatography. Magn Reson Med 1975; 18: 69-75

[lar02]: Larson AC, Simonetti OP, Li D. Coronary MRA with 3D undersampled projection reconstruction TrueFISP. Magn Reson Med 2002; 48: 594-601

[lar04]: Larson AC, White RD, Laub G, McVeigh ER, Li D, Simonetti OP. Self-gated cardiac cine MRI. Magn Reson Med 2004; 51: 93-102

[lark04]: Larkman DJ, Atkinson D, Hajnal JV. Artifact reduction using parallel imaging methods. Topics in Magnetic Resonance Imaging 2004; 15: 267-75

[lau93]: Lauzon ML and Butt BK. Generalized k-space analysis and correction of motioneffects in MR imaging. Magn Reson Imag 1993; 30: 438–46

[lau96]: Lauzon ML, Rutt BK. Effects of polar sampling in k-space. Magn Reson Med 1996; 36: 940-9

[laut73]: Lauterbur PC. Image formation by induced local interactions: examples employing nuclear magnetic resonance. Nature 1973; 242: 190

[liang99] : Liang ZP, Lauterbur PC, Principles of magnetic resonance imaging: a signal processing perspective, Wiley, 1999

[man00]: Manduca A, McGee KP, Welch EB, Felmlee JP, Grimm RC, Ehmann RL. Autocorrection in MR imaging: adaptive motion correction without navigator echoes. Radiology 2000; 215: 904-9

[manke01]: Manke D, Boernert P, Nehrke K, Nagel E, Doessel O. Accelerated coronary MRA by simultaneous acquisition of multiple 3D stacks. Magn Reson Imag 2001; 14: 478-83

[manke03]: Manke D, Nehrke K, Börnert P. Novel prospective respiratory motion correction approach for free-breathing coronary MR angiography using a patient-adapted affine model. Magn Reson Med 2003; 50: 122-31

[manke03]: Manke D, Nehrke K, B"rnert P. Novel prospective respiratory motion correction approach for free-breathing coronary MR angiography using a patient-adapted affine model. Magn Reson Med 2003; 50: 122-31

[mans73]: Mansfield P, Grannell PK. NMR 'diffraction' in solids ?. J Phys C: Solid State Phys 1973; 6: 422-27

[mey92]: Meyer CU, Hu BS, Nishimura DG, Macovski A. Fast spiral coronary artery imaging. Magn Reson Med 1992; 28: 202-13

[mricro]: MRIcro medical image viewer. http://people.cas.sc.edu/rorden/mricro.html

[neh01]: Nehrke K, Börnert P, Manke D, Bock JC. Free-breathing cardiac MR imaging: study of implications of respiratory motion -- intial results. Radiology 2001; 220: 810-5

[ngu03]: Nguyen TD, Nuval A, Mulukutla S, Wang Y. Direct monitoring of coronary artery motion with cardiac fat navigator echoes. Magn Reson Med 2003; 50: 235-41

[opp86]: Oppelt A, Graumann R, Barfuss H, Fischer H, Hartl W, Schajor W. FISP: eine neue schnelle Pulssequenz fuer die Kernspintomographie. Electromedica 1986; 54: 15-18

[pauly]: Reconstruction of non-Cartesian data. http://mrel.usc.edu/class/articles

[pet00]: Peters DC, Korosec FR, Grist TM, Block WF, Holden JE, Vigen KK, Mistretta CA. Undersampled projection reconstruction applied to MR angiography. Magn Reson Med 2000; 43: 91-101

[pipe00]: Pipe JG. Reconstructing MR images from undersampled data: data-weighting considerations. Magn Reson Med 2000; 43: 867-75

[pipe95]: Pipe JG, Duerk JL. Analytical resolution and noise characteristics of linearly reconstructed magnetic resonance data with arbitrary k-space sampling. Magn Reson Med 1995; 34: 170-8

[pipe99]: Pipe JG, Menon P. Sampling density compensation in MRI: rationale and an iterative numerical solution. Magn Reson Med 1999; 41: 179-86

[pipe99b]: Pipe JG. PROPELLER MRI: Application to head motion and free-breathing cardiac imaging. Magn Reson Med 1999; 42: 963-69

[prue99]: Pruessmann KP, Weiger M, Scheidegger MB, Boesiger P.. SENSE: sensitivity encoding for fast MRI. Magn Reson Med 1999; 42: 952-62

[prue99]: Pruessmann KP, Weiger M, Scheidegger MB, Boesiger P.. SENSE: sensitivity encoding for fast MRI. Magn Reson Med 1999; 42: 952-62

[ra94]: Rasche V, Holz D, Schepper W. Radial turbo spin echo imaging. Magn Reson Med 1994; 32: 629-38

[ra99]: Rasche V, Proksa R, Sinkus R, Börnert P, Eggers H. Resampling of data between arbitrary grids using convolution interpolation. IEEE Trans Med Imag 1999; 18: 385-92

[rib04]: Ribe LR, Hansen MS, Ringgaard S, Pedersen EM. Motion analysis for shortening scan times by use of affine transformations and HARP in cardiac MRI. Proc. ISMRM 2004 2004; 12: 653

[roe]: Deutsches Roentgen-Museum. http://www.roentgen-museum.de

[roem90]: Roemer PB, Edelstein WA, Hayes CE, Souza SP, Mueller OM. The NMR phased array. Magn Reson Med 1990; 16: 192-225

[ros84]: Rosen BR, Wedeen VJ, Brady TJ. Selective saturation in NMR imaging. J Comput Assist Tomogr 1984; 8: 813-18

[sachs00]: Sachs TS, Meyer CH, Pauly JM, Hu BS, Nishimura DG, Macovski A. The real-time interactive 3-D DVA for robust coronary MRA. IEEE Trans Med Imag 2000; 19: 73-9

[schae99]: Schaeffter T, Rasche V, Carlsen IC. Motion compensated projection reconstruction. Magn Reson Med 1999; 41: 954-63

[sche01]: Scheffler K, Heid O, Hennig J.. Magnetization preparation during the steady state: fat-saturated 3D TrueFISP. Magn Reson Med 2001; 45: 1075-80

[sche03]: Scheffler K, Hennig J. Eddy current optimized phas encoding schemes to reduce artifacts in balanced SSFP imaging. Proc. ISMRM 2003; 11: 294

[schom95]: Schomberg H, Timmer J. The gridding method for image reconstruction by Fourier transformation. IEEE Trans Med Imag 1995; 14: 596-607

[sha01]: Lauzon ML and Butt BK. Two-step navigatorless correction algorithm for radial k-space acquisitions. Magn Reson Med 2001; 45: 277-88

[slich96] : Slichter CP, Principles of Magnetic Resonance, Springer, 1996

[sod97]: Sodickson DK, Manning WJ. Simultaneous acquisition of spatial harmonics (SMASH): fast imaging with radiofrequency coil arrays.. Magn Reson Med 1997; 38: 591-603

[soy]: An early example. http://www.soyeeproductsny.com -> an early example

[spue02]: Spuentrup E, Stuber M, Botnar RM, Kissinger KV, Manning WJ. Real-time motion correction in navigator-gated free-breathing double-oblique submillimeter 3D right coronary artery magnetic resonance angiography. Invest Radiol 2002; 37: 632-6

[spue04]: Spuentrup E, Katoh M, Buecker A, Manning WJ, Schaeffter T, Nguyen TH, Kuhl HP, Stuber M, Botnar RM, Gunther RW. Free-breathing 3D SSFP CMRA with radial k-space sampling - comparison with cartesian k-space sampling and cartesian gradient-echo CMRA. Radiology 2004; 231: 581-6

[spuen02]: Spuentrup E, Manning WJ, Botnar RM, Kissinger KV, Stuber M. Impact of navigator timing on free-breathing submillimeter 3D coronary magnetic resonance angiography. Magn Reson Med 2002; 47: 196-201

[stu99]: Stuber M, Botnar RM, Danias PG, Sodickson DK, Kissinger KV, van Cauteren M, de Becker J, Manning WJ. Double-oblique free-breathing high resolution three-dimensional coronary magnetic resonance angiography. J Am Coll Cardiol 1999; 34: 524-31

[stu99b]: Stuber M, Botnar RM, Danias PG, Kissinger KV, Manning WJ. Submillimeter three-dimensional coronary MR angiography with real-time navigator correction: comparison of navigator locations. Radiology 1999; 212: 579-87

[stud99]: Studholme C, Hill D, Hawkes D. An overlap invariant entropy measure of 3D medical image alignment. Pattern Recognition 1999; 32: 71-86

[sul85]: O'Sullivan JD. A fast sinc gridding algorithm for Fourier inversion in computer tomography. IEEE Trans Med Imag 1985; 4: 200-7

[twieg83]: Twieg DB. The k-trajectory formulation of the NMR imaging process with applications in analysis and synthesis of imaging methods. Med Phys 1983; 10: 610-21

[vla02] : Vlaardingerbroek MT, den Boer JA, Magnetic resonance imaging, Springer, 2002

[wan95]: Wang Y, Riederer SJ, Ehmann RL. Respiratory motion of the heart: kinematics and the implications for the spatial resolution in coronary imaging. Magn Reson Med 1995; 33: 713-9

[web03]: Weber OM, Martin AJ, Higgins CB. Whole-heart steady-state free precession coronary artery magnetic resonance angiography. Magn Reson Med 2003; 50: 1223-8

[who]: . WHO: Milestones in knowledge of heart and vascular disorders. ; :

[wie01]: Wieben O, Barger AV, Block WF, Mistretta CA. Correcting for translational motion in 3D projection reconstruction. Proc. ISMRM 2001; 9: 737

[won94]: Wong ST, Roos MR. A strategy for sampling on a sphere applied to 3D selective RF pulse design. Magn Reson Imag 1994; 32: 778-84

[wood85]: Wood ML, Henkelmann RM. MR image artifacts from periodic motion. Med Phys 1986; 12: 143-51

[xia93]: Xiang QS, Henkelmann RM. k-space description for MR imaging of dynamicobjects. Magn Reson Med 1993; 29: 422-28

A. Appendix

I. Publications

1. **C. Stehning**, P. Börnert, K. Nehrke, H. Eggers, O. Dössel. Fast Isotropic Volumetric Coronary MR Angiography Using Free Breathing 3D Radial Balanced FFE Acquisition, Magn Reson Med 2004, 52:197-203

2. **C. Stehning**, P. Börnert, K. Nehrke, O. Dössel. Free breathing 3D balanced FFE coronary MRA with prolonged cardiac acquisition windows and intra-RR motion correction, Magn Reson Med 2005, 53:719-23

3. **C. Stehning**, P. Börnert, K. Nehrke, H. Eggers, M. Stuber. Free-Breathing Whole-Heart Coronary MRA with 3D-Radial SSFP and Self-Navigated Image Reconstruction, Magn Reson Med 2005 (in press)

4. J. Rahmer, P. Börnert, **C. Stehning**. 3D Radial Ultrashort Echo-Time Imaging, prepared for submission in Magn Reson Med.

II. Presentations

1. **C. Stehning,** P. Börnert, K. Nehrke, H. Eggers, O. Dössel. Fast Isotropic Volume Imaging for Coronary MRA using 3D-PR, 11th scientific meeting ISMRM, Toronto, 2003 (oral presentation)

2. **C. Stehning,** P. Börnert, T. Schäffter, O. Dössel. Radial Balanced FFE Imaging with Extended Sampling Windows for Fast Coronary MRA, 11th scientific meeting ISMRM, Toronto, 2003 (oral presentation)

3. **C. Stehning,** P. Börnert, K. Nehrke, O. Dössel. Continuous Epicardial Fat Suppression for Coronary MRA Using Balanced FFE With Long Cardiac Acquisition Windows – A Comparison of Two Techniques, 12th scientific meeting ISMRM, Kyoto, 2004 (oral presentation)

4. **C. Stehning,** P. Börnert, K. Nehrke, O. Dössel. ECG-Triggered, Free Breathing Coronary MRA Using Radial Balanced FFE With Intra-RR Motion Correction, 12th Scientific Meeting ISMRM, Kyoto, 2004 (oral presentation)

5. **C. Stehning,** W. Dannels, P. Börnert, K. Nehrke, O. Dössel. Free Breathing MRI Using Isotropic 3D-radial Sampling With Motion-Dependent Readout Orientation (ROAR), 21st Meeting of the ESMRMB, Copenhagen, 2004 (oral presentation)

6. **C. Stehning**, K. Nehrke, P. Börnert, H. Eggers, M. Stuber. Free Breathing Whole-Heart MRI With 3D Radial SSFP and Self-Navigated Image Reconstruction, 8th Scientific Meeting SCMR, San Francisco (oral presentation)

7. A.O. Ustun, K.Z. Abd-Elmoniem, **C. Stehning**, M. Stuber. Automated Identification of Minimal Myocardial Motion Period During a Cardiac Cycle for Coronary MRI, 8th Scientific Meeting SCMR, San Francisco (poster presentation)

8. R. Nezafat, **C. Stehning**, A. M. Gharib, M. Y. Desai, R. G. Weiss, R. I. Pettigrew, E. R. McVeigh, M. Stuber. Improved Spatial-Temporal Resolution MR Coronary Blood Flow Imaging at 3T, 8th Scientific Meeting SCMR, San Francisco (poster presentation)

9. J. Rahmer, P. Börnert, C. Schröder, **C. Stehning.** 3D Radial FID-Sampling for Ultrashort TE Imaging at 3T, 12th Scientific Meeting ISMRM, Kyoto, 2004 (oral presentation)

10. **C. Stehning**, R. Nezafat, A. M. Gharib, M. Y. Desai, R. G. Weiss, R. I. Pettigrew, E. R. McVeigh, M. Stuber. Dual Navigators for Time-Resolved MR Coronary Blood Flow Imaging at 3T During Free Breathing, 13th Scientific Meeting ISMRM, Miami (poster presentation)

11. **C. Stehning**, M. Stuber, P. Börnert, K. Nehrke, O. Dössel. Fast Whole-Heart Coronary MRA Using 3D-Radial SSFP With 32 Channel Parallel Acquisition and Self-Navigated Image Reconstruction, 13th Scientific Meeting ISMRM, Miami (oral presentation)

12. K. Nehrke, P. Börnert, **C. Stehning**, R. Winkelmann, I. Grässlin, J. Overweg, P. Mazurkewitz, T. Rozijn. Free Breathing Whole Heart Coronary Angiography on a Clinical Scanner in less than 4 Minutes, 13th Scientific Meeting ISMRM, Miami (oral presentation)

III. Invited Presentation

- **C. Stehning,** P. Börnert, K. Nehrke, H. Eggers, O. Dössel. Improved Fast Isotropic Volume Imaging for Coronary MRA using 3D-PR, 15th MR Angio Club Meeting, Dublin, 2003

IV. Honors and Awards

• ***Philips CMR Science Award***, presented on January 21, 2005 for the time-resolved measurement of the blood flow in the coronary arteries during free breathing on a clinical 3T scanner, performed in collaboration with Reza Nezafat at the National Institutes of Health, Bethesda, USA.

• ***ISMRM Educational Student Stipends*** for the 11th ISMRM, Toronto, Canada (2003), 12th ISMRM, 2004, Kyoto, Japan (2004) and 13th ISMRM, Miami, USA (2005).

• ***German Academic Exchange (DAAD) postgraduate stipend*** to support the research project conducted at the Johns Hopkins University School of Medicine, Baltimore, in summer 2004

V. Acknowledgements

My thanks go to many colleagues and friends who supported me during this thesis. First, I would like to express my gratitude to Dr. Peter Börnert, whose patience, commitment and superb supervision provided the basis for this thesis, and who assisted me throughout my work at the Philips Research Laboratories. Second, I would like to thank Prof. Dr. Olaf Dössel from the Institute of Biomedical Engineering at the University of Karlsruhe, whose supervision and cooperation made this dissertation possible. Finally, I would like to thank the co-referee, René Botnar from the Technical University of Munich, for his time and assistance with the present work.

From the Philips group, a hearty thank goes to Dr. Kay Nehrke, a walking library, for having an immediate, sound answer to virtually any problem, and to Dr. Dye Jensen, head of the tomographic imaging group, for the opportunity to work in an excellent scientific environment. Holger Eggers helped me getting a jump start into MR image reconstruction, and always took time to explain MR basics to me no matter how often I showed up in his office with a bunch of questions.

A hearty thanks also goes to Prof. Dr. Stuber from the Johns Hopkins University School of Medicine, Baltimore, MD, USA, for the excellent cooperation and the opportunity to work in his team, to think out of the box, and for providing a constant stream of MR ideas. Also, to all my colleagues and labmates at Johns Hopkins, Wesley, Ali, Ahmed, Ibrahim, Khaled, Li, Allen, Saurav, Ulrike, Michael, Feilim, Alan, Milind, Ronald, and Nael. Among these wonderful people I had the pleasure to work with, special thanks go to Reza Nezafat at the NIH in Bethesda, USA, for the great and fun cooperation and his hospitality, and for fully convincing me that Washington DC is a great place.

Further I am greatly indepted to my former and present office mates in Hamburg, Robert and Richard, and all my colleagues I had the pleasure to work with during the past three years: Peter Koken, Peter Mazurkewitz, Jürgen Rahmer, Peter Forthmann, Detlef, Tobias, Stefanie, Dirk, Claas, Hannes, Christoph, Babak, Steffen, Bernd, Jochen, Jürgen W, Bernhard Gleich and Bernhard Metzger, and Daniel Herzka.

Finally, I would like to thank Petra and my family for their patience and for keeping me grounded, hoping that I will have the opportunity to return all the support that I received during the last years.

VI. Curriculum Vitae

I was born on December 23, 1975, in Dorsten, Germany, as son of Karin and Werner Stehning. I attended primary school at the St. Agatha Grundschule and secondary school at the St. Ursula Gymnasium in Dorsten, from which I graduate with the Abitur in June 1995. From fall 1995 to 1996, I rendered the alternative civilian service in the Maria Lindenhof old people's home in Dorsten.

From October 1996 to January 2002, I studied electrical engineering at the University of Bremen. The branch of my studies was communications engineering. My study research project entiteled „Design and Setup of an all-optical Fiber Multiplexer" and my Diploma thesis entiteled „DSP-based Measuring System for Temperature Compensated Fiber Optical Oxygen Sensing" were completed at the Max-Planck-Institute for Marine Microbiology (MPI) in Bremen. The Diploma thesis was supervised by Dr. Gerhard A. Holst (MPI) and Prof. Dr. Walter Anheier, University of Bremen.

Since May 2002 I am working at the Philips Research Laboratories in Hamburg, as a Ph.D. student and member of the research group of Prof. Dr. Olaf Dössel, Institute of Biomedical Engineering, Karlsruhe, Germany. The focus of my studies was the development of motion correction strategies and volumetric acquisition methods for coronary magnetic resonance angiography, including MR sequence programming and image reconstruction. From June 1 to August 28, 2004, I had the opportunity to work in the group of Prof. Dr. Matthias Stuber at the Johns Hopkins University School of Medicine in Baltimore, MD, USA. In September 2004, I continued my research in Hamburg. This thesis was supervised by Prof. Dr. Olaf Dössel and Dr. Peter Börnert, Philips Research Laboratories, Hamburg.